Laboratory Studies of Segregation in Prograding Deltas of TRSU Tailings

A THESIS SUBMITTED TO THE FACULTY OF THE
UNIVERSITY OF MINNESOTA
BY

Rochelle Grace Widmer

IN PARTIAL FULFILLMENT OF THE REQUIREMENTS
FOR THE DEGREE OF
MASTER OF SCIENCE

Kimberly Hill

December 2020

Table of Contents

List of Tables

List of Figures

Chapter 1 - Introduction and Background

1.1 Introduction and Statement of Challenges

Canada has the third largest oil reserves in the world with 97% of these reserves located in the form of oil sands (Introduction to Oil Sands, 2018). It is estimated that there are 165.4 billion barrels of bitumen in those reserves (Roshani, 2017), and they are increasingly being harvested to help meet the energy needs of the world's growing human population. These oil sands reserves lie beneath 142,000 km^2 of boreal forest and peat bogs in the Athabasca, Peace River, and Cold Lake regions of Alberta and Saskatchewan, Canada (Introduction to Oil Sands, 2018; Roshani, 2017). Bitumen, a highly viscous and dense petroleum-based hydrocarbon, is the primary component extracted from these mines that is used for energy needs. The bitumen is eventually upgraded into Synthetic Crude Oil (SCO) before it is refined and sold to consumers as products such as gasoline and diesel ("Oil Sands Extraction and Processing," 2016).

Byproducts from the bitumen extraction process include the sands, clays, and silts that originally contained the bitumen, a tremendous amount of process water, and trace solvents and additives. Significant fractions of the landscape are being replaced by storage facilities for these byproducts in what are called oil sands tailings ponds. As the reclamation of this land is a slow, arduous process, it is becoming a growing concern. The tailings ponds are now perceived as a serious environmental issue because of their growth across the landscape as the production of bitumen rapidly increases as shown in **Figure 1.1.1**. In 2017, Canada's crude oil production from mined oil sands alone reached 1.14 million barrels per day (mbd) and the rapidly expanding industry is predicted to produce 1.73 mbd by 2035 (2018 CAPP Crude Oil Forecast, Markets & Transportation, 2018).

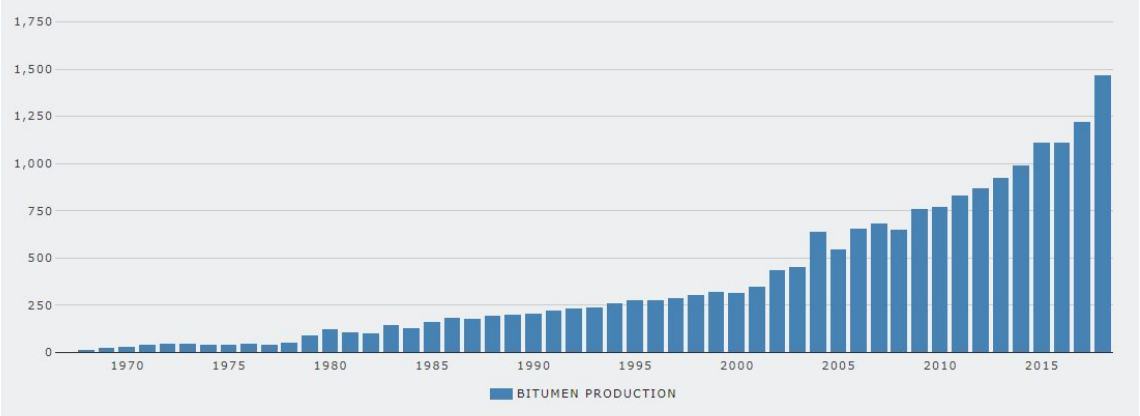

Figure 1.1.1: Canada's annual bitumen production from surface mining techniques in thousands of barrels produced in one day (bbl/day). This data is from Canadian Association of Petroleum Producers (CAPP) and Annual Energy Review (AER) and reported by Oil Sands Magazine ("Mining Operations," 2019).

Tailings remediation is an essential activity for the Canadian oil sands industry due to the increase in public concern for the environmental impact and strict government regulations regarding tailings disposal (Xu, Dabros, & Kan, 2013). This has encouraged the industry to take extra precautions while storing tailings and work toward faster tailings pond reclamation. Certain details of the reclamation process have provided the motivation for this thesis.

The reclamation of the sands and subsequent restoration of the landscape is complicated by the numerous processes currently undertaken to maximize the extraction of bitumen from the mined sands. These practices generate waste materials, often called oil sands tailings, that contain primarily: water, sand, fine silts and clays, and residual bitumen (Beier, Wilson, Dunmola, & Sego, 2013). These oil sands tailings are considered unwanted and are discharged to storage facilities in the form of large bodies of water or tailings ponds. These ponds are designed to facilitate the separation of solids from water by way of settling due to gravity. If this is completely accomplished, the water can be removed and reused in future oil sands operations (Canada's Oil Sands Fact Book, 2018) and the settled solids can be reused in the landscape to return the land back into its original state. However, this process is complicated by the fact that there are residual

bitumen and solvents as well as fine grained solids in the tailings stream; the result is that a perfect separation of solids from water is not possible.

To better understand the causes of these major issues with tailings ponds faced by the oil sands industry, it is helpful to review the major processes of oil sands production from mining the ore to the settling that occurs in tailings ponds. The next section describes this process and presents these issues.

1.2 Detailed Background of Oil Sands Tailings and Tailings Ponds

1.2.1 Step 1: Surface Mining

The majority of the mineable oil sands in the Canadian province of Alberta are found along the Athabasca River. Approximately 20% of those reserves are located less than 50 meters from the surface and are economically feasible to extract in a process called surface mining. Typically, oil sands are excavated from open-mine pits by large hydraulic shovels as exhibited in **Figure 1.2.1**. These mined materials usually contain 7% to 13% bitumen by weight ("Mining for Bitumen," 2017).

Figure 1.2.1: Surface mining operation near the Athabasca river at Fort McMurray in Alberta, Canada. Ore is removed and placed in large trucks that haul the materials to processing facilities. Photo from Oil Sands Magazine ("Mining Operations," 2019).

1.2.2 Step 2: Oil Sands Processing

After the oil sands are mined, they are delivered to a processing plant where the bitumen is separated from the unwanted solids and water. This process consists of three primary stages: ore preparation, bitumen extraction, and froth treatment.

During the ore preparation stage, large amounts of hot water are added to the oil sands to produce a pumpable slurry that is delivered to the processing plant. The second stage, bitumen extraction, includes separating most of the bitumen from the rest of the slurry: coarse sand, fines, and process water. Process water is defined as any water that has come into contact with oil sands or was released from tailings and not returned to the environment for safety reasons. The separation process is done in a way that produces an intermediate product called bitumen froth, composed of sediment, process water, and bitumen that wasn't removed. During the third stage, froth treatment, solvent is added as a diluent to the bitumen froth. This addition decreases the viscosity of the bitumen froth to enable separation of most of the bitumen in the froth from the water and solids. Typically, 90% to 92% of the bitumen can be extracted depending on the quality of the oil sands (Beier et al., 2013). **Figure 1.2.2** from the Oil Sands Tailings Magazine contains a diagram illustrating this process.

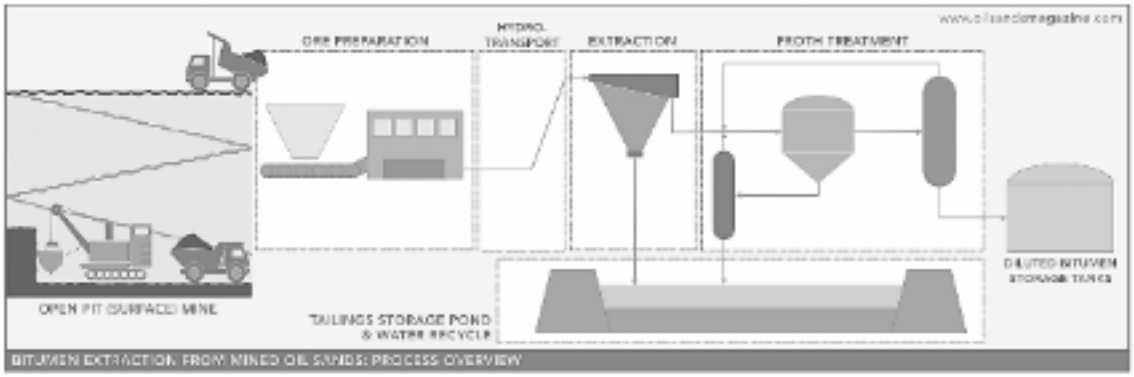

Figure 1.2.2: Diagram of oil sands processing, described in the text. Image from Oil Sands Magazine ("Mining for Bitumen," 2017).

At this point, the solvent needs to be separated from the waste product before returning to the tailings ponds due to economic and environmental reasons. The unit where this is done is called the Tailings Solvent Recovery Unit (TSRU), designed specifically to remove and separate solvent out of the tailings before the tailings are discharged to the tailings ponds. Recovered solvent is re-used farther upstream in the process. We refer to the water materials separated from the solvent as TSRU tailings. Typically, the amount of solvent contained in TSRU tailings varies between 5% and 10%.

All the bitumen removed from these processes is then stored and the rest of the materials are sent to the oil sands tailings ponds where the solids are allowed to settle out over time.

1.2.3 Step 3: Discharging the Byproducts

The materials left over from the bitumen extraction and froth treatment processes (i.e., the byproducts) are discharged from the processing plant through a series of pipes into tailings ponds (Roshani, 2017). As the production of one barrel of bitumen results in a substantially larger volume of tailings, the ponds need to be tremendously large structures that can provide the storage volume necessary for: (1) shorter-term settling processes specifically needed for water recovery and (2) longer-term holding capacity for all of the solids originally contained in the mined ore.

Figure 1.2.3 contains a satellite image of a tailings pond located in Alberta, Canada. The picture shows a somewhat early-stage image of the facility where the pipe is discharging in the lower region at a point in the image that looks something like the apex of a fan. This is a common scene in tailing ponds where, after some discharge has occurred, the ponds appear to consist of river deltas with several intermittent braided channels carrying the discharged materials. These tailings ponds are considered

temporary storage facilities with the ultimate goal that they will eventually be solidified and that the land can be reclaimed and returned to an environmentally friendly and inhabitable landscape, not dissimilar from its original state.

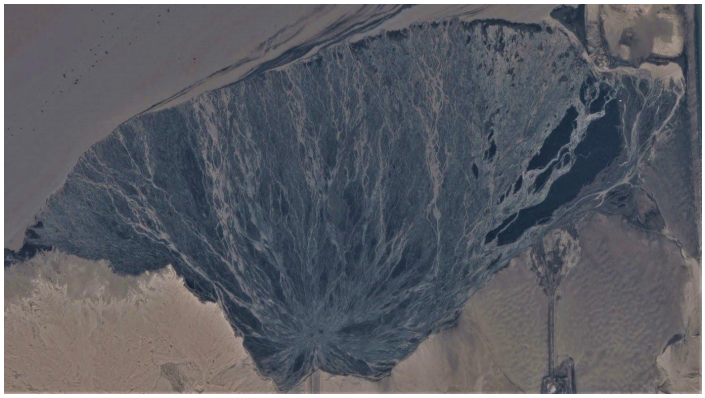

Figure 1.2.3: Satellite image taken of an oil sands tailings pond in Alberta, Canada. The pipe outlet, near the bottom of the image, releases tailings into the pond where it gradually builds up the beach. The streams covering the beach drain into the tailings pond, shown in the top portion of the image. This pond contains TSRU tailings which are a resultant from a process that strips-off and recycles any remaining solvents from tailings before they are placed in these storage ponds.

1.2.4 Step 4: Settling and Separation in Tailings Ponds

The production of one barrel of bitumen results in the production of almost 15 barrels of tailings (Hande, 2014) including the original particles present in the mined oil sands, the water, and any additives remaining after the extraction of bitumen. As mentioned above, tailings ponds are designed to enhance the separation of solid particles from process water. The materials discharged in streams to the ponds are mostly water and contain a somewhat low volumetric concentration of solids consisting of a mixture of sediment, including sand, silt, and clay particles. Upon entry to the ponds, some of the particles settle to the bottom quickly whereas some settle much more slowly, creating trouble for the idealized and envisioned reclamation process. Those in the industry often describe the different short- and long-term behaviors of the materials by distinguishing three main categories of materials: (1) fast-settling sand particles, (2) a clarified surface

water layer with some residual bitumen, and (3) an aqueous suspension of fine clay and silt particles (BCG Engineering I., 2010).

The majority of the structure that appears similar to a river delta in **Figure 1.2.3** is made of the most rapidly-settling particles. These particles form what many (e.g,. Hande, 2014) consider the "beach" on the edge of tailings ponds. The finer clay- and silt-sized particles not captured along the beach settle much more slowly in the pond. After settling for several years, they reach a solid content of 30% to 35% and at this point are referred to as Mature Fine Tailings (MFT) (BCG Engineering I., 2010; Roshani, 2017; Wang, et al. 2010). At this relatively high concentration, they are in the form of a unique high-density, non-Newtonian suspension and can remain in a fluid-like state for decades, hindering the reclamation process. Of the 15 barrels of byproducts discharged into tailing ponds for every barrel of bitumen, two barrels of this long-term, high-density Mature Fine Tailings are produced (Hande, 2014). Due to the slow consolidation rate exhibited by MFT, industry leaders are actively seeking different modes of intervention such as accelerated dewatering technologies so that reclamation can be obtained within a reasonable amount of time after mining has ceased.

1.2.5 Step 5: Reclaiming the Water

Water plays a critical role at any bitumen production facility since it is used in the transportation and processing of the materials. It takes roughly 12 to 13 barrels of water to produce one barrel of bitumen. The clarified water layer that rises to the top of tailings ponds can be reclaimed and used in the process again. The reclaimed water provides over 80% of the facility's process water needs. This reduces the amount of freshwater that needs to be drawn from freshwater sources. All tailings ponds are constructed with groundwater monitoring facilities that are designed to capture and recycle material that may seep from the ponds. The 2011 Lower Athabasca Water Quality Monitoring Program was developed to track changes in water quality, assess the cumulative effects of

oil sands activity, and inform any necessary mitigation ("7 Facts on the Oil Sands and the Environment," 2019).

1.2.6 Final Comments

The goal of the work included in this thesis is to add to the understanding of certain issues that contribute to the slow reclamation process of oil sands tailings ponds. In particular, we address the call by a consortium of oil companies called Canada's Oil Sands Innovation Alliance (COSIA) to understand the segregation processes that can occur in the discharge and settling of byproducts related to oil sand processes. The long-term goal is that this better understanding will facilitate improved reclamation capabilities.

Toward this, we first studied the behavior of surrogate mixtures subjected to analogous boundary conditions. We evaluated a safer alternative mixture in order to observe the transportation, segregation, and deposition behaviors of the mixture in various situations and related this information to TSRU tailings. Before proceeding to the description of our experimental procedures and results, we first consider a naturally occurring surrogate system with many processes similar to those separating particles in oil tailings ponds. Specifically, we consider systems of river deltas and relatively stationary bodies of water (e.g., naturally occurring lakes, ponds and oceans). Since the materials entering tailings ponds are fast-traveling aqueous mixtures that deposit in a stagnant system and move freely, we found a number of similarities between oil sands tailings deltas and natural deltas as Kim et al. (2009) did with iron mine tailings. In the next section, we consider the mechanisms present in the formation of a natural prograding delta toward gaining insight for the problems associated with tailings ponds.

1.3 Natural Prograding Deltas and Insights into Tailings Ponds

1.3.1 Introduction to Similarities Between Natural Deltas and Tailings Deltas

For a first look at the connection between landforms created at the edge of oil sands ponds during the discharge of tailings and landforms we refer to as natural river deltas created by the discharge of rivers into large bodies of water, we consider the pictures in **Figure 1.3.1**. A satellite image of an oil sands tailings pond located in Alberta, Canada is shown in **Figure 1.3.1 (a)**. An image of the Selenga River delta on Lake Baikal in Siberia, Russia is included in **Figure 1.3.1 (b)**.

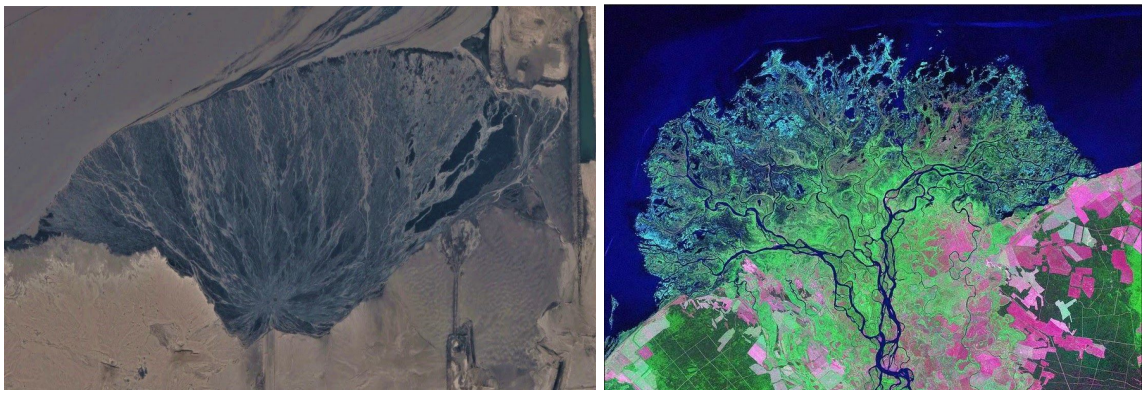

(a) **(b)**

Figure 1.3.1: **(a)** An oil sands tailings pond delta in Alberta, Canada. This is a satellite image taken on July 17, 2016. **(b)** The Selenga River delta on Lake Baikal in Siberia, Russia. The Landsat-8 image of the Selenga River delta is courtesy of the U.S. Geological Survey.

In the formation of a landform at the edge of an oil sands tailings pond, a mixture of water, sediment, and solutes enter the relatively stationary pond at a localized point. Upon entrance to the pond, some sediment settles close to the entry point and forms a landform often similar to that shown in **Figure 1.3.1 (a)**. The details can vary considerably from one such landform to the next, dependent on boundary conditions such as the material properties of the sediment, discharge rate, and fine particle content, though these dependencies have not been studied much in the oil sands environment.

The formation of a river delta occurs as a river enters a slower moving body of water, such as an ocean, lake, or other water-containing reservoir (Seybold, Andrade, & Herrmann, 2007) and a mixture of fluid and sediment enter the water at a relatively small point. Upon entrance to the reservoir, some sediment settles close to the inlet and forms a river delta, often similar to that shown in **Figure 1.3.1 (b)**. The details can vary considerably from one such delta to the next and unlike the landforms associated with tailings ponds, these have been studied in great detail, including tidal and wave effects (Abeyta, 2016), fluid discharge, and sediment concentration.

1.3.2 Introduction to Gilbert Deltas

A common style of delta often seen in lacustrine and marine environments is the Gilbert-style delta, first described in 1885 by Grove Karl Gilbert. A Gilbert delta is a deltaic system that forms where a river opens up and flows into a body of standing water that is considerably deeper than the feeding channel (Gobo, 2014). These deposits contain three different areas known as the topset, foreset, and bottomset initially characterized by Barrell (1912) as indicated in **Figure 1.3.2**. Typically, the topset is a relatively thin and flat layer of sediment, the foreset is a steeper area that progrades away from the supply stream and the bottomset is another thin and flat layer of sediment. Gilbert-style deltas most often form in lakes but they can also be seen in marine regions.

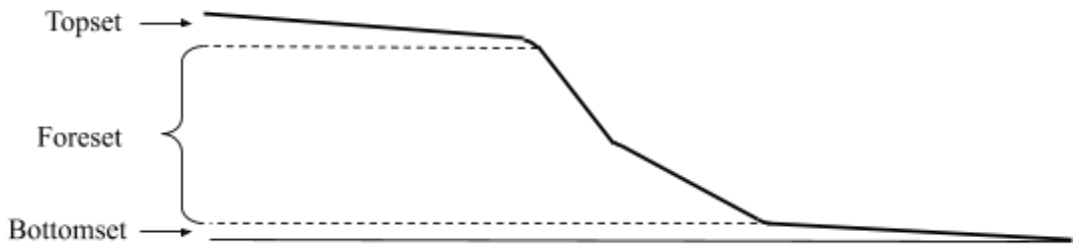

Figure 1.3.2: Topset, foreset, and bottomset of a delta or deposit front.

The transfer of sediment from the topset to the steep-sloped foreset depends on the type (e.g. particle density, size, shape) and amount of sediment delivered by the stream flow and the difference in the density between the stream and the basin water (Gobo, 2014). When the density of the stream is lower than the basin (often associated with fresh, warmer water moving into salty, colder water), the flow is categorized as "hypopycnal" and the flow takes the form of a buoyant plume with fine-grained, low-density sediment in suspension that is deposited primarily along the bottomset (Nemec, 1995; Wildermuth, Reece, & Morgan, 2015). If the densities for the stream and the basin are the same, the flow is categorized as "homopycnal" and there is rapid mixing and the deposition of sediment occurs in a higher proportion near the mouth of the stream (Colella, De Boer, & Nio, 1987). What is called "hyperpycnal flow" occurs when the density of the incoming stream has a higher density than the basin and the sediment plunges down the foreset slope and deposits along the slope (Lei, Chiu, & Wu, 2019). Both homopycnal and hyperpycnal flow typically result in the progression of the front of the delta away from the incoming mixture of particles and fluid.

1.3.3 Insights on Segregation in Deltas From Experimental Work

The formation and sorting patterns of Gilbert deltas have been studied in the laboratory setting (e.g. Kleinhans, 2005; Lai & Capart, 2007). In order to learn more about the mechanisms present in the formation of deltas, we considered work by Maarten G. Kleinhans on grain-size sorting that occurred on the lee side or foreset of a subaqueous Gilbert delta. By studying various sediment mixtures in a narrow flume with varying flow conditions, Kleinhans was able to systematically investigate particle sorting trends he observed in both natural and experimental prograding deltas. Kleinhans focused on two segregation trends. First he reported an overall vertical sorting, where, contrary to many water-driven sediment transport systems, small particles were found in higher concentrations the closer the sediment was sampled near the top of a dune. Second, he reported that independent of the normal grading of large particles upward in these deltas,

they exhibited the commonly observed “downstream fining” at the surface of the delta, where the smaller particles were in higher concentration the further downstream one sampled in the delta.

In these careful investigations, Kleinhans proposed physical explanations for the trends he observed that correlated with dynamics in his experiments. One trend that Kleinhans was able to explain was upward fining which he related to three basic steps. Firstly, large particles are deposited immediately along the upper end of the lee slope or the topset (grain fall) whereas smaller particles saltate or become suspended and are deposited farther downstream. Secondly, the sediment located at the upper part of the foreset eventually exceeds a threshold and the sediment falls down the slope (grainflow or avalanche). Lastly, the movement of sediment down the slope engages kinetic sieving where small particles meander inward into small pore spaces while the large particles move outward and continue to travel down the slope, yielding an upward fining trend, illustrated in **Figure 1.3.3**. Kleinhans also explained the trend of upward coarsening by grain fall where large particles collect at the upper end of the foreset whereas smaller particles continue to travel downstream and deposit lower on the foreset slope. This effect is well-known and has been seen in the field as well as in the laboratory setting. Kleinhans also found that the concentration, grain size and the amassing of sediment decreases in the downstream direction from the delta which would result in a downstream fining behavior. All of these mechanisms were behaviors that we would be able to identify in the laboratory.

Given that these behaviors are all associated with the mechanics of sediments in a prograding delta, we expect that we could relate them to segregation behaviors in prograding dunes of sediments more closely resembling those in oil sands ponds.

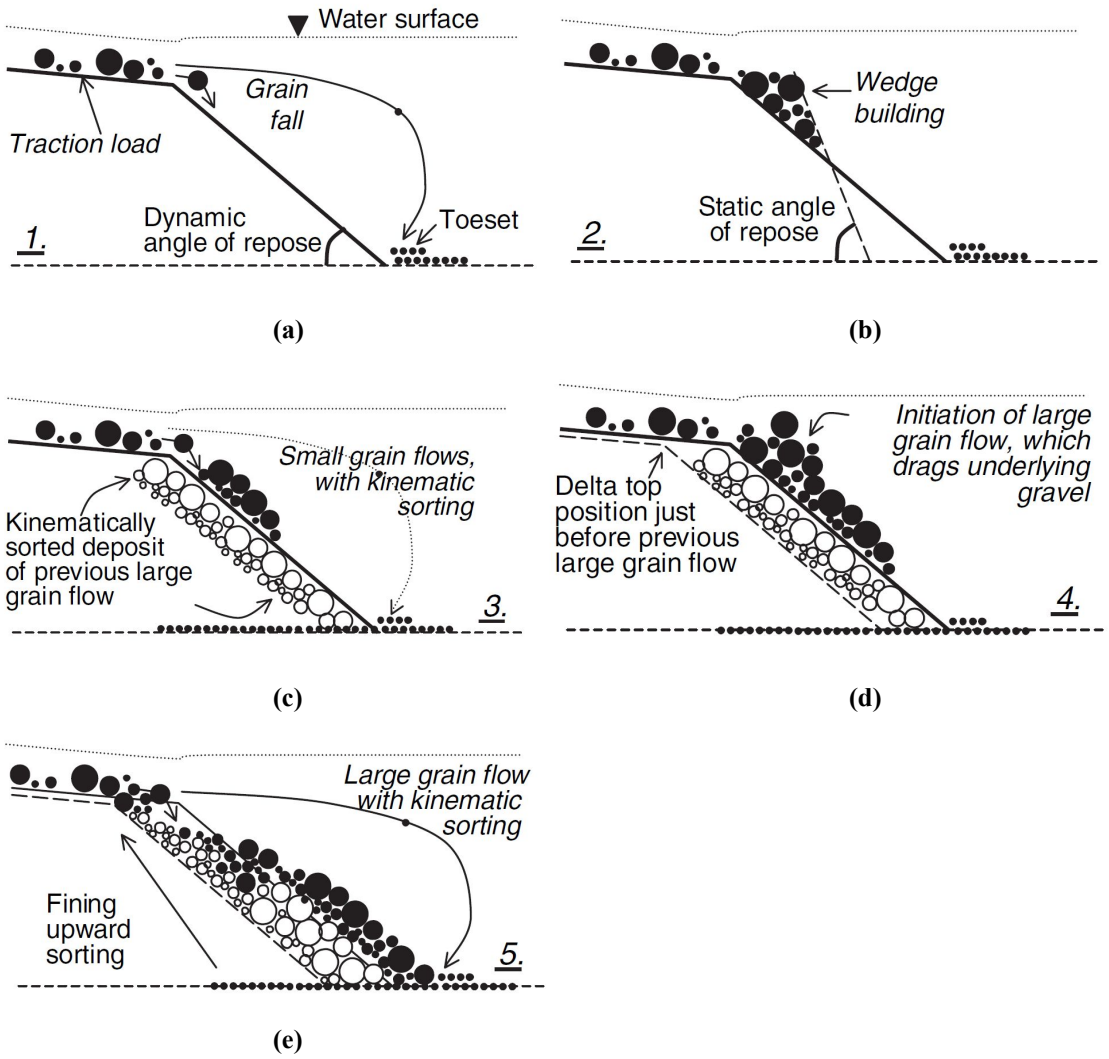

Figure 1.3.3: Sketch detailing the sorting mechanisms present at the lee slope of a delta from Kleinhans (2005). The first step is described in **(a)** and **(b)** where grain fall creates the sediment wedge at the upper end of the foreset and small grains fall to the bottomset. The second stage is shown in **(c)** with kinetic sieving and small grainflows. **(d)** and **(e)** display the large grainflows that pull large particles down slope and generate upward fining.

1.3.4 Comparison of Terminology

While it is helpful to consider the physical analogies between natural deltas and similar landforms in oil sands tailings ponds, there are a number of terminology differences that can cause confusion. For the purposes of this report, we attempt to clarify these differences by a brief overview in this subsection that helps identify our

deposit and its processes with the following terms as exhibited in **Figure 1.3.4**. We first define our basic deltaic features. We also demonstrate the release of sediment down the length of the foreset or an avalanche. Additionally, we display the action of settling that occurs downstream of the topset.

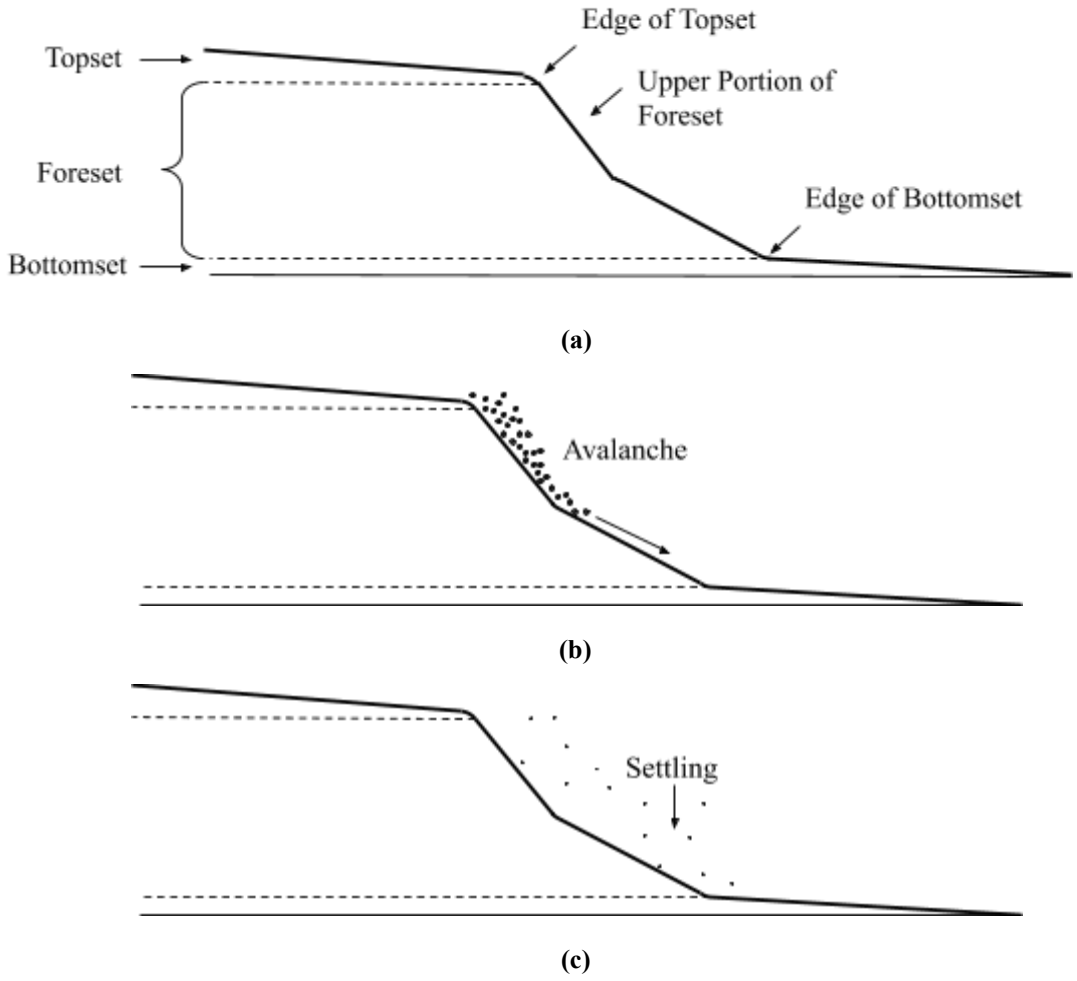

Figure 1.3.4: **(a)** Defines certain deltaic features, **(b)** conveys what we call an avalanche or a release of sediment down the length of the foreset, and **(c)** shows the settling that occurs along the foreset and farther downstream.

The terms Kleinhans uses for these features and phenomena are shown in **Figure 1.3.5**. Whereas we define the lowest deposit layer as the bottomset, Kleinhans identifies this layer as the toeset. Kleinhans uses the term grainflow to describe the action of

sediment travelling down the front of the deposit and grain fall to signify the deposition of sediment that occurs along the front.

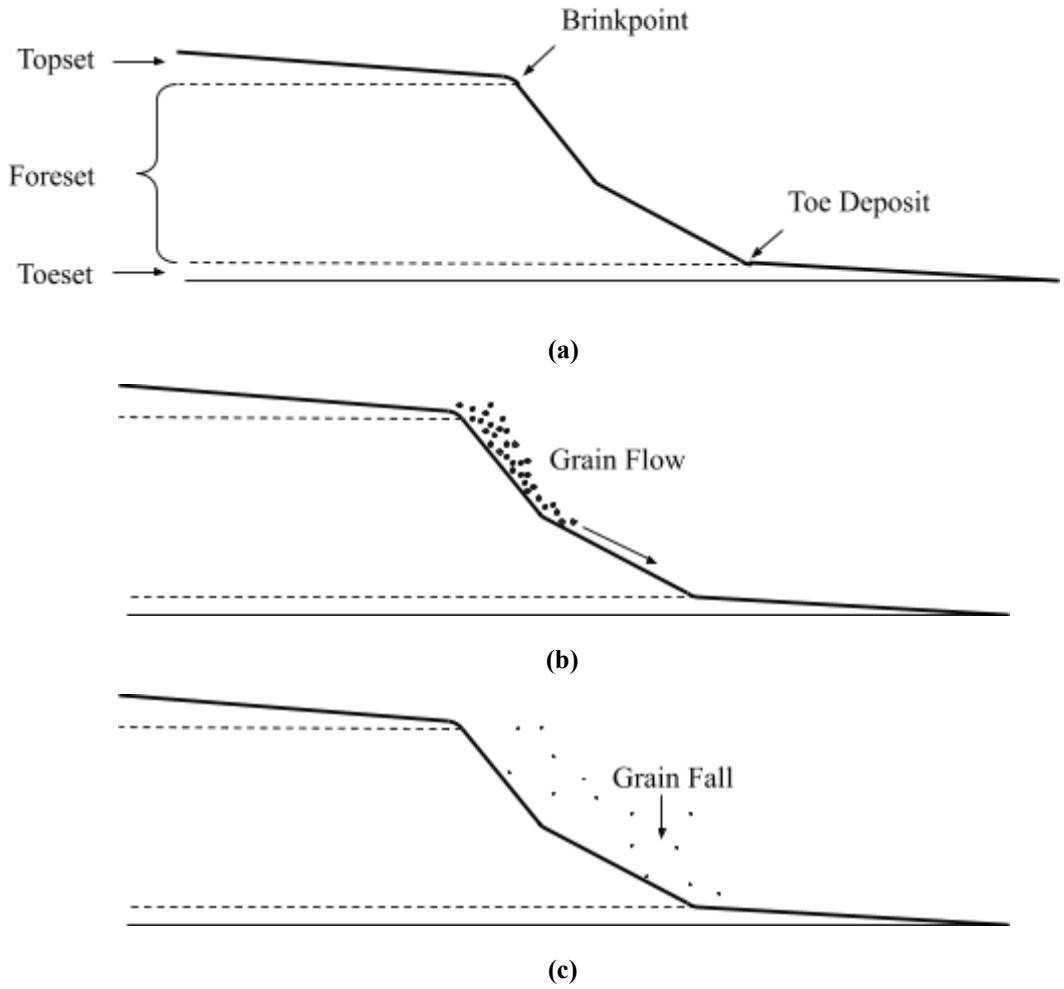

Figure 1.3.5: **(a)** Kleinhans defines deltaic features, **(b)** describes what Kleinhans calls a grain flow or a release of sediment down the front, and **(c)** portrays grain fall, the term Kleinhans uses to describe the deposition that occurs along the delta front.

Figure 1.3.6 conveys the terms that the oil sands industry uses for the landforms present in a delta. The oil sands industry defines the topset as the Beach Above Water (BAW) and the foreset and bottomset as the Beach Below Water (BBW).

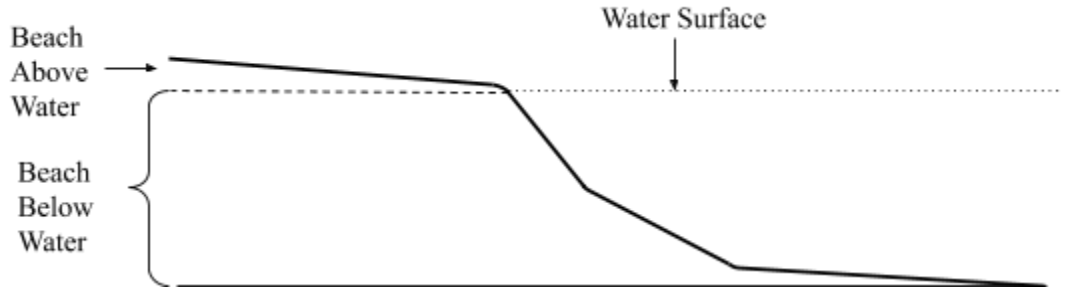

Figure 1.3.6: Terminology used by the oil sands industry to describe the two sections of a delta: Beach Above Water (BAW) and Beach Below Water (BBW).

1.3.5 Potential Lessons Learned Toward Faster Remediation of Tailings Ponds

If we can show that a surrogate mixture behaves similarly to actual oil sands tailings and these tailings behave similarly to naturally formed deltas, then we can use the information obtained from the surrogate mixture to learn more about the mechanisms involved in the formation of oil sands tailings deltas.

In developing the plan of study for the work described in this thesis, we chose to use what we call surrogate mixtures as preliminary work toward studying the actual oil sands tailings systems for several reasons. First, compared with actual oil sands tailings, we are not restricted to the concentrations of components in any particular delta on any particular pond. So, we are able to vary components systematically to better understand how different boundary conditions such as concentration, flow discharge and particle size distribution affect the segregation patterns and related behavior. Second, if chosen carefully, our surrogate materials create a natural connection between natural materials that build into natural deltas and oil sands so we can make a clear bridge between mechanistic behaviors of the different substances. Third, there are several moderate hazards associated with handling oil sands associated with the solvents and bitumen traces in the material. Working initially with materials where we didn't have to worry about the hazards allowed us to develop experimental practises toward investigating the physical behaviors independently from safety practises to keep the personnel and

environment from being negatively affected from aeration and containment procedures to safety clothing.

1.4 Summary

To summarize the introduction presented in this Chapter: the oil sands industry is presently working diligently to discover ways to substantially enhance the performance of existing oil sands tailings ponds due to growing environmental concerns. A more in-depth knowledge of the physical transport and segregation behaviors of tailings materials, specifically TSRU tailings, would be beneficial for the advancement of the reclamation process. We hope to achieve a better understanding of these behaviors with the intention of advancing the processes currently implemented in the field. To accomplish this, we must first interpret the situations present in the field and then investigate simple techniques that the oil sands industry can incorporate into their deposition process. This work has the potential to lessen the impact of tailings and provide relief for the producers.

The largest issue common in the reclamation process used by the oil sands industry today is the slow settling rate of fine particles relative to larger particles. We hypothesize that if the fine and coarse particles were able to somehow settle together that there would be less segregation and therefore the ponds would be more stable. Before this idea can be explored, a greater understanding of the concepts behind the sorting mechanisms is required as well as an examination of the conditions that reduce the amount of sorting. For our experiments, these ideas would be explored by varying the dynamics to allow for more mixing to occur. In the future, other researchers will have the opportunity to further investigate into the relative stability of unsegregated mixtures and compare their results to successfully segregated fine and coarse particle systems. It is clear that unmixed deposits are undesirable for ponds due to the fact that the fine particles hinder the reclamation process by settling at slower rates and not naturally dewatering. We hypothesize that if some of the fines were to intermix with the coarse particles

present on the beaches of the ponds, a stable beach would still be produced. It would be beyond the scope of this thesis to determine the exact concentration of fines in the coarse deposit that would still result in a stable beach. We are hopeful that the methods we investigate in this thesis will assist the industry in identifying the general dynamics present in their deposits and subsequently adjust these dynamics to provide a more desirable outcome.

To date, very minimal research has been conducted on TSRU tailings which demonstrate a unique physical composition and dynamic morphology. We propose a study which would use an alternative to TSRU tailings that still exhibit similar characteristics in order to examine the deposition, segregation, and transport behaviors of the materials. We have confidence that a well-designed laboratory study can be used to test these behaviors by sending different surrogate mixtures at varying rates through a narrow flume and observing the deposit formed.

The remainder of this thesis covers the following topics. In **Chapter 2**, we include a detailed description of our experimental methods. For **Chapter 3**, we cover our work with a simple surrogate mixture consisting of anthracite coal and kaolinite clay. Then we discuss our work with a more complex surrogate mixture of anthracite coal, kaolinite clay, and silica sand in **Chapter 4**. Finally, we review our findings, discuss any issues we faced, and explore future directions for this research in **Chapter 5**.

Chapter 2 - Methods

The goal of this work was to study dynamics such as deposition and segregation of sediment during the formation of a deltaic landform. To study these behaviors systematically, we decided that a 2-dimensional flume would provide an ideal geometry. We used operational information and measured geometries of field-scale tailings beaches to design the experimental facility which we discuss below in detail.

2.1 Qualitative Descriptions of Field-Based and Experimental Channels

2.1.1 Field-Based Depositional Setting

As discussed in **Chapter 1**, once the mined oil sands have been processed and the bitumen extracted, the tailings, in the form of slurry of particles, water, and traces of other substances, are discharged from a horizontal pipe and into a large pond. With time, a deposit or a beach forms near the end of the pipe primarily from the larger particles in the slurry. The smaller and lighter particles are carried with the fluid past the beach into the pond.

The deposit of the largest particles is often described as two distinct regions. The segment of the deposit that is below the surface of the pond is called the Beach Below Water (BBW) and the portion that is above the water surface is called the Beach Above Water (BAW). As evident from satellite images from actual tailings beaches, seen in **Figure 1.3.1 (a)**, the tailings deposit that grows outward from the point of discharge strongly resembles natural river deltas with numerous braided channels that lead to the pond. As is true of natural river deltas, several of the channels are active at any given time, as the material discharged from the pipe spontaneously divides among the active channels. Some of the larger particles within the slurry deposit along the channels until they reach the point where the channels meet the edge of the BAW. This depositional process adds vertically to the BAW along particular channels. Over time, these channels

migrate across the entire topset resulting in a relatively flat surface. Most of the large particles that do not deposit from the slurry along the top surface of the landform avalanche down the BBW prograding the landform relatively symmetrically. The rest of the particles continue in suspension with the fluid into the pond to settle much more slowly.

2.1.2 Laboratory-Based Model Framework

To experimentally model this process, we consider a more idealized configuration of these tailings ponds deltas. We consider a delta without any winding channels i.e. with channels that span radially outward from the pipe as in **Figure 2.1.1**. In our experimental design, we model just one of these active channels, over which we expect the particles to be leaving the discharged slurry. We sketch what we expect the dynamics in a cross section of such a channel to resemble, essentially a Gilbert-style delta. For our experimental design, we focused on this particular framework.

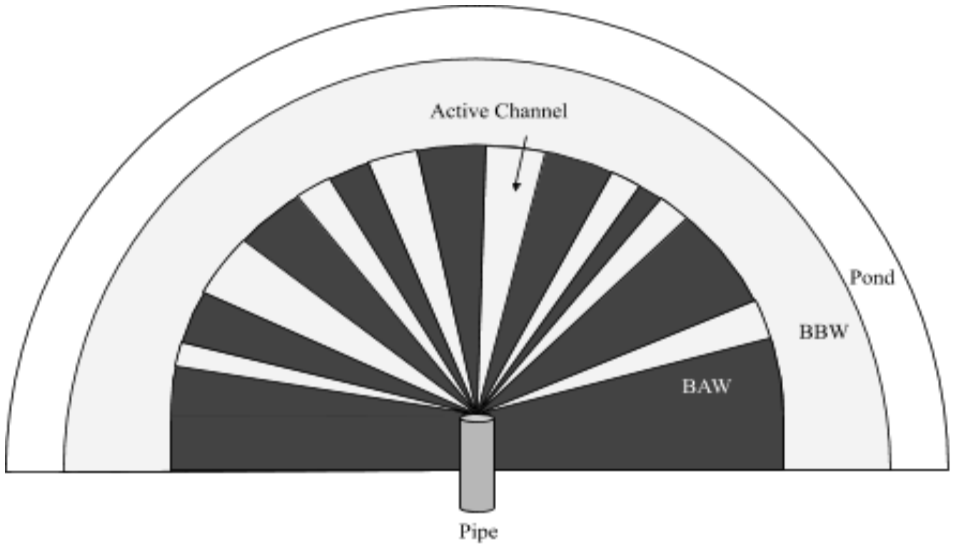

(a)

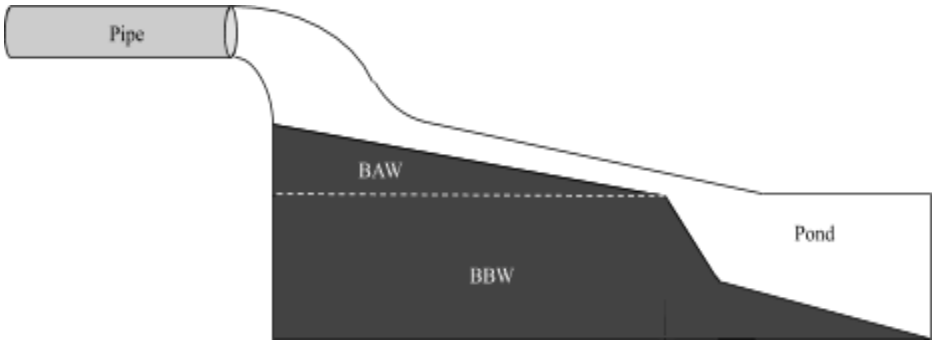

(b)

Figure 2.1.1: Simplified representations of the idealized situation in the field presented **(a)** as a top view sketch with all flow traveling radially outward and **(b)** a side view sketch of flow leaving the pipe and forming the beach. This situation includes a Beach Above Water and a Beach Below Water with a pond.

In order to design a flume that quantitatively matched the field conditions, we used field data as described in the next section.

2.2 Image Analysis of Field Data

One set of field data we used for our experimental design involved a series of satellite images we received from industry consisting of deltaic landforms around oil sands ponds such as those shown in **Figure 1.3.1 (a)** and idealized in **Figure 1.3.1 (b)**. Accompanying these were TSRU tailings pipe discharge rates were received from industry. The rates of discharge from the pipes range from 0 to 4000 m^3/hr with average densities ranging from 1000 to 1150 kg/m^3. **Table 2.2.1** contains these values for discharge and density. These readings were recorded for an oil sands tailings pond between July 19, 2014 and February 17, 2017. Any values we were not provided with are left empty.

Date	**Discharge (m^3/hr)**	**Density (kg/m^3)**	**Second Flow Rate (m^3/hr)**	**Second Density (kg/m^3)**
July 19, 2014	2600	1000	-	-
March 30, 2015	2500	1000	-	-

July 29, 2015	2500	1040	4000	1000
September 9, 2015	2200	1020	3500	1000
May 5, 2016	3000	1000	1950	1000
September 22, 2016	0	1600	2500	1040
February 17, 2017	2150	1000	2200	1150

Table 2.2.1: Tables containing the flow rates and density readings for an oil sands tailings pond on various days between July 19, 2014 and February 17, 2017. The values not provided are left empty.

A satellite image of a tailings pond delta can be seen in **Figure 2.2.1**. The pond shown in **Figure 2.2.1** contains TSRU tailings that were produced after removing any remaining solvent. We used the information contained in satellite images similar to **Figure 2.2.1** along with operational information at the time the photo was taken to approximate average discharge along each estimated 2D channel.

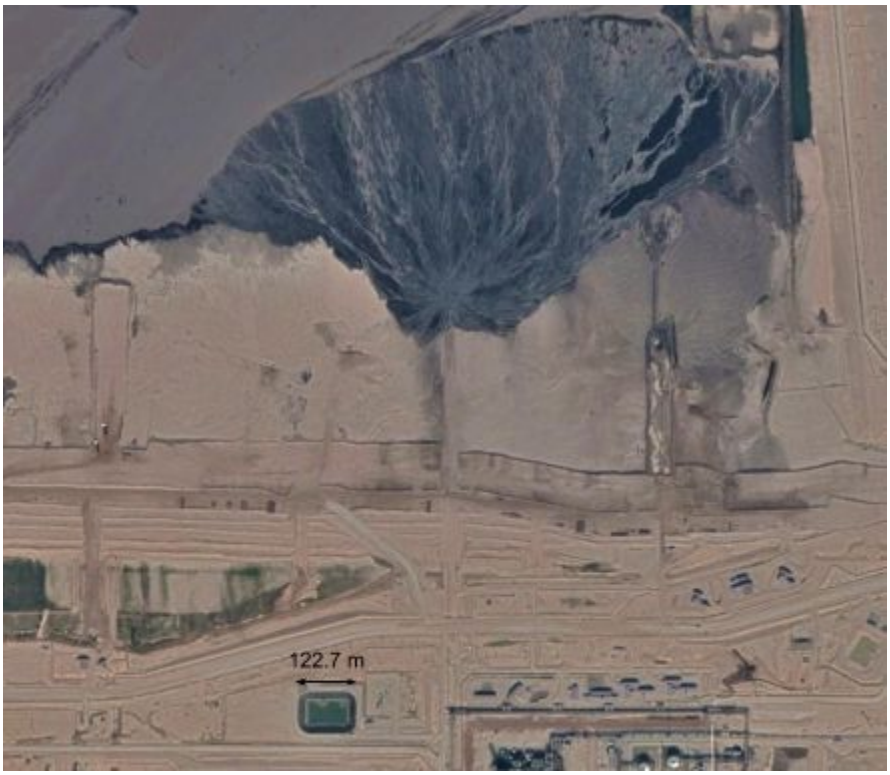

Figure 2.2.1: Satellite image of a tailings delta including a scale of 122.7 meters. This pond contains TSRU tailings produced through the process of striping-off and recycling any remaining solvent from the tailings before they are deposited in the pond, discussed in **Chapter 1**. This image was taken on July 17, 2016.

We processed satellite images of the deltas to approximate the average unit discharge at the time the photographs were taken to determine appropriate discharge rates for laboratory flumes. The procedure we used for this is as follows. For unit discharge for a particular fan of interest at a particular distance from the point of discharge from the pipe, we drew a circle with radius, R, of 125 m over a corresponding image with the center positioned approximately at the pipe exit. We chose the location of each circular segment so that the upstream channels were still traveling radially outward i.e. before they started twisting and turning. We then divided each circular segment evenly into 18 slices, N, each occupying 20 degrees of the circle. **Figure 2.2.2 (a)** shows an example. We call the outside edge of a slice a segment and illustrate a segment and a slice in **Figure 2.2.2 (b)**.

(a) **(b)**

Figure 2.2.2: **(a)** A satellite image of a tailings delta similar to that used for this research taken on July 17, 2016. A circle with a radius of 125 meters was drawn over the estimated exit of the pipe. **(b)** The circle was split into 18 slices and the flow through the end of each of these slices i.e. a segment was estimated. A slice is indicated in red and the segment is indicated by the yellow.

To approximate the unit discharge, we examined all of the segments for evidence of flow at the time the photograph was taken. The total wetted length is calculated according to

$$L_w = \frac{N_f \times \pi \times R}{9} \qquad \textbf{Equation 1}$$

where N_f is the number of segments determined to contain some flow and R is the radius of the circle. Following this, we estimate the unit discharge for each of the segments as

$$q = \frac{F_f \times Q}{L_w} \qquad \textbf{Equation 2}$$

where F_f is the fraction of flow occurring through each segment and Q is the pipe discharge at an instant in time shown in a particular image (see **Table 2.2.1**). By looking at all of the unit discharges for each of the segments, we found the minimum, maximum, and average unit discharges for each of the days we had received data for. We used these unit discharge values to calculate the total discharge for a reasonable flume width of 4 inches. We determined a flume width of 4 inches was wide enough so that an arm could reach into the flume for cleaning and data collection purposes. We provide discharge rates for such a flume in **Table 2.2.2**.

Date	**N**	**Q (m^3/hr)**	**N_f**	**L_w (m)**	**q_{min} (m^2/s)**	**q_{max} (m^2/s)**	**q_{avg} (m^2/s)**	**$Q_{min,4}$ (L/s)**	**$Q_{max,4}$ (L/s)**	**$Q_{avg,4}$ (L/s)**
July 19, 2014	18	2600	6	262	0.00166	0.00414	0.00276	0.168	0.421	0.281
March 30, 2015	18	2500	5	218	0.00319	0.00319	0.00319	0.324	0.324	0.326
Sept. 9, 2015	18	5700	8	349	0.000726	0.0145	0.00668	0.0738	1.48	0.679
May 5, 2016	18	4950	11	611	0.000631	0.00631	0.00225	0.0641	0.641	0.229
Sept. 22, 2016	18	2500	14	698	0.000159	0.00207	0.001	0.0162	0.210	0.101

Table 2.2.2: Table of results from image analysis of satellite images where N is the number of slices/segments, Q is the total discharge, N_f is the number if segents occupied by flow, L_w is the total wetted

segment length, q_{min} is the minimum unit discharge, q_{max} is the maximum unit discharge, q_{avg} is the average unit discharge, $Q_{min,4}$ is the minimum discharge for a 4 inch wide flume, $Q_{max,4}$ is the maximum discharge for a 4 inch wide flume, and $Q_{avg,4}$ is the average discharge for a 4 inch wide flume.

2.3 Experimental Flume

2.3.1 Flume Dimensions

We present a top view and side view sketch of the flume without instrumentation in **Figure 2.3.1**. The materials are initially discharged through the pipe into the flume where they are allowed to flow over the upstream weir before forming the BAW and BBW. Much of the fluid that enters the flume collects in the pond. Any excess materials flow over the downstream weir.

(a)

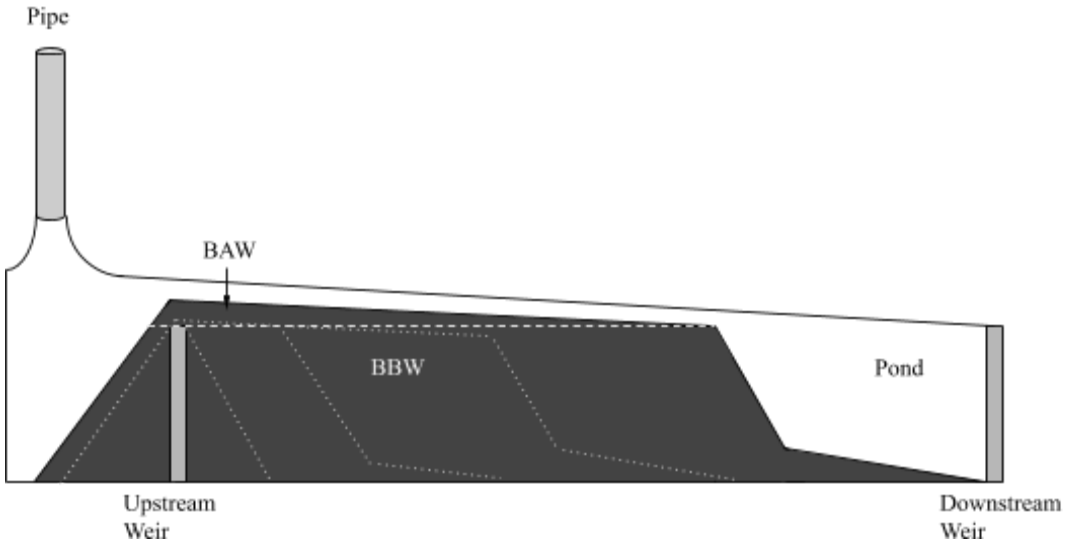

(b)

Figure 2.3.1: (a) Top view of experimental channel. As more material entered the flume, the BAW prograded downstream toward the end of the flume. **(b)** Side view of the experimental channel. The materials enter the flume and pass over the upstream weir before forming the BAW and BBW. As time passes, the surface of the beach builds up and forms a Gilbert delta as indicated by the white dotted lines

Once we used the method described above to determine the flume design, we worked with the technical staff at St. Anthony Falls Laboratory (SAFL) at the University of Minnesota (UMN) on the more detailed design and build of the flume. The flume used for these experiments was designed and built by SAFL technical staff members who have designed, built, and worked with many similar flumes in the past.

In addition to the determination of discharge and flume width described in section **2.2**, we kept a number of other goals in mind while determining the flume dimensions with the SAFL staff. These goals included: (1) minimizing the volume of materials needed for a single experiment, (2) minimizing frictional wall effects, and (3) minimizing hazards associated with splashing over the flume edges.

With these considerations in mind, we worked with the SAFL staff to determine the geometry of the flume. Based on experience, the SAFL staff designed the flume walls to be 50 cm high: a height that was sufficient to avoid splashing but still shallow enough

for someone to reach inside the flume. The flume length was designed to be 10 m, adequately long for the front of the deposit to reach a position far enough downstream to be independent of initial conditions.

As mentioned previously, based on experience, we determined the width of the flume needed to be at least 10 cm or approximately 4 inches so that a researcher could reach his or her arm into the flume for data collection, cleaning, and other purposes. Based on our calculated unit discharge rates described above in **Table 2.2.2**, the discharge rates needed for such a flume vary from 0.1 L/s to 0.7 L/s. These were obtainable discharge rates for a laboratory pumping system. We provide a computer-aided sketch of the flume in **Figure 2.3.2**, created by SAFL staff member, Aaron Ketchmark.

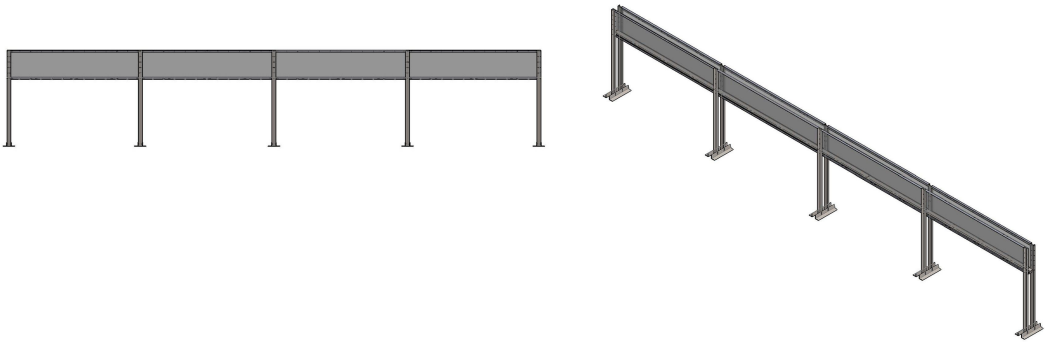

(a) **(b)**

Figure 2.3.2: Sketch of the experimental flume from the side **(a)** and from the side, slightly above the top of the flume **(b)**. The flume had a length of 10 meters, a height of 50 centimeters, and a width of 10 centimeters. The walls of the flume were made of transparent Plexiglas and the frame and supports were made of aluminum. One end of the flume was closed with a Plexiglas wall and the other was open so an adjustable weir could be attached. This image was created by SAFL staff member, Aaron Ketchmark.

2.3.2 Flume with Inlet and Outlet Structures

The flume had a few additional features to help us achieve our desired boundary conditions. We included a sharp-crested weir at the downstream end of the flume to

establish a constant downstream pond elevation of 15 cm. We installed a vertical pipe to input materials into the upstream end of the flume in a spatially efficient manner. Slightly downstream of the inlet, we installed a 15 cm tall weir to establish a "stilling basin" to dissipate bigger vortices that might otherwise dominate the deposit dynamics. In other words, the stilling basin served to dissipate some of the energy of the incoming materials and to help minimize erosion from these large scale structures. To summarize, we designed the upstream structures to: (1) discharge the surrogate particle-fluid mixture into the stilling base, (2) dissipate the forceful organized energetic eddy-like behavior, and (3) allow the material to pass over the upstream weir and move into the main body of the flume in a much smoother laminar-like manner. While the particles deposited along the base, the downstream structure kept the far-downstream pond level at its initial 15 cm height.

Details about the flume and the other experimental apparatus are included in the next section.

2.4 The Composite System

In addition to the flume itself, we used several additional pieces of equipment in our experimental runs. We present a diagram of the experimental setup in **Figure 2.4.1**. We used a large, cubic meter-sized tank to hold the materials prior to their discharge into the flume with an opening on the top through which we inserted an industrial-sized mixer to mix the materials.We also installed a spout near the bottom on the side where the materials could exit the tank.

We connected the bottom opening of the tank to the discharge pipe at the upstream end of the flume through a pump, two series of pipes, and a constant head tank. We will discuss the pump in section **2.4.1**. A series of constant diameter pipes connected the pump to the constant head tank. The constant head tank was made from a transparent material so that the pump operator could see the level inside the tank and appropriately adjust the pumping speeds until the mixture was at a constant, predetermined level,

indicated by a black line on the tank. We connected the outlet from the constant head tank to the flume with a series of pipes of decreasing diameters to minimize settling of the particles from the mixture before they entered the flume.

At the end of the piping system, just before the flume, we attached a pre-calibrated orifice designed to control the flow rate at a predetermined discharge. We were able to adjust the flow rate of the materials entering the flume by attaching different sized orifices in this location. After passing through the orifice, the mixture freely entered the flume.

The flume was constructed from Plexiglas and had dimensions of 10 meters in length, 50 cm in height, and 10 cm in width. As discussed above, once the mixture entered the flume, some of its energy was dissipated behind the upstream weir before it entered what we call the pond. Both this upstream weir and the downstream sharp-crested weir attached to the downstream end of the flume set the pond level inside of the flume. Whatever materials passed over the downstream weir, deposited in a large, exit tote.

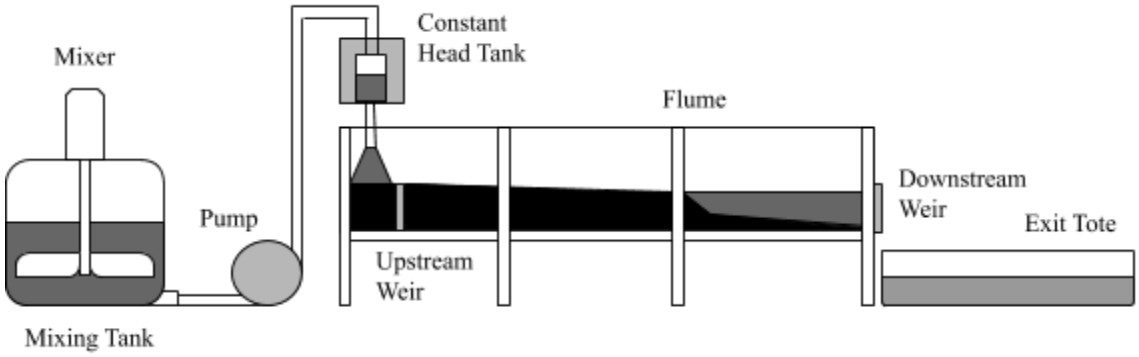

Figure 2.4.1: Diagram of complete experimental setup. A mixer placed on top of the mixing tote mixed the materials. A pump was used to pump the mixed materials from the mixing tote to the head tank. A weir was located inside of the head tank so that a steady flow could be achieved. A pre-calibrated orifice was placed at the end of the pipe so that a known flow rate could be determined. After leaving the pipe, the material was allowed to settle or travel through the flume. The flume had a length of 10 meter, a width of 10 centimeters, and a height of 50 centimeters. Two weirs were placed in the flume so that a water level could be set. Any material that passed over the lower weir was deposited in the exit tote.

2.4.1 Pumping System

For the experiments described in this thesis, we used a diaphragm pump to deliver our surrogate mixtures from the mixing tank to the flume. A diaphragm pump uses compressed air to actuate two diaphragms that expand and contract to create flow in a pipe system. The advantage of a diaphragm pump in this application is that particles can remain intact, not broken down, as they are drawn through the pumping mechanism. Further, the flow rate could be relatively easily controlled by adjusting air pressure: the air supplied to the diaphragm pump controls the rate at which the pump delivers materials. A diagram of the basic mechanics of a diaphragm pump is included in **Figure 2.4.2**.

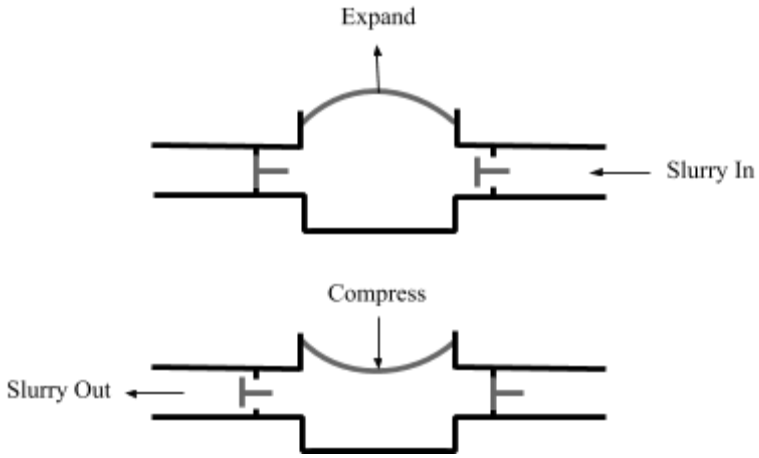

Figure 2.4.2: Simple diagram of a diaphragm pump. When the diaphragm expands, the first valve opens and the slurry enters the chamber. As the diaphragm compresses, the second valve opens and the slurry flows out of the pump.

For the purpose of these experiments, we equipped our pumping system with a Versa-matic E4 diaphragm pump. This particular pump has a flow rate range between 0 and 70 gpm or roughly 4.4 L/s which encompassed the pumping requirements necessary for these experiments.

2.4.2 Mixer and Mixing Tank

To mix the materials before we pumped them into the flume, we used an industrial-sized mixer in our mixing tank. A Variable Frequency Drive (VFD) was attached to the mixer motor allowed for us to control the speed at which the mixer would operate. **Figure 2.4.3** shows a picture of the tank with the mixer mounted on top. Difficulties associated with the mixing tank are discussed later in **5.2.2 Mixing Complications**.

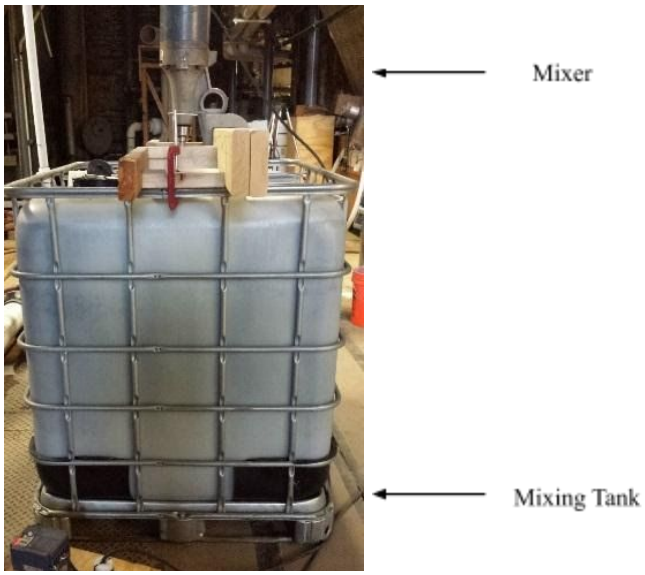

Figure 2.4.3: Photograph of mixing tank with the industrial-sized mixer attached to the top of the 1000 L tank.

2.5 Experimental Materials

All experiments were performed in this thesis using one of two mixtures we considered reasonable surrogates for TSRU tailings based on certain similar characteristics. We determined the composition of the surrogates by comparing the behavior of a small sample of TSRU tailings with several mixtures of materials readily available at SAFL. We found the volumetric concentration of water in the TSRU tailings

to be 95% and made test surrogate mixtures that were similar. Then we investigated settling behaviors of the TSRU mixtures and potential surrogate mixtures. We discuss the results of these tests in detail in sections **3.1.1** and **4.1.1**.

In the end, we found the most suitable mixture consisted of anthracite coal and kaolinite clay in water, as we discuss in **Chapter 3**. We also ran experiments with a mixture composed of anthracite coal, kaolinite clay, and silica sand in water, as we discuss in more detail in **Chapter 4**. We present the grain size distributions for anthracite coal, kaolinite clay, and silica sand in **Figure 2.5.1**.

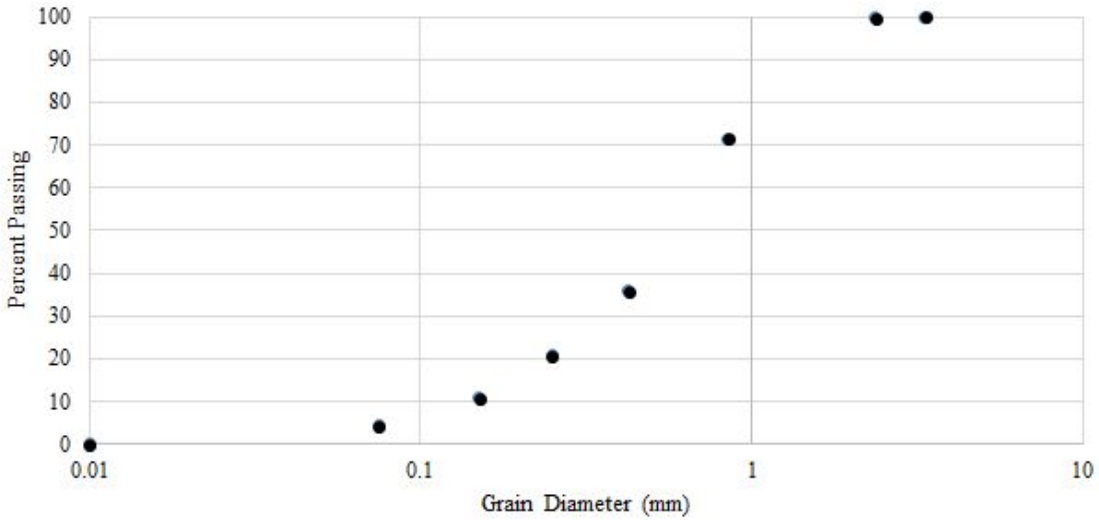

(a)

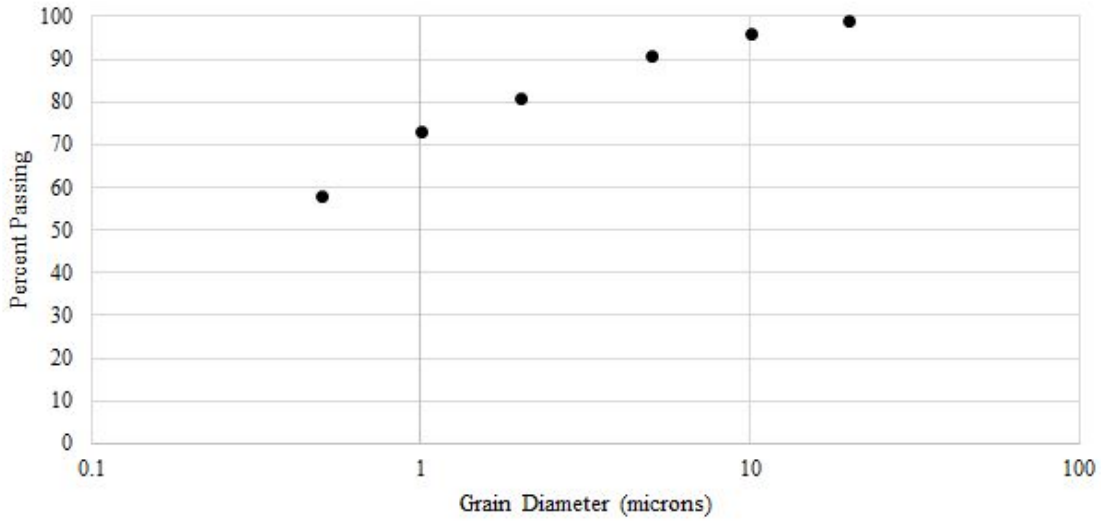

(b)

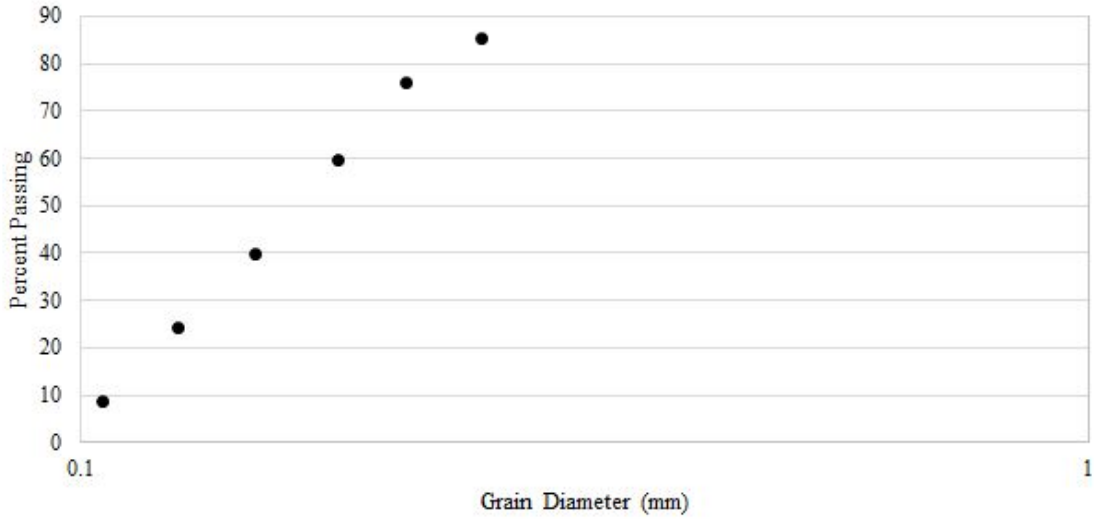

(c)

Figure 2.5.1: Percent finer plots for **(a)** anthracite coal in millimeters, **(b)** kaolinite in microns, and **(c)** silica in millimeters. The data for all of the plots was provided by the manufacturers.

We determined the median grain size and other characteristic grain sizes from the Material Safety Data Sheets (MSDS) for the three materials, as shown in **Table 2.5.1**.

Grain Size (microns)	Anthracite Coal	Kaolinite Clay	Silica Sand
D_{15}	186	-	112

D_{50}	560	0.5	164
D_{85}	1389	-	247

Table 2.5.1: Table of D_{15}, D_{50}, and D_{85} for anthracite coal, kaolinite clay and silica sand in microns.

The experimental parameters for experiments A02 and A03 are documented in **Table 2.5.2** and in **Table 2.5.3** for A05 and A06. These tables include the flow rates, densities, sediment by volume percentages, and percent by volume values for the four materials.

	Experiment	**A02**		**A03**	
	Flow Rate (L/s)	0.5		1.0	
Material	**Density (g/ml)**	**% Sed. by Vol.**	**% by Vol.**	**% Sed. by Vol.**	**% by Vol.**
Coal	1.495	89	4.5	89	4.5
Clay	2.82	11	0.5	11	0.5
Silica	2.77	0	0	0	0
Water	0.9982	-	95	-	95

Table 2.5.2: Table of experimental parameters during runs A02 and A03.

	Experiment	**A05**		**A06**	
	Flow Rate (L/s)	1.0		0.5	
Material	**Density (g/ml)**	**% Sed. by Vol.**	**% by Vol.**	**% Sed. by Vol.**	**% by Vol.**
Coal	1.495	44.7	2.3	44.7	2.3
Clay	2.82	10.7	0.5	10.7	0.5
Silica	2.77	44.7	2.3	44.7	2.3
Water	0.9982	-	95	-	95

Table 2.5.3: Table of experimental parameters during runs A05 and A06.

2.6 Experimental Procedure

The entirety of the surrogate experiments were performed at the University of Minnesota's St. Anthony Falls Laboratory in Minneapolis, Minnesota. Each experiment required several days of preparation as well as tasks performed during and after the run concluded. In the following sections, we discuss the procedures that we executed before, during, and after the experiment.

2.6.1 Summary of Procedures Performed Prior to Each Experiment

Before starting the experiment, we needed to perform several tasks to prepare for each experiment. Firstly, we cleared all of our equipment of any residue such as that remaining from previous runs. This required filling the mixing tank with water and running the water through the pump, head tank, and flume several times. Next, we cleaned out the flume so that no marks or smudges could be seen on the walls of the flume so that the evolution of the mixture could be readily seen through the side walls. Then, we installed the upstream weir by taping it to the inside of the flume near the inlet, and we installed the downstream weir by clamping it to the downstream end of the flume. Once we had the weirs in place, we filled the flume with water i.e. with a hose until water poured over the top of the downstream weir into the exit tote. We also attached the inlet orifice that gave us our desired flow rate of surrogate tailings into the flume.

We then prepared the mixture by pouring the appropriate amount of the solid components into the mixing tank. We filled the remainder of the mixing tank with water until the level reached 1000 liters. While the water was being added, we started the mixer at a low mixing speed. The mixer was able to mix at an adjustable rate until the mixture was deemed well-mixed i.e. there were no visible distinctions between the different components inside the tank.

Outside of the flume, we placed video cameras on tripods near the first half of the flume to capture the formation of the deposit and construction lights were placed near the cameras to provide the proper lighting. Specifically, we placed three Canon GL2 and one Canon Vixia HF200 on tripods as in **Figure 2.6.1**. We adjusted the height of the tripods so that the base of the flume appeared at the base of each image. The cameras recorded in progressive framing with 60 frames per second. We focused each of the cameras on the inside surface of the flume and set to manual focus with a meter stick or measuring tape within the view of the cameras.We placed white foam boards were attached to the backside of the flume to provide a simple background for the videos and to keep the video cameras from focusing on objects behind the flume.

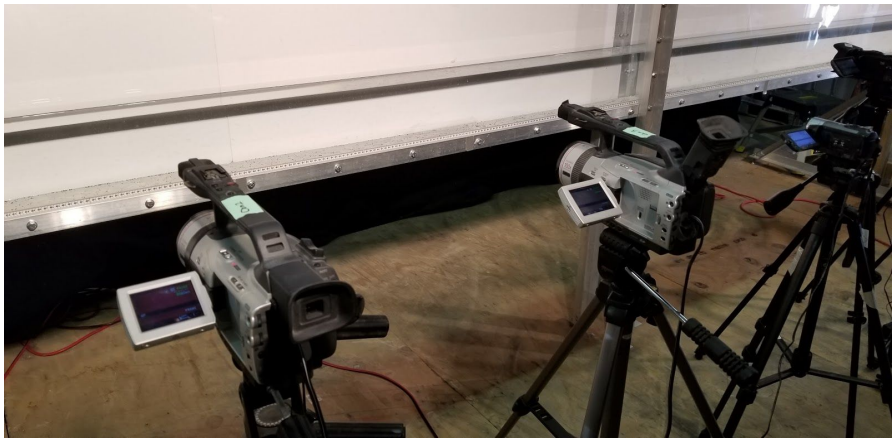

Figure 2.6.1: Picture of video cameras on tripods approximately 1 to 2 feet from the side of the flume. Spotlights behind the cameras provided the lighting needed for the videos. A white backdrop was added to prevent the cameras from focusing on background objects.

Sampling bottles were also prepared before starting the experiment by labeling them with the experiment number and the time that the sample would be taken. A point gauge was placed at the downstream end of the flume that was used to measure the liquid level in the flume before and during the experiment for discharge calculations.

Several people were needed in order to run each experiment. This part of the pre-experiment setup involved distributing job assignments. One person had the responsibility of controlling the operating speed of the pump so that the level inside of

the constant head tank remained at the desired height. Another person was assigned the responsibility of measuring the downstream pond level in the flume at regular time intervals with the point gauge. We typically designated two people to capture the real-time surface of the deposit with wax pencils at certain times during the run. We also had a person pour colored sand into the flume, near the inlet, to mark the surface of the deposit at various times. One person was also in charge of taking inlet and surface samples during the experiment. One person periodically sampled materials from the inlet to make certain the materials entering the flume remained well-mixed and from the surface of the deposit to compare with the inlet samples. Finally, between other tasks, several people took turns checking the cameras to ensure they remained in focus and properly functioning.

Once all of the responsibilities were designated, the valves connecting the experimental system were opened so that the mixed material could flow to the diaphragm pump and the pump controller turned on the air so that the pumping commenced. When the material inside the head tank reached a constant level as specified by the line inside the tank, everyone started their timers at the same time and the experiment began.

2.6.2 Summary of Procedures During the Experiment

With the experiment started, everyone began tending to their tasks. The pump controller watched the level of the material inside the head tank to make sure the level did not vary too much from the predetermined height, designated with a line in the tank. If the level deviated from the desired height, the pump controller adjusted the amount of air being provided to the pump to either increase or decrease the pumping rate.

Point gauge measurements were taken during the experiment by lowering the point of the gauge to the surface of the fluid and recording the value. There were typically two people to draw the surface lines of the deposit during the run; one person started at the upper edge of the front and drew upstream and the other person started at the same spot and moved downstream in order to get the best profile of the bed in a sharp

timespan. At regular intervals, a scoop of colored sand was poured into the flume near the inlet to indicate the surface of the deposit at that specific time. The sample taker also took samples from the inlet and the surface of the deposit, near the edge of the front at designated times. All the while, one person was responsible for monitoring the video cameras to confirm video was being captured and that there were no other issues. **Figure 2.6.2** includes a photo taken of us observing an experiment.

Figure 2.6.2: Photo taken during experimental run of researchers observing formation of the deposit.

We continued to pump materials into the flume until the level inside the mixing tank was too low for the blades of the mixer to reach. Our goal for each experiment was to observe a minimum 10 m long depositional region, consisting of a minimum region of 8 m Beach Above Water region and a 2 meter-long Beach Below Water region (as defined in **Chapter 1**). Once these conditions were observed, or we ran out of materials, we ceased pumping and ended the experiment.

2.6.3 Summary of Procedures Post-Experiment

Once the pumping had ceased, and no new material was entering the flume, the fluid level inside the flume dropped to the level of the weirs and the materials in the pond began to settle, see **Figure 2.6.3**.

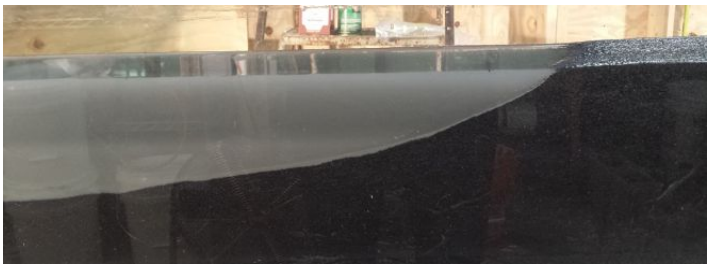

Figure 2.6.3: Picture taken of deposit shortly after pumping concluded. Clear region at the top of the pond indicates that suspended sediment in the pond started to settle out.

When the materials suspended in the pond had enough time to settle and the pond cleared, we were able to take the surface measurements of the entire deposit with the point gauge. This is explained in detail in **2.7.4 Final Surface Measurements**. We include a photograph of a deposit with a pond that had clarified enough for point gauge measurements in **Figure 2.6.4**. We attached the point gauge to the top of the flume using a clamp.

Figure 2.6.4: Picture of a deposit with a clear enough pond for surface measurements to be taken with a point gauge. The point gauge is included in the right side of the photo, attached to the top of the flume with a clamp.

2.7 Experimental Measurements

We used many measurement techniques for these experiments in order to capture the segregation, depositional, and transport behaviors.

2.7.1 Videos

As mentioned above, before starting each experiment, we placed several video cameras on tripods between 1 and 2 feet from the flume at the upstream half of the flume. We placed the cameras within a few feet of each other to capture as much of the deposit formation as possible. To prevent the cameras from trying to correct the focus while taking videos, we focused each of them on the flume wall closest to the cameras and set the cameras to manual focus. Screenshots from the footage captured by the two different types of cameras used for these experiments can be seen below in **Figure 2.7.1**. Each of the cameras captures between 1 and 2 feet of the deposit formation. We initially attached metal meter sticks and plastic rulers for scale. Later, the meter sticks and rulers were replaced by a measuring tape.

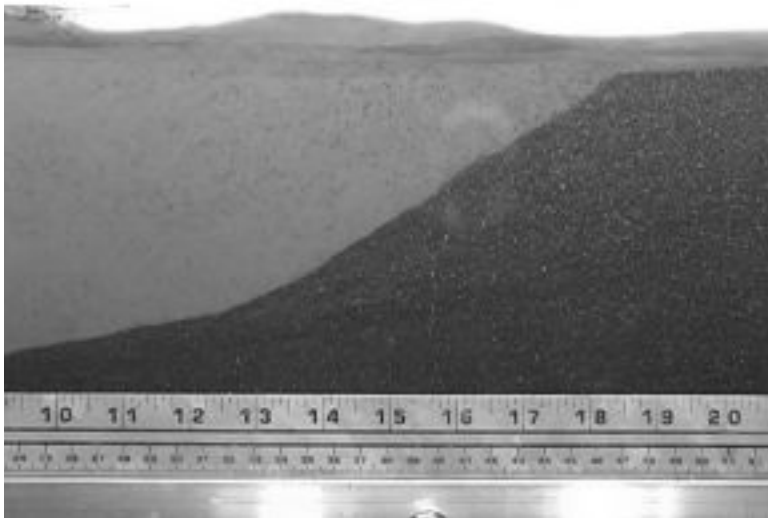

(a)

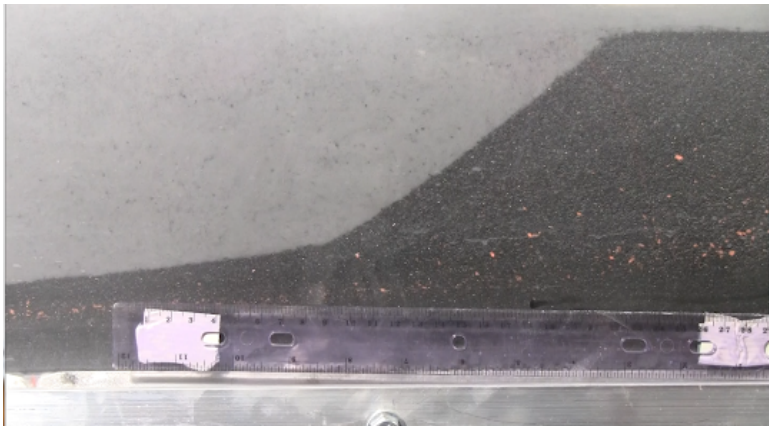

(b)

Figure 2.7.1: Screenshot of **(a)** Canon GL2 and **(b)** Canon Vixia HF200 footage of depositional formation. Each of the cameras captured between 1 to 2 feet of the formation as indicated by the scales provided in the images. Initially, we placed metal meter sticks and plastic rulers were taped to the bottom of the flume wall to provide a scale. Later, we replaced these measuring devices with a measuring tape.

The horizontal field of view for each of the video cameras ranged roughly half of a meter. We made sure that each of the cameras had a scale at the bottom of the video for later referencing and that the view included the surface of the flow inside of the flume. The videos from the cameras were used to qualitatively analyze the movement of the particles as they formed the deposit and moved downstream. The videos were also used to determine the phenomena that were occurring during each of the experiments and how these phenomena varied between experiments.

2.7.2 Surface Lines

In order to achieve a detailed record of the deposit height at specific times during the experiment for later analysis, two of us were charged with drawing the instantaneous height profile on the side wall of the flume at discrete intervals over the duration of the experiment. We have some examples in **Figures 2.7.2 and 2.7.3**. Because of the high rate of surface evolution, this process required two researchers, both starting at the current edge of the topset i.e. the front of the deposit with one drawing upstream while the other

drew downstream. The two surface profilers drew their lines every one or two minutes, depending on if the front had moved a significant distance or there was some notable formation requiring documentation. After the experiment was finished, the heights of the lines at different lengths along the flume were recorded by placing a ruler up against the Plexiglas wall and recording the values. Photos taken of the lines drawn on the side wall of the flume both during and after an experiment can be seen in **Figure 2.7.3**. The surface lines were drawn every 1 or 2 minutes throughout the experiments with wax pencils.

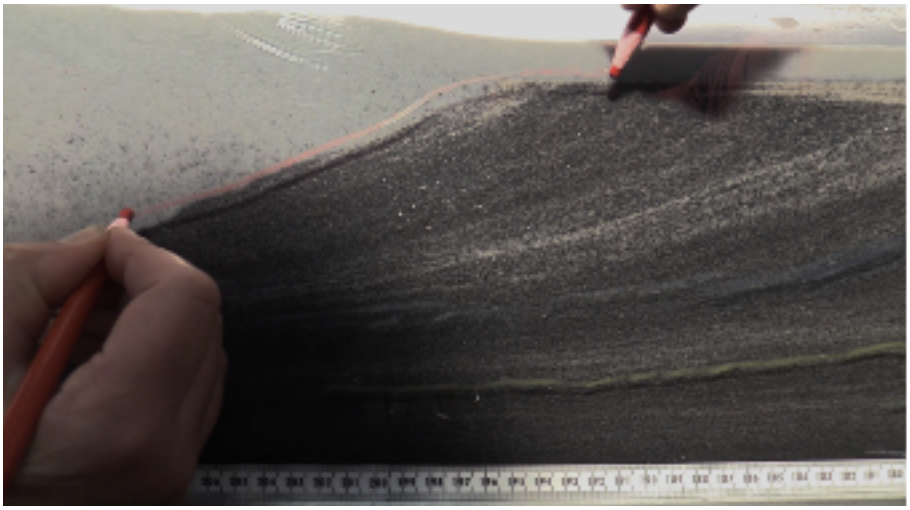

Figure 2.7.2: Picture of a surface line being drawn with wax pencils on the side wall of the flume.

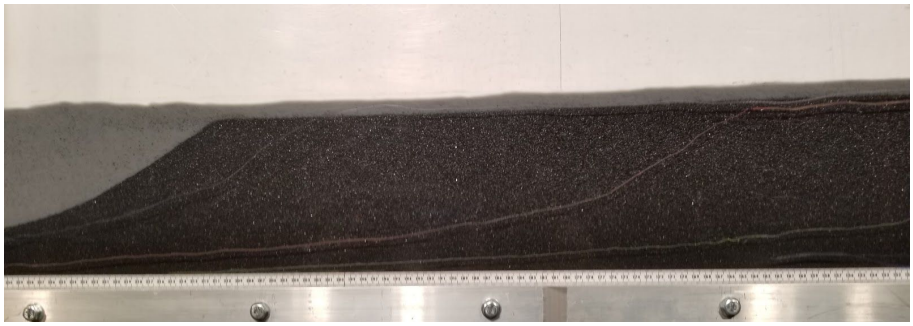

(a)

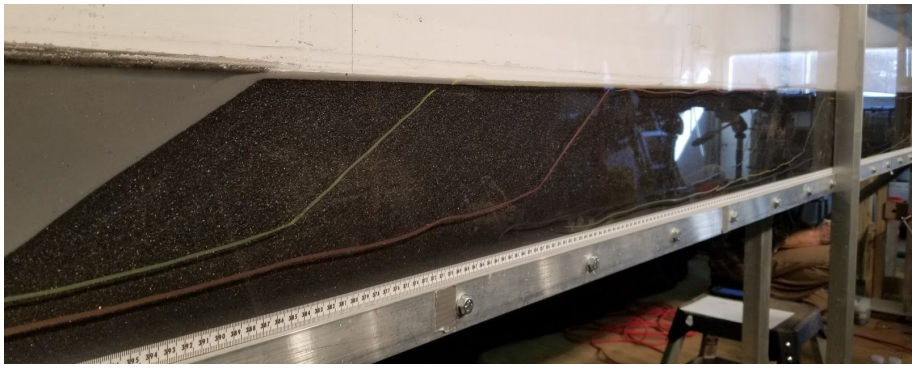

(b)

Figure 2.7.3: Pictures of the surface lines on the side of the flume taken **(a)** during and **(b)** after an experiment. The lines were drawn with different colored wax pencils at 1 or 2 minute intervals.

2.7.3 Inlet Sampling

To ensure the quality of the mixing system and the ability of the plumbing system to deliver unsegregated materials to the flume, we took samples from the head tank of the flume with a narrow scoop throughout the experiment, every 3 to 6 minutes depending on the discharge. To extract a sample, the scoop was submerged in the head tank and the contents were transferred to a sample bottle. A picture of the head tank where we took the samples is in **Figure 2.7.4**.

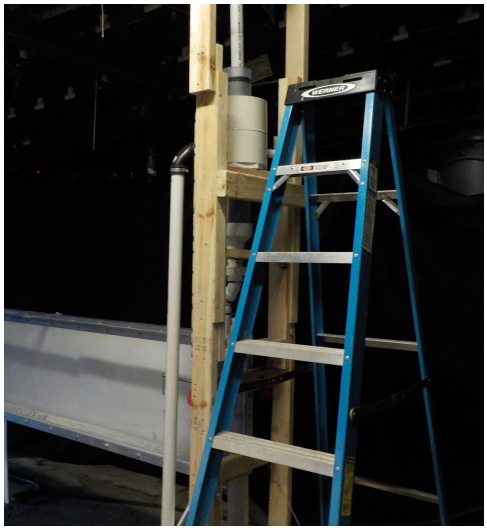

Figure 2.7.4: Picture taken of the head tank above the head of the flume. A researcher standing on the ladder shown in the image was able to dip a narrow scoop into the head tank during an experiment in order to retrieve an inlet sample.

The purpose of this information was to determine if the materials entering the flume could be considered well-mixed and remained this way throughout each experiment. After analyzing solids content data for these samples, the inlet sampling methods were deemed unfit and this data was not used. A more detailed description of this issue can be found in **5.2.1**.

2.7.4 Final Surface Measurements

A point gauge attached to the top of the flume using a clamp and was used to accurately measure the surface of the final deposit over the entire length of the flume. The point gauge provided more accurate readings of the final deposit height than using a ruler or tape measure from the side of the flume. At each location tested, the pointed tip of the point gauge was lowered until it just touched the surface of the deposit. We measured the height with the point gauge in the center of the flume since we were not concerned with the variation in the widthwise direction. In order to take point gauge measurement of the BBW or the submerged region of the deposit, we needed to wait for the pond to clarify so that the point of the gauge was visible through the liquid. We provide a picture depicting the point gauge attached to the top of the flume with a clamp in **Figure 2.7.5**.

Figure 2.7.5: Photo of the point gauge used to measure the final surface of deposits attached to the top of the flume via a clamp. Point gauge measurements were taken of the entire deposit by removing the clamp and sliding the system to a new location.

2.7.5 Coring Process

In order to get samples of the different vertical layers of the deposits, we took several cylindrical samples along the center of the flume at various locations of the final deposits. The locations from which we took these samples, i.e., the coring locations for experiment A02 are reported in **Table 2.7.1** in distance from the start of the flume in centimeters.

A02 Coring Locations (cm)
70
170
270
320
370

384
394
420
470

Figure 2.7.1: Table of coring locations for A02 in cm from the start of the flume.

We chose the coring locations for A02 roughly at 100 cm intervals. The initial core location was chosen to be 70 cm to ensure sufficient distance from the upstream boundary initial conditions. We collected core samples more frequently near the intersection of the Beach Above Water with the Beach Below Water to capture its unique behavior.

We used nine coring tubes in total, each consisting of a 13 inch-long copper pipe with a diameter of 1 inch. To ensure minimal disturbance of the sediment within each of these cores, we closed the downstream end of the flume and flooded the deposit with water to a depth greater than 13 inches. We inserted the core tubes at our chosen locations vertically with delicacy, so that there was minimal disturbance of the relative location of the sediment within the tube. We present a photograph documenting this placement of a coring tube in **Figure 2.7.6**. Once each of the coring tubes reached the bottom of the deposit, we placed a tight cap on the top of the submerged coring tube. We then carefully lifted the coring tube from the deposit so that a second tight cap could be placed on the bottom of the coring tube before the tube left the water. With both caps tightly placed, we removed the coring tube from the flume and placed it vertically in a holding container. This process was repeated for all of the coring tubes. After this was completed, the container containing the filled coring tubes was placed in a freezer to solidify the materials inside the tubes so that the cores could be later split.

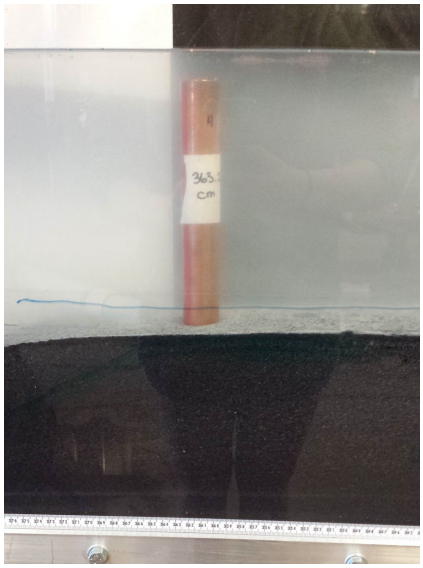

Figure 2.7.6: Example of a coring tube placed in the deposit and submerged in the pond before being carefully extracted.

Once the cores were completely frozen, we removed the core samples from the coring tubes and photographed them. We then divided each of the core samples into three approximately evenly sized smaller pieces to be photographed again with labels of the locations where they were extracted. We placed the separated core samples into sample bottles labeled with the coring location and the section of the deposit -- bottom, middle, or top. Some of the core samples contained much less material than the other samples and were therefore separated into fewer pieces. We include sample pictures taken of a coring sample before and after being divided into thirds in **Figure 2.7.7**. The core shown in **Figure 2.7.7** was extracted from experiment A03 at 330 cm from the start of the flume.

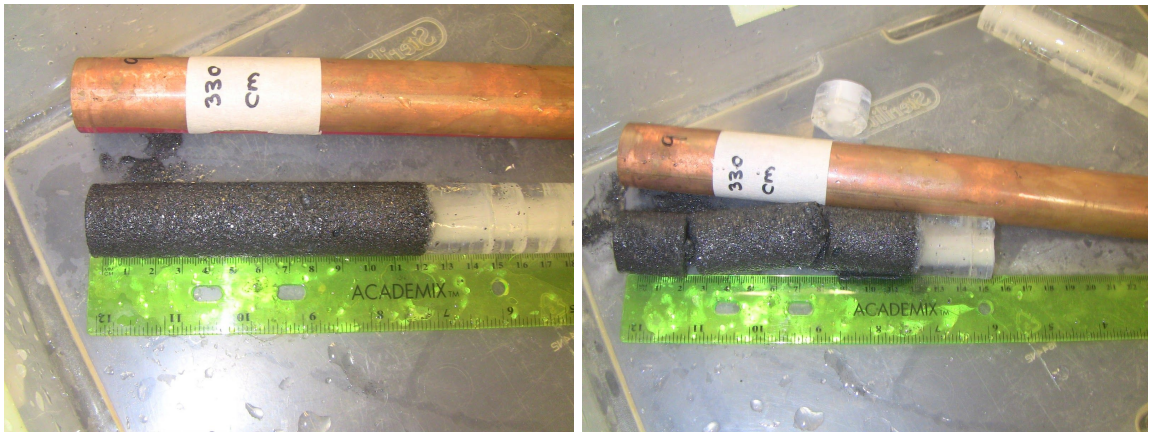

(a) **(b)**

Figure 2.7.7: Coring tube with core sample and a ruler with **(a)** exhibiting the core sample before it is broken up into three pieces and **(b)** displaying the core sample after it was split into thirds. This core sample was from experiment A03 and was extracted from 330 cm from the start of the flume.

Using the final deposit of A02, we developed a technique to determine new core locations scaled to those chosen for experiment A02 according to the locations of particular landmarks such as the edge of the topset and the edge of the bottomset. This way, core samples could be compared in a systematic manner. This is discussed further in section **3.4** and **4.4**. The locations of the core samples taken from the deposit formed during experiment A03 are recorded in **Table 2.7.2**.

A03 Coring Locations (cm)
91
227
295
330
363
382
396
431

499

Table 2.7.2: Table of coring locations from the deposit formed during experiment A03. The locations are in centimeters from the start of the flume.

2.8 Grain Size Analysis with Laser Diffraction

For the purpose of collecting the grain size distributions for various grain samples, we performed grain size analysis with laser diffraction using a highly-precise device called a Horiba LA-920, owned by the National Lacustrine Core Facility (LacCore) at the University of Minnesota. We include a photograph of the Horiba LA-920 located in the LacCore laboratory in **Figure 2.8.1**.

Figure 2.8.1: Photo taken of Horiba LA-920 located in the LacCore laboratory at the University of Minnesota.

2.8.1 Specifics of Horiba LA-920

The Horiba LA-920 uses a helium-neon laser with a frequency of 632.8 nm to produce diffraction patterns detectable by photodiodes. The device uses the length scales in the diffraction patterns to determine the grain sizes in a sample of particles. The Horiba

LA-920 is capable of differentiating sizes of particles with diameters ranging from 0.02 to 2000 microns.

Instruments such as the Horiba LA-920 that use light diffraction to determine grain sizes base their output on three major assumptions: (1) the light-scattering particles in a sample are spherical in shape, (2) there are no multiple scattering phenomena, and (3) the detector receives a scattering pattern that is the sum of the individual scattering patterns from each particle in the sample. Therefore, any divergence from a spherical shape may produce notable errors in the particle size distribution representation (A Guidebook to Particle Size Analysis, 2012).

2.8.2 Grain Size Analysis Procedure

After the Horiba was warmed up, we inserted a standard into the machine to ensure that the results given by the Horiba LA-920 were consistent and accurate. The standard was an Aluminum Oxide powder with a median grain size of approximately 62 microns. For the results given here, we only inserted a small amount of the standard as the Horiba did not need a large sample to produce a grain size distribution. We include a photo of the standard taken before inserting into the Horiba in **Figure 2.8.2**.

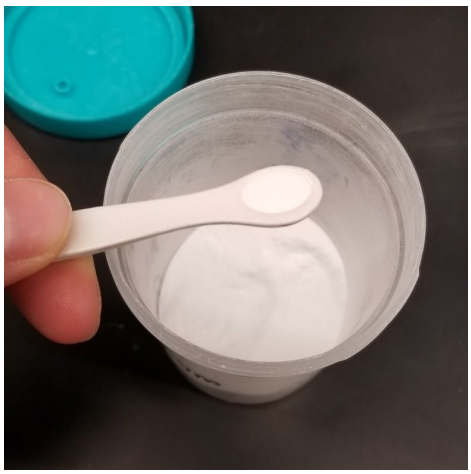

Figure 2.8.2: Picture of a scoop of Aluminum Oxide powder standard before it was inserted into the Horiba.

When the Horiba produced an acceptable result for the standard's median grain size, we could insert our experimental samples for testing. As is typical, our experimental samples were too large for a single analysis in the Horiba, so we needed to take a smaller subsample for analysis. Since our samples were composed of particles of many different sizes, we needed to ensure that there was no unmixing occurring in our samples before we took a subsample and placed it in the Horiba. We noticed that a major source of unmixing in our samples happened when our mixture sample was too wet. That is, when the sample was mixed, the large particles settled out quickly, leaving the fine particles in suspension. In this situation, it was difficult to take a scoop that accurately represented the entire sample. We found another source of unmixing to be grain-size segregation typical of dry particles (e.g., kinetic sieving) when our sample was dry. To avoid any sorting or separation from occurring, we found that slightly moistening the samples helped to keep the particles well-mixed and resulted in more consistent results. If samples were initially too wet after thawing, we dried them in an oven, and if the samples were too dry, we added drops of water to the sample bottle until we attained a desirable intermediate moisture level. Before we took a scoop for measuring, we mixed each sample thoroughly by hand, with care not to break down the grains of the samples. **Figure 2.8.3** displays a dampened sample being mixed before a scoop was extracted and placed in the Horiba. The sampling difficulties mentioned here are discussed further in section **5.2.3 Grain Size Analysis Sampling Complications**.

Figure 2.8.3: Picture of a sample after it had been moistened and mixed thoroughly. A dropper like the one next to the sample in the picture was used to add drops of water to the sample until it was sufficiently damp.

There were several variables that we could adjust when working with the Horiba LA-920. We found three to be noteworthy: (1) the circulation speed, (2) the Relative Refractive Index (RRI), and (3) number of subsamples per sample. The circulation speed setting pertains to the speed at which the sample was mixed after being inserted into the Horiba. After several tests, we found that the circulation speed did not noticeably affect our sample results and we chose a moderate circulation speed setting of 10. The Relative Refractive Index (RRI) setting pertains to the ratio of the speed of light of a specific medium to a given medium, or in this case, water. To determine the correct settings for our particles, we researched the index of refraction of the materials and entered these values into the machine. The Horiba also allowed the user to select the number of subsamples per sample submitted for analysis. This pertains to how many subsamples the Horiba would divide the initial subsample we placed in the machine into. Based on the advice we received from the Horiba technician Jessica Heck, we programmed the Horiba to divide our submitted samples into two subsamples.

Once our samples were at the correct dampness and well-mixed, small scoops were placed in the funnel of the Horiba, as we show in **Figure 2.8.4**.

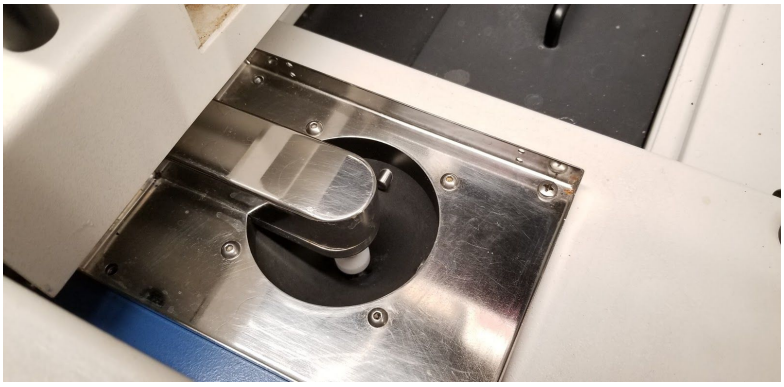

Figure 2.8.4: Photograph taken of the funnel located on the top of the Horiba where samples were inserted.

Once we input our sample into the Horiba, we needed to monitor a setting known as “Transmittance” (T%), presumably, the percentage of light signal that reached the other side of a sample. Initially, the T% was at 100% and as we released the sample into the machine by dropping it into the funnel, the T% dropped. Horiba technicians recommend the T% be between 95 and 70% for the best running conditions. If not enough material is inserted for good results, the T% is above 95%, and we would place more of the sample in the Horiba funnel. On the other hand, if the T% was too low, the material was too dense for good readings, and we added water to the funnel to correct for this.

Once the T% was within the recommended range, the Horiba began its analysis of the sample. When the Horiba finished, it returned a grain size distribution, as shown in **Figure 2.8.5**, for the number of subsamples selected and also displayed various grain size characteristics such as median, average, and mode grain sizes. The distribution shown in **Figure 2.8.5** was for a core sample taken from the middle layer of A02 at 270 cm from the start of the flume. Select grain size distributions are included in **Chapters 3** and **4**.

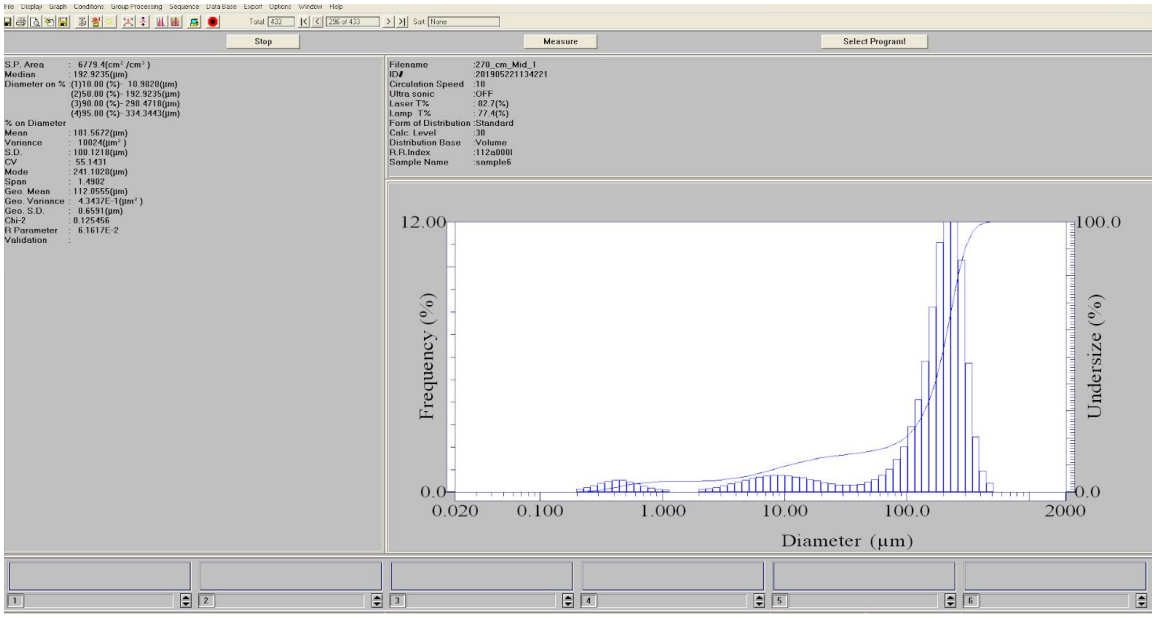

Figure 2.8.5: Screenshot taken of Horiba results for a core sample from A02 at x=270 cm in the middle section of the deposit. This screen displays the grain size distribution on the plot and various grain size characteristics in the top left corner.

Chapter 3 - Experiments with Coal and Clay Mixture

3.1 Description of Mixture

For the purpose of creating a surrogate mixture that behaved comparably to actual TSRU tailings, we conducted several experiments on TSRU tailings samples we had received and surrogate mixtures we composed. First, we estimated the volumetric concentrations of solids and process water in a 1.0 liter sample of TSRU tailings. We then observed the settling behavior of TSRU tailings to compare to other mixtures. The unique settling behaviors led us to test combinations of materials we had readily available at St. Anthony Falls Laboratory. After we found the surrogate mixture that best matched the TSRU tailings, we performed grain size analysis on the materials composing the surrogate mixture and took microscopic images in order to gather more information on the materials.

3.1.1 Determination of Surrogate Sediment Mixtures

Some of the physical properties of the TSRU tailings from the Material Safety Data Sheet (MSDS) are included in **Table 3.1.1** below.

Material Property	**Value**
Relative Density	1 - 1.5
Density (at 15.5 ºC)	900 kg/m^3 - 1200 kg/m^3
Viscosity	21 cSt (21 mm^2/s) at 40 ºC

Table 3.1.1: Table containing various data from the MSDS for TSRU tailings received from an oil sands company (Tailings Solvent Recovery Unit (TSRU) Tailings, 2016).

Since our goal was to create a surrogate that imitated the TSRU tailings well, we decided that our surrogate should have a similar solid fraction to that of the actual tailings. We determined the concentration by volume of a TSRU tailings sample that we had received from the field by placing it in a 1.0 L sealable glass settling column and allowing for the column to completely settle over the duration of several months. We then visually estimated the concentrations by volume of the solids and process water of the TSRU tailings sample and documented them in **Table 3.1.2**. We additionally calculated the concentrations by weight which we also included in **Table 3.1.2** using the void ratio provided to us.

Material	**Concentration by Volume**	**Concentration by Weight**
Solids	0.103	0.14
Process Water	0.897	0.86

Table 3.1.2: Table containing concentrations by volume of solids and process water for a sample of TSRU tailings.

We include the actual amounts of coal and clay used in experiments A02 and A03 in **Table 2.5.2**.

To characterize the settling behavior of the TSRU tailings, which we hypothesized would play an important role in the settling pond behavior, we performed a series of tests in a settling column. Upon simple observations, it was relatively straightforward to see the components of the tailings settled primarily at two distinct rates and formed two definitive layers as seen in **Figure 3.1.1 (a)**. The surfaces of the two layers are indicated by the white and black lines in **Figure 3.1.1 (b)**.

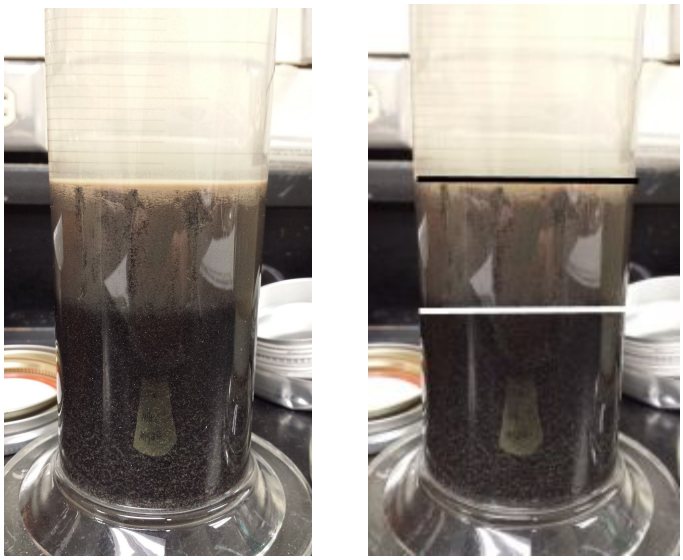

(a) **(b)**

Figure 3.1.1: (a) Photograph taken of TSRU tailings in a settling column after being left undisturbed for several days. The tailings formed two distinct sediment layers: one of dark colored, large particles that settled within a few minutes and one of lighter colored, fine particles that took several days to completely settle out. **(b)** The surface of the first layer is indicated by the white line and the surface of the second layer is indicated by a black line.

We denote the layer below the white line in **Figure 3.1.1 (b)** as the bottom layer and note that it consists primarily of larger particles that settled out swiftly after being mixed. We also noticed that the large particles in this layer captured some of the smaller, lighter colored particles while settling. We note that there is a color gradation in the bottom, dark layer of the settling column, evidence of a differential capture rate from top to bottom. The gradual change in color visible in these macroscopic pictures is reflective of the small particle concentration gradient visible by eye, indicating a higher concentration of smaller particles captured near the bottom of the large particle layer.

Once the interface became visible, we noticed more fine particles falling out of suspension and forming the second, lighter colored layer whose surface we indicate with a black line in **Figure 3.1.1 (b)**. For this process to reach a near final state where the third layer of liquid had clarified, we needed to leave the settling column undisturbed for several days.

We wanted to create a surrogate mixture with similar settling behaviors to the TSRU tailings discussed above. To minimize cost, we looked for such materials leftover from previous experiments in sufficiently large quantities at the St. Anthony Falls Laboratory. The materials that we tested included fine-grained ballotini, fine grained sand, nepheline syenite, anthracite coal, and kaolinite clay. Some of these materials were fine grained to simulate the fines that took some time to settle and some of these materials were large grained to simulate the large particles that settled out quickly. We include a picture of some of the mixtures that we tested sitting next to TSRU tailings in a settling column in **Figure 3.1.2**.

Figure 3.1.2: Picture of different mixtures tested in glass jars sitting next to a TSRU tailings sample in a settling column. Here, we wanted to see if these mixtures would form two distinct sediment layers like TSRU tailings and at similar settling rates.

A table of the mixtures we tested are included in **Table 3.1.3**.

Mixture #	Surrogate Fines	% by Volume	Surrogate Coarse	% by Volume
1	Fine Ballotini	75	Lakeland Sand	25
2	Nepheline	50	Anthracite Coal	50
3	Fine Ballotini	50	Anthracite Coal	50
4	Kaolinite Clay	10	Anthracite Coal	90

Table 3.1.3: Table of surrogate mixtures whose settling behaviors were tested and compared to those of the TSRU tailings sample. We note that the % by volume indicates the % by volume of solid particles. In all cases we tested these with 95% water by volume.

3.1.2 Time Dependent Pictures and Observations

In the end, we found mixture four in **Table 3.1.3**, a mix of 90% anthracite coal and 10% kaolinite clay sediment by volume, mixed in a 1:19 volumetric ratio with water, to exhibit the most similar settling behavior to the actual TSRU tailings and chose this mix to be our primary surrogate mixture.

We performed settling column experiments to determine whether or not our surrogate mixture described in the previous section settled and behaved similarly to the TSRU tailings sample in a quiescent fluid. To complete this, we filled a 1.0 L settling column with the coal, clay, and water components of our surrogate mixture. We also filled a 1.0 L settling column with a TSRU tailings sample to compare to the surrogate mixture. The top of the settling columns were both sealed so that the columns could be inverted, allowing for the materials to mix. Once the columns were sufficiently mixed, we placed them side-by-side in front of a video camera. The surfaces of the initially settled layer of the surrogate mixture and TSRU tailings sample were tracked in the videos as indicated in **Figure 3.1.3**.

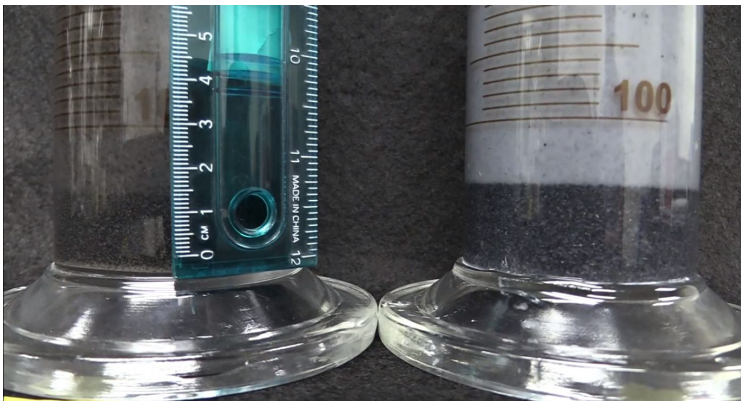

(a)

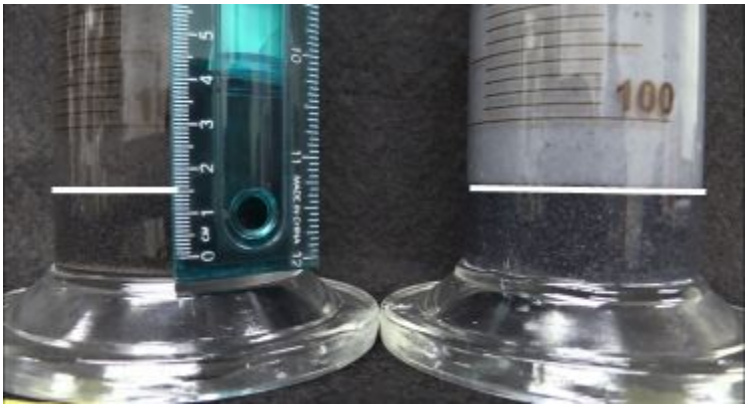

(b)

Figure 3.1.3: (a) Snapshot of video that captured the settling of the TSRU tailings (left) and the coal, clay, and water mixture (right) in 1.0 L settling columns. **(b)** The same image but with white lines to indicate the surface of the initially settled layer that was tracked. A ruler was taped to the side of the tailings settling column in order to provide a scale.

The time for the settling experiments started (t=0 s) as soon as the columns were simultaneously placed in front of the video camera. At various times, the height of the settled layer surface for both samples was recorded. The data collected from three such TSRU experiments and four such surrogate mixture experiments is documented in **Figure 3.1.4**.

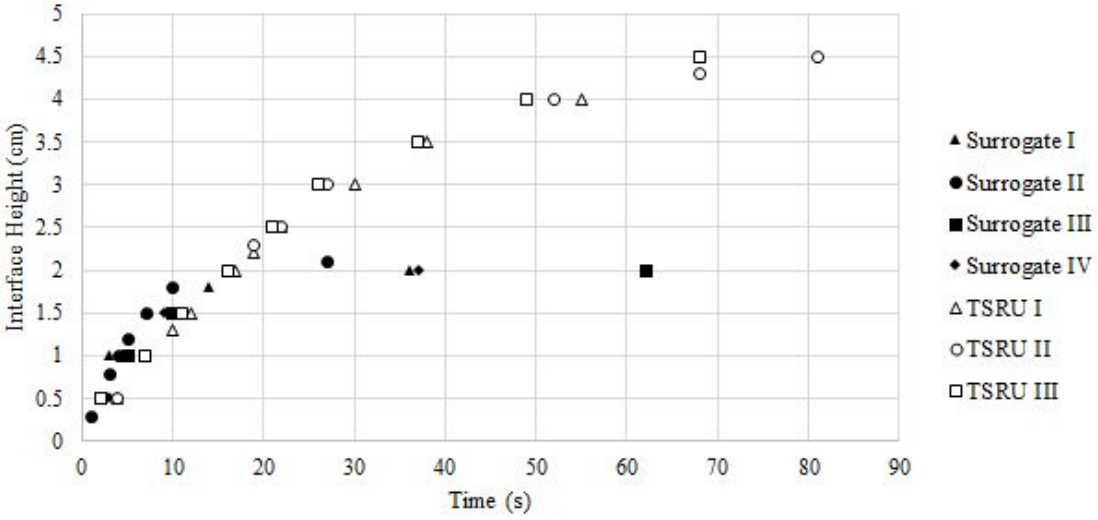

Figure 3.1.4: Plot of elevation of initially settled sediment layer for the TSRU tailings sample and our coal and clay surrogate mixture. There were four videos of the surrogate mixture settling and three for the TSRU tailings sample.

By performing a numerical derivative on the interface location data, we calculated an effective settling rate for the surrogate mixture and the TSRU tailings sample that could be quantitatively compared with other mixtures. We present these data in **Figure 3.1.5**.

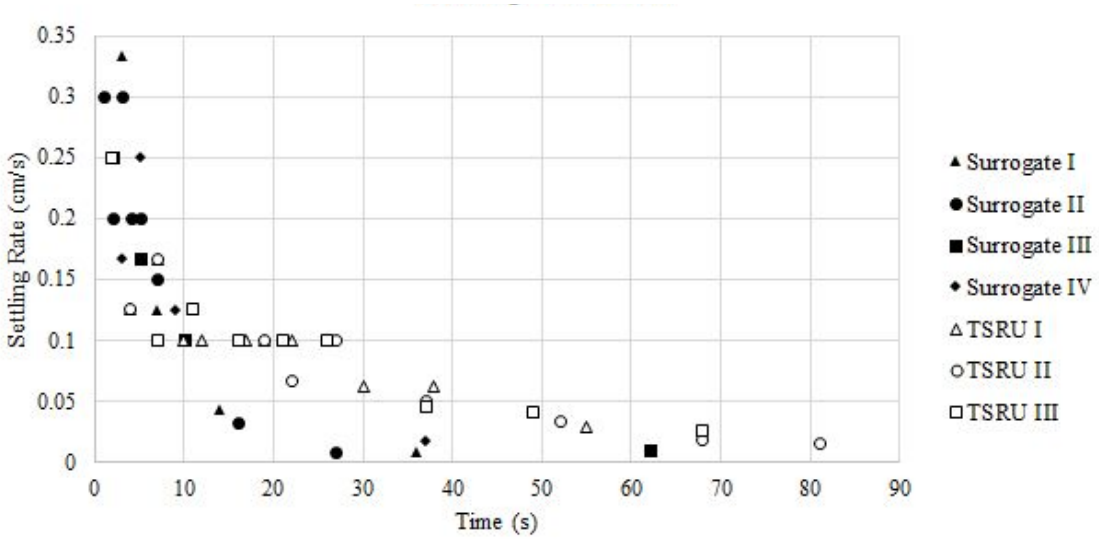

Figure 3.1.5: Graph of calculated settling velocities of the interfaces of our surrogate mixture and the TSRU tailings sample. There were four videos of the surrogate mixture and three videos of the TSRU tailings sample settling.

Over the same amount of time, the settling velocities for the TSRU tailings sample ranged between 0.015 and 0.25 cm/s and 0.01 and 0.33 cm/s for the surrogate sample. While there were many similarities, we note there were some differences. In particular, after approximately 15 minutes, the surrogate sample appeared to reach a steady state while the TSRU tailings continued settling. While this difference seems substantial, this coal and clay surrogate mixture seemed to behave the closest to TSRU tailings and we continued with this for our most prominent surrogate runs.

3.1.3 Laser Diffraction and Microscope Results

While we had basic information about the grain size distributions of the particles in our surrogate mixtures, we felt it was important to know these even more precisely. Therefore, we performed laser diffraction grain size analysis on separate samples of anthracite coal and kaolinite clay. A more detailed description of the grain size analysis can be found in **2.8.2 Grain Size Analysis Procedure**. For each region of each core, we input two unique subsamples into the Horiba. We chose a setting on the Horiba that had it further divide each of these two samples into four subsamples for a total of eight subsamples for each region of each core. While typically, the total average of all such samples are presented, it is helpful to examine each individually to understand certain trends. For example, the first of the samples often exhibit the largest sizes of the grouping because of the spontaneous segregation we spoke about in **Chapter 2**.

In **Figure 3.1.6**, we present the relative frequencies for each of the subsample tests as well as the average considering all of the subsamples to give us the average relative grain size frequency of the anthracite coal. We include these plots in **Figures 3.1.6** and **3.1.7** for anthracite coal. In **Figure 3.1.7** we present the same information for kaolinite clay. We discuss in more detail our reason for calculating the average relative frequency in section **3.5.1** and **4.5.1**.

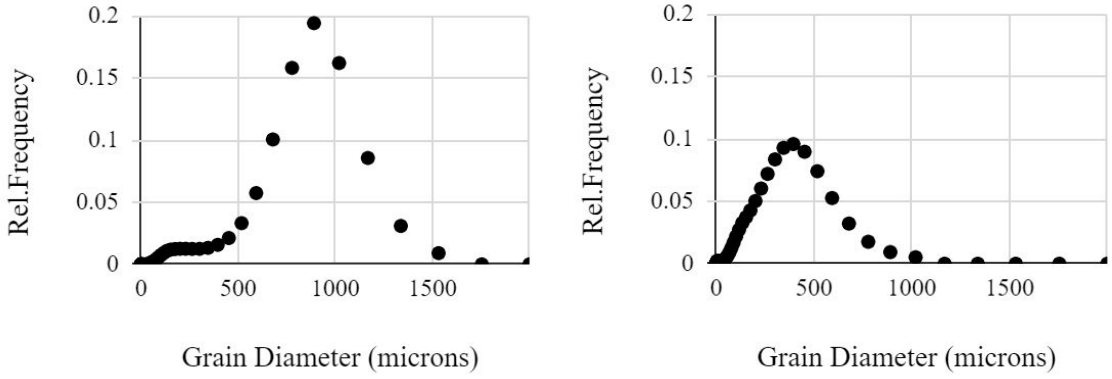

(a) **(b)**

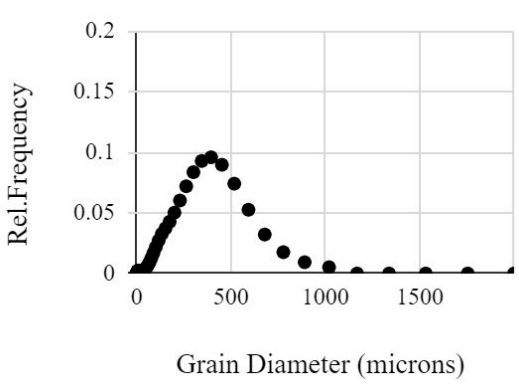

(c)

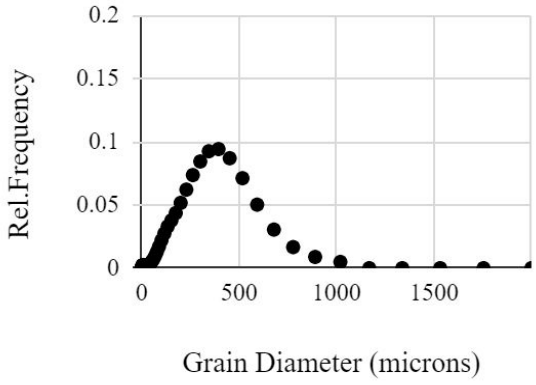

(d)

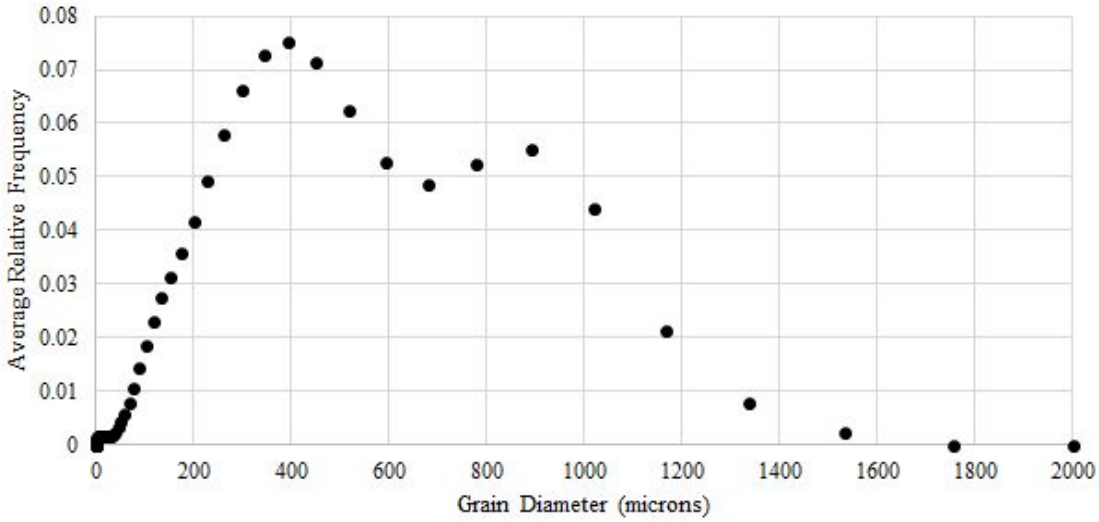

(e)

Figure 3.1.6: **(a)-(d)** The four individual relative frequency plots received from performing grain size analysis on anthracite coal. **(e)** The average relative frequency plot for anthracite coal.

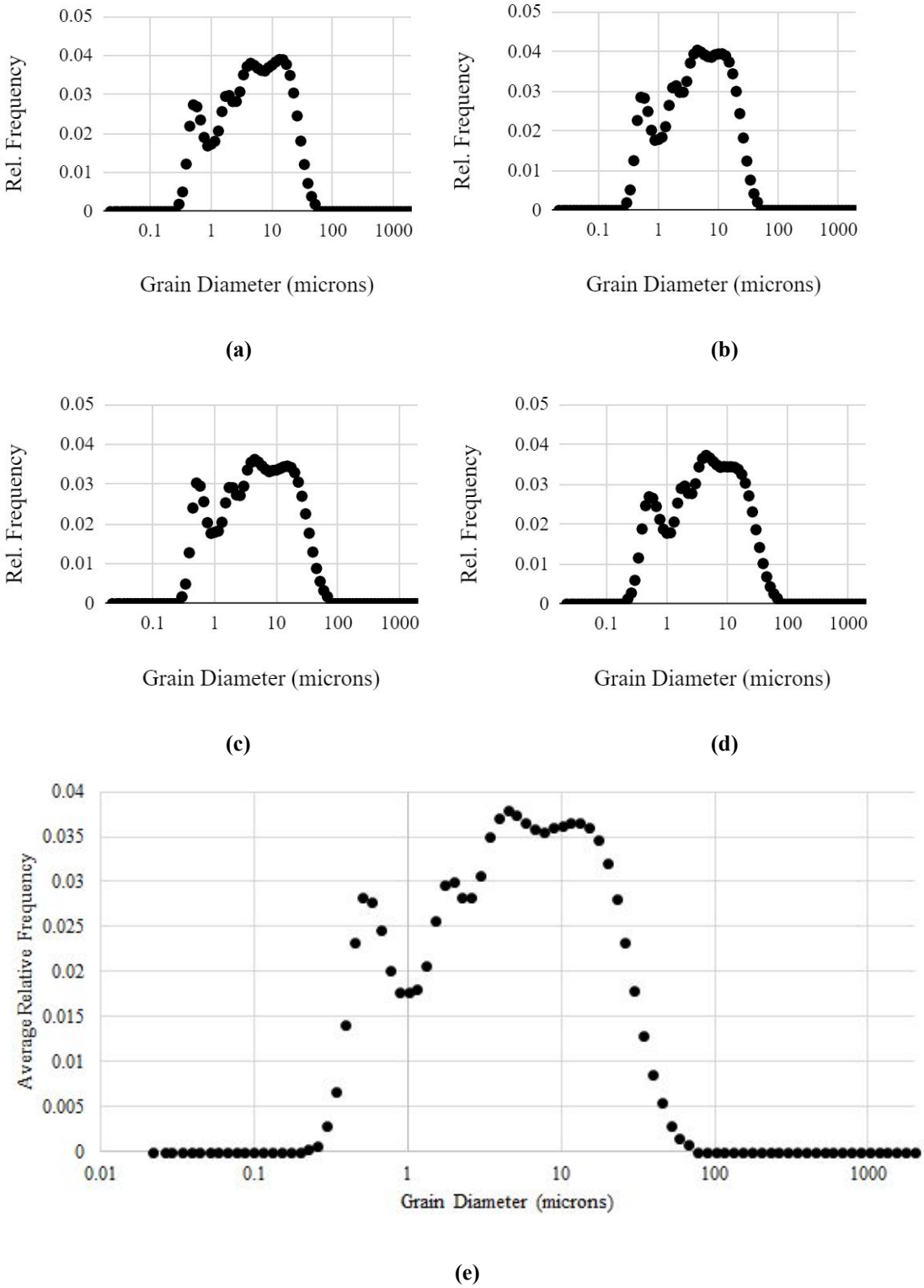

Figure 3.1.7: (a)-(d) The relative frequency plots for the four kaolinite clay samples on a log scale. **(e)** The average of the four relative frequency plots of kaolinite clay on a log scale.

The average relative frequency plot for coal had two peaks, one located at roughly 400 microns and one around 900 microns. For clay, there appear to be several peaks that are essentially the same for each subsample that thus appear in the average relative frequency plot; we consider these as one broader peak close to 4 microns.

Figure 3.1.8 includes microscope images of dry coal and clay samples. The photos in **Figure 3.1.8** were taken with a Leica Wild M10 microscope. The bar in the top left corner of the images provides a scale of 2 mm.

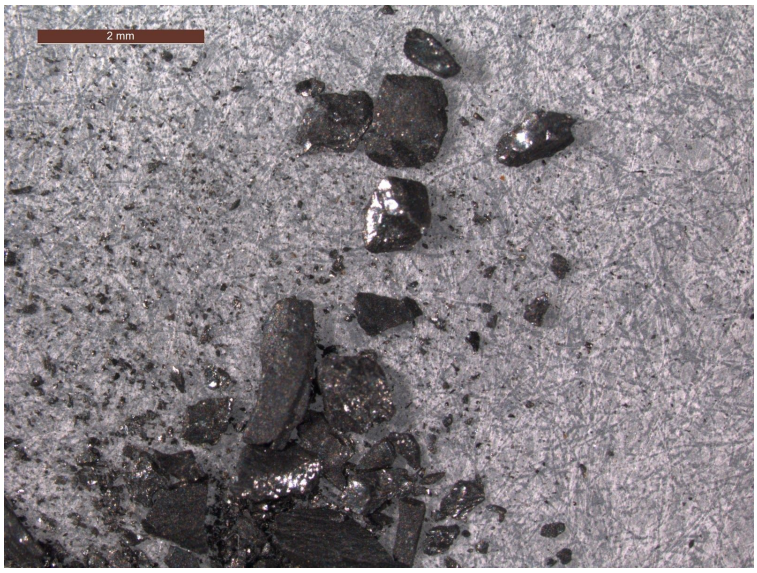

(a)

(b)

Figure 3.1.8: Microscope images of **(a)** anthracite coal and **(b)** kaolinite clay. The photos were taken with a Leica Wild M10 microscope. The bar in the top left corner of the images provides a scale of 2 mm.

In **Figure 3.1.8 (a)**, it is easy to understand why we see two peaks in the grain size distribution of coal. The image also exhibits the angularity of the coal particles that has the potential to reduce the accuracy of the grain size analysis given that the process assumes a spherical shape of all particles. The clay particles shown in **Figure 3.1.8 (b)** are very small and likely to clump together. While it is difficult to determine from this image alone that there is a relatively singular grain size for these particles, one might get some intuition to this effect from the photograph.

3.2 Observations of Experimental Depositional Formation

As we described and documented in section **2.2**, TSRU tailings are delivered to the tailings ponds at variable discharge rates. In order to see if changing the discharge rate had a noticeable effect on the segregation, transportation, and deposition of actual tailings, for the two experiments with the coal and clay surrogate mixtures, we used two different inflow rates. Altering the inflow rate is a relatively attainable adjustment that can be made by the oil sands producers. We based our discharge rates on our calculations in section **2.2**, similar to those we presented in **Table 2.2.2**. Given the range of flow rates calculated in the table, we decided on a flow rate of 0.5 L/s for what we called experiment A02 and a rate of 1.0 L/s for experiment A03.

The deposits formed during experiments A02 and A03 had three basic formation stages: the initial stages when the deposit begins to form, the “steady state” stage when the front does not change in shape but merely travels downstream, and the “no flow” stage when the pumping was ceased and suspended particles were allowed to settle. We present our observations for these three phases in each of the following subsections.

3.2.1 Early Stages

In the early stages of our experiments, the mixture passed over the upstream weir, and traveled first as a plume downstream before it appeared more thoroughly mixed with the pond water. This flow is similar to hypopycnal flow, as mentioned in **Chapter 1**. A snapshot of the plume seen in experimental run A03 is included in **Figure 3.2.1** below. The plume shown in **Figure 3.2.1** traveled downstream or from the right side of the image to the left side.

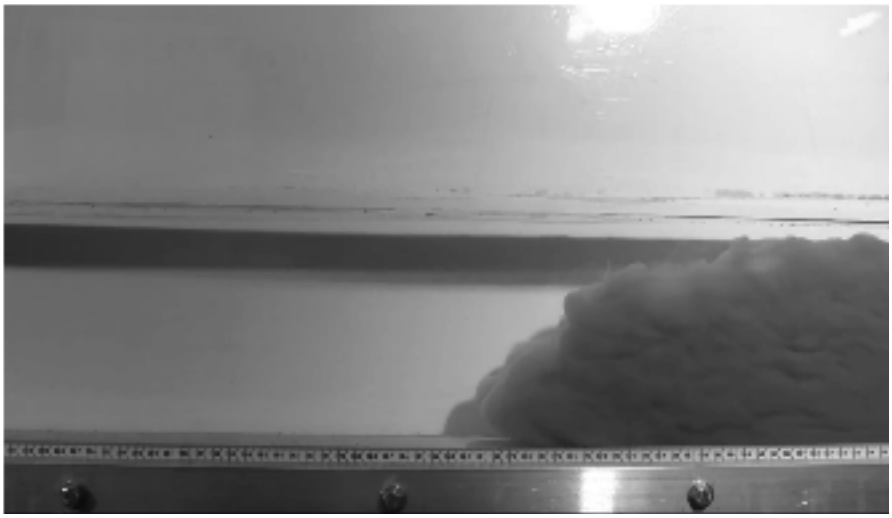

Figure 3.2.1: Snapshot taken from video recording of experiment A02 around 200 cm from the start of the flume. The plume traveled from right to left, leaving behind a cloud of material.

After the plume initially travelled the length of the flume, it left behind a thin layer of sediment at the bottom of the flume as we show in **Figure 3.2.2**. This photo was taken during experiment A03 where the largest particles left suspended by the plume were able to settle at the bottom of the flume.

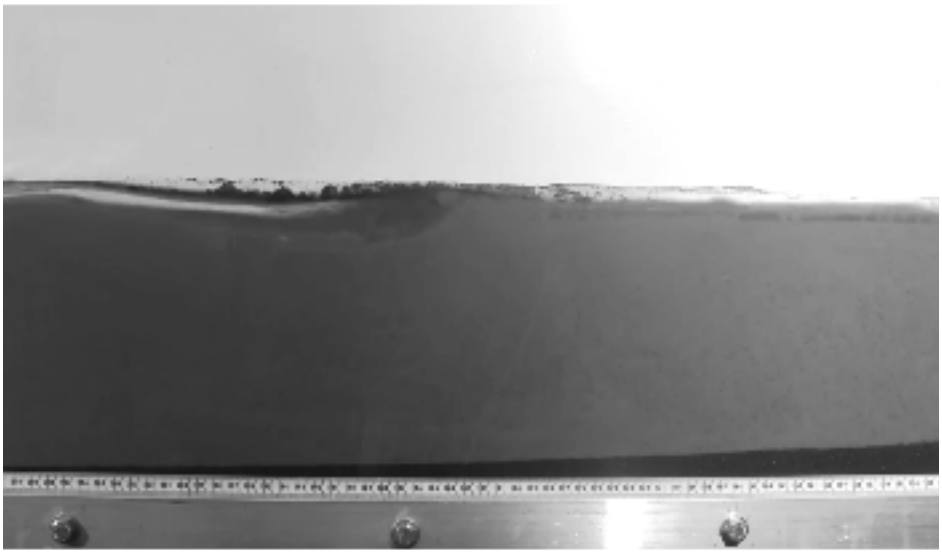

Figure 3.2.2: Screenshot from a video from experiment A03 after the plume passed through this length of the flume. The large particles carried by the plume are allowed to gradually settle and form the bottom layer of the deposit.

At the same time the plume traveled the length of the flume, a triangular-wedge slowly formed on the downstream side of the upstream weir as the large particles initially settled near the intake. The wedge grew in a triangular shape at these early times until it reached the water surface. Once the top of the initial wedge reached the water surface of the pond, a Gilbert-style delta began to take shape. A snapshot of the prograding delta from run A03 at early times can be seen in **Figure 3.2.3**.

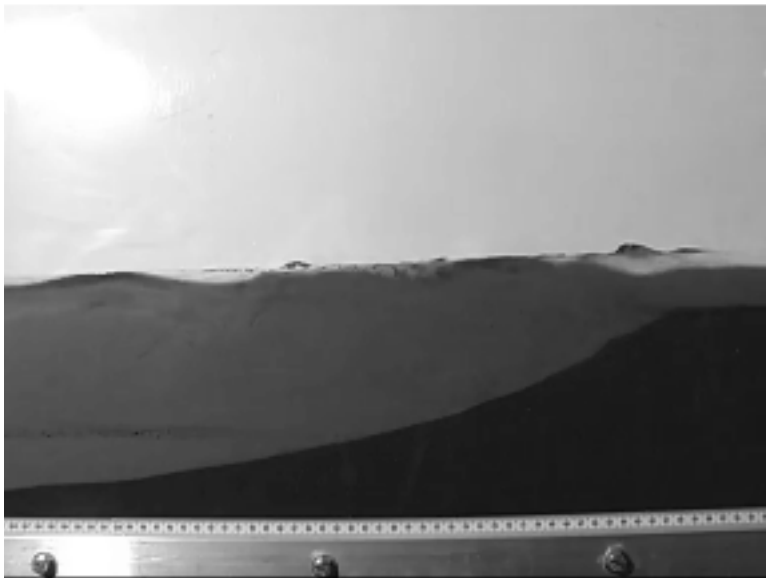

Figure 3.2.3: Snapshot from video from run A03 showing the deposit traveling from right to left in the experimental flume.

After the Gilbert delta finished its initial stages of formation, the materials delivered to the flume were transported over the topset surface with great speed. A small fraction of these particles settled on the growing surface of the delta which we call the beach above water or the topset. The majority of the particles moved as a stream, skimming the top surface and occasionally moving the top particles of the deposit as bedload along the topset. Once the sediment reached the edge of the topset, the flow detached from the sediment surface; some of the remaining large particles deposited at the upper portion of the foreset while the remaining gave rise to a complicated series of eddies. The foreset periodically steepened and intermittently failed and avalanched down the foreset in hyperpycnal flow. This action covered the previously settled materials of the bottomset closest to the foreset with a new layer of sediment.

The particles not deposited at the upper edge of the topset traveled in homopycnal flow past the front of the deposit to settle farther downstream. A continuation of these events steadily added to the downstream progression of the front of the deposit. As the deposit continued to advance downstream, the edge between the bottomset and the foreset became more clear and distinguishable.

3.2.2 Steady State

Several minutes into the experiment, the front of the deposit did not vary considerably in shape, but simply prograded downstream. Two images displaying the front of the deposit from experiment A02 in this stage at two different times are included in **Figure 3.2.4**.

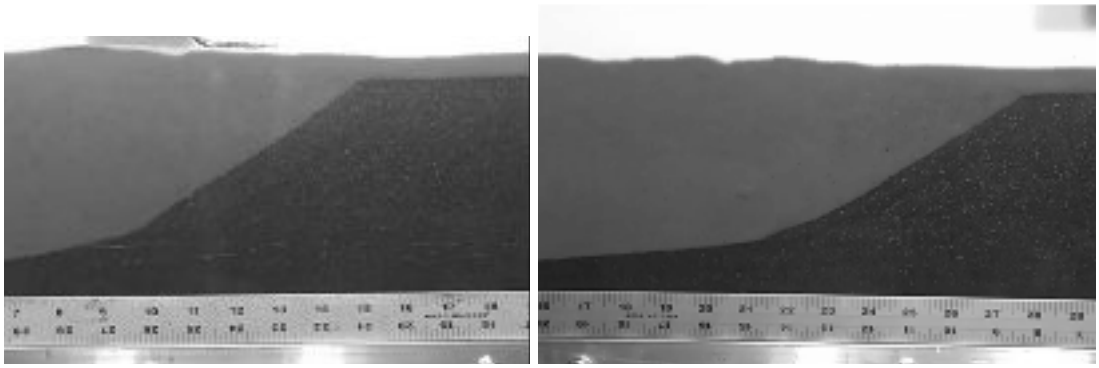

(a) **(b)**

Figure 3.2.4: Video screenshots from experiment A02 of deposit in steady state with **(a)** taken at an upstream location and **(b)** taken at a downstream location. The shape of the front of the deposit did not change considerably in shape as it progressed upstream to downstream.

During this phase, the front of the deposit continued prograde through a build-up or avalanche process while the topset and bottomset aggraded at much slower rates. We also observed that the angle of the foreset did not vary considerably over the duration of a run.

3.2.3 After Pumping Ceased

The experiment was stopped when the level inside of the mixing tank was too low for the mixer to work effectively. With no new material being added to the flume, the third and final phase of the experiment began with the slow settling of suspended

materials. As the suspended particles in the pond gradually settled they formed a thin layer over the ponded portion of the deposit. A photograph describing this formation can be seen in **Figure 3.2.5**. The parts of the deposit with more pond water above it had a thicker layer of settled out materials.

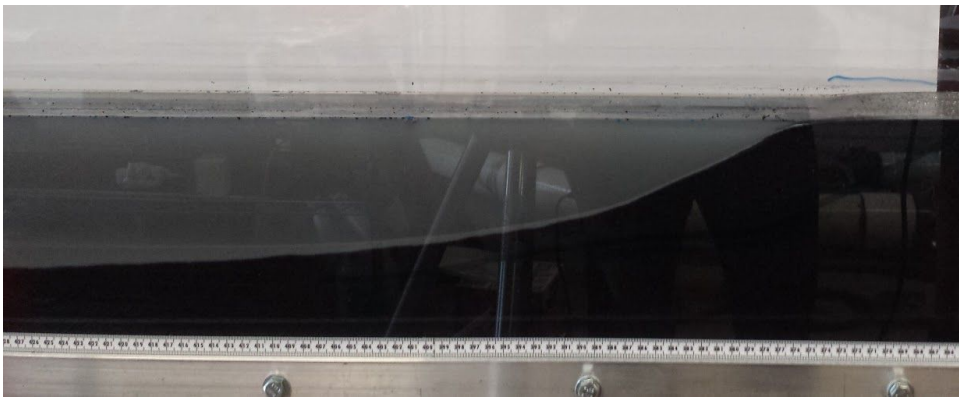

Figure 3.2.5: Picture of pond settling out and forming a thin layer of fine particles for experiment A03.

3.3 Measurements of Profiles

Some information about the progression of the deposit can be learned from recording the profile of the bed, determining bed slopes, and documenting the final deposit. Comparing the rate of progression and deposit characteristics can lead to interesting connections between different experiments. In this section we introduce data relating to deposit profiles slopes in **3.3.1** and **3.3.2** and further present a more comprehensive analysis and discussion on this information in section **3.6** for experiments A02 and A03.

3.3.1 Plots of Profiles

At designated times during an experiment, we marked the instantaneous position of the deposit by drawing on the sidewall of the flume as described in **2.7.2 Surface Lines**. After the completion of the experiment, we recorded the heights of those lines by

placing a ruler on the side of the flume. Examples of this data for experiments A02 and A03 can be seen in **Figure 3.3.1**.

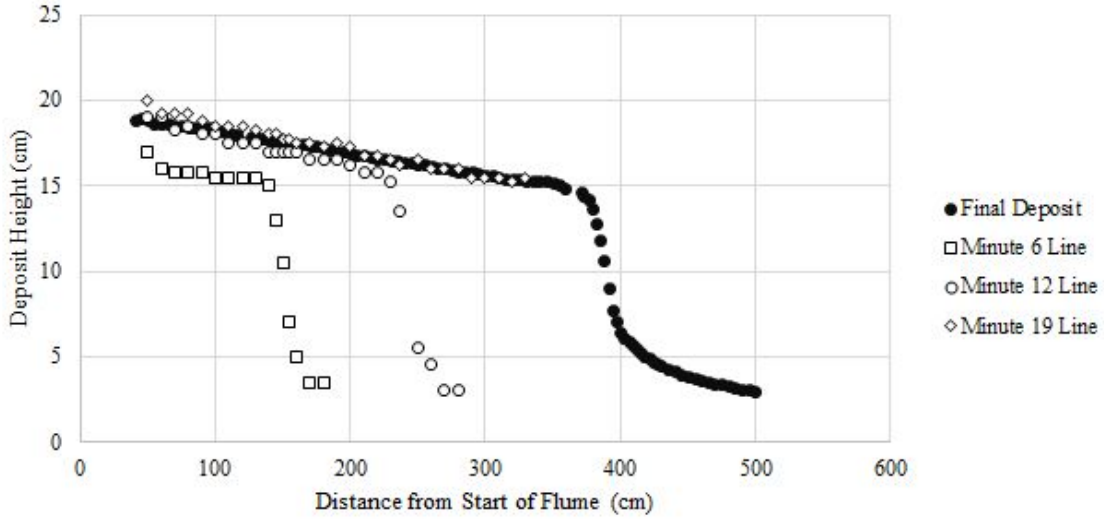

(a)

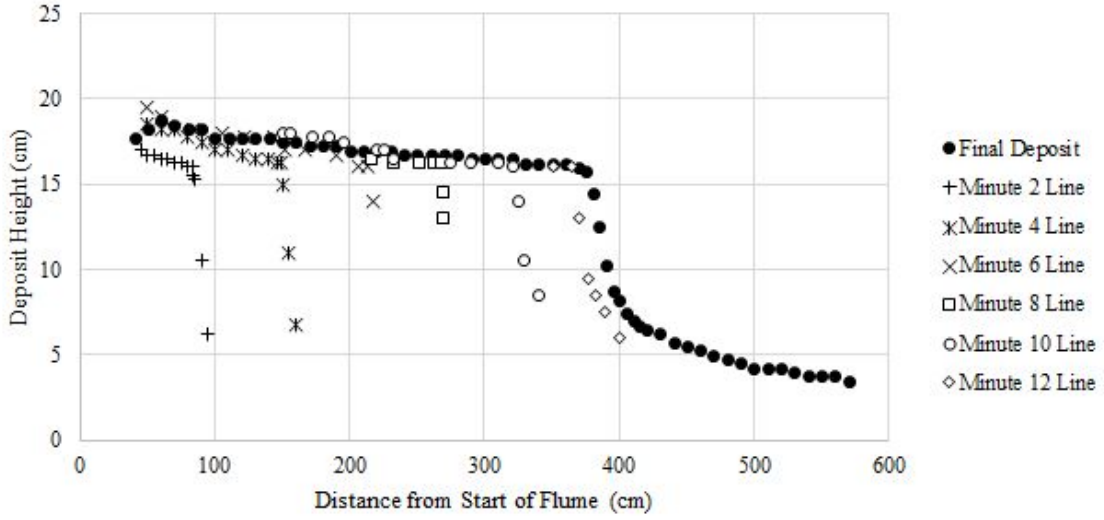

(b)

Figure 3.3.1: Recorded deposit heights or bed surface profiles from experiments **(a)** A02 and **(b)** A03 at various times throughout the each experiment as well as the final deposit. Some of the bed surface profile data for A02 and A03 is incomplete due to the front progressing too far before the lines were finished. Anticipating future discussion starting in section **3.6.1**, we here define the topset and foreset aggradation rates and velocities. The aggradation rates for both the topset and foreset refer to the change in area beneath

each surface divided by the time between two profiles. The topset and foreset velocities refer to the distance between two profiles divided by the time passing between the two measurements.

The plots in **Figure 3.3.1** show that the deposit gradually aggraded in the horizontal and vertical directions as more of the mixture was introduced to the flume. It is notable that the movement that occurred in the horizontal direction on the foreset far surpassed the progression that took place in the vertical direction at the topset. This specific evolution of the deposit is further examined in the discussion in section **3.6.1**.

3.3.2 Final Topset, Foreset, and Bottomset Slope Values

The final deposits for A02 and A03 can be seen in **Figure 3.3.2**. The final deposit heights were recorded with a point gauge as mentioned in section **2.7.4 Final Surface Measurements**.

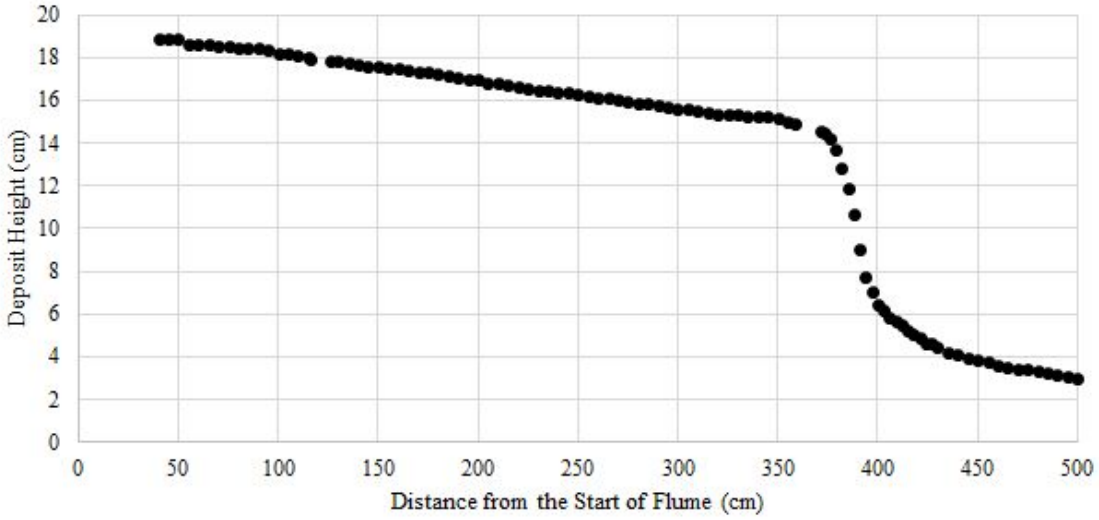

(a)

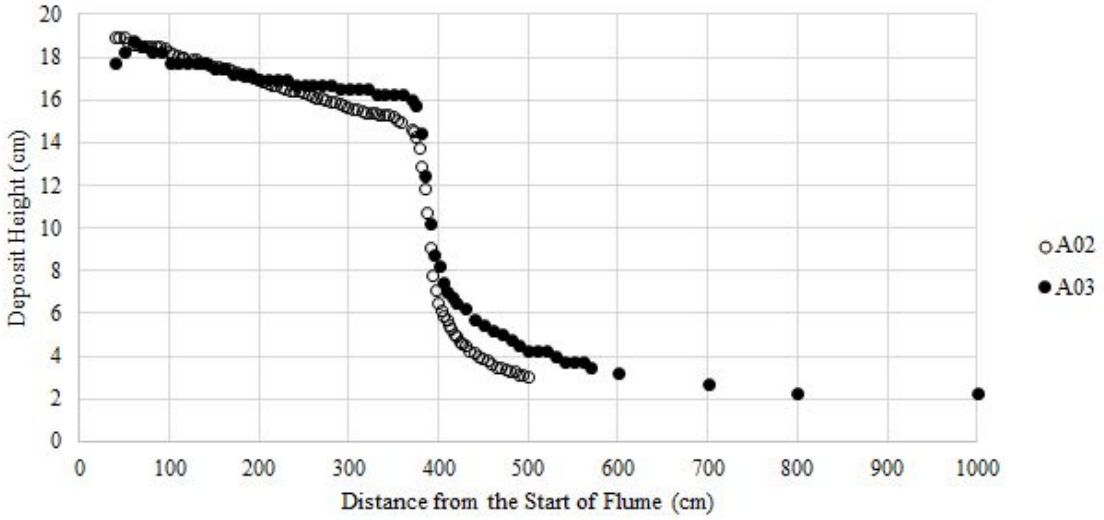

(b)

Figure 3.3.2: Final deposit heights for **(a)** A02 and **(b)** A02 and A03 as measured by a point gauge from the top of the flume. There are occasional gaps in the data due to the point gauge not being able to take data at locations where there were vertical aluminum supports.

To determine the slope values of the topset, foreset, and bottomset of each final deposit, we disregarded areas where the deposit height varied the most i.e. close to the inlet and near the transitions between sections. For example, the areas included in the determination of the topset, foreset, and bottomset slopes for A02 can be seen in **Figure 3.3.3**.

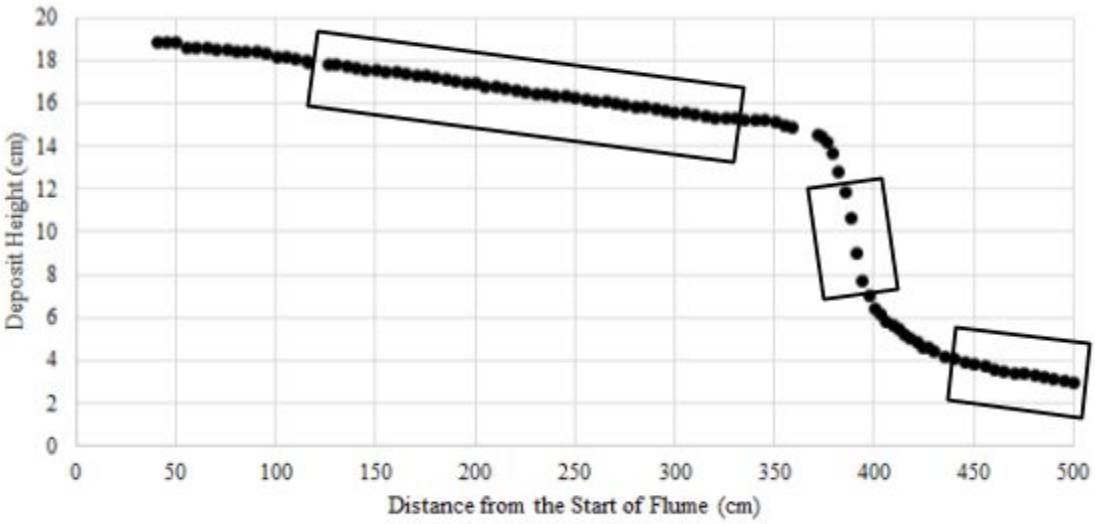

Figure 3.3.3: Final deposit from A02 with boxes to indicate where the slopes of the topset, foreset, and bottomset were taken. These boxes exclude the areas with a lot of variations such as near the inlet or near transitions.

We determined the slope values by fitting the data points within each range to a linear fit. The slope values for the topset, foreset, and bottomset of the deposits A02 and A03 are included in **Table 3.3.1**.

Experiment #	Discharge (L/s)	Topset Final Slope	Foreset Final Slope	Bottomset Final Slope
A02	0.5	-0.0129	-0.462	-0.014
A03	1.0	-0.0075	-0.325	-0.014

Table 3.3.1: Table with final slope values for the topset, foreset, and bottomset of experiments A02 and A03 as well as discharge rates.

As we can see from **Table 3.3.1**, the final topset slope for A02 is nearly double the slope value for A03. We also observe from the data that the final slope values for the foresets of each experiment are relatively similar with the slope for A02 being slightly steeper than the slope for A03. Finally, we note that both experiments A02 resulted in the

same final bottomset slope values. A more thorough discussion concerning the final slope values for the anthracite coal and kaolinite clay experiments is included in **3.6.2**.

3.4 Locations of Cores

As previously mentioned in **2.7.5 Coring Process**, we performed coring at nine different locations throughout the length of the flume in the interest of studying the various vertical layers within the experimental deposits. The core locations for A02 were chosen at approximately 100 cm intervals with exceptions near the foreset. More core samples were taken near the foreset in order to learn more about the segregation occurring in this transition region. We also did not want to capture any of the inlet conditions in our cores so we chose our first core location to be at 70 cm from the start of the flume.

We wanted to make sure that future deposits were cored in a similar fashion to A02 for later comparison, with no samples taken too close to the inlet, and more samples taken near the foreset region. To accomplish this, we identified the locations of the topset edge and the bottomset edge as displayed in **Figure 3.4.1**.

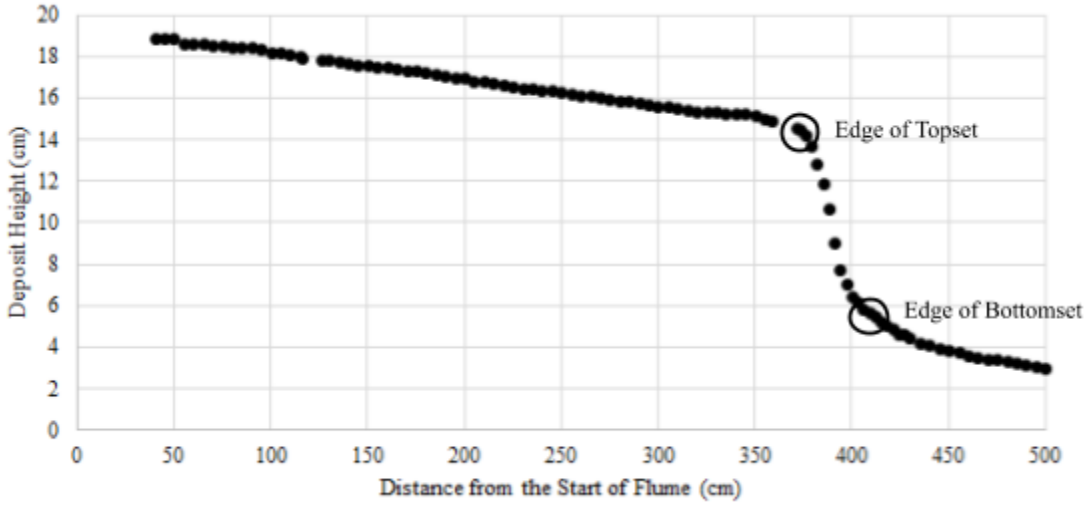

Figure 3.4.1: Plot of final deposit from A02 with circles indicating the locations of the edge of the topset and edge of the bottomset.

We determined the edges of the topset and bottomset by plotting the slopes for the topset, foreset, and bottomset and finding where these lines intersected. We used the distances between the edge of the topset and the edge of the bottomset for both A02 and A03 to determine the scale between the two deposits. This technique was then used to find the new coring locations for A03. The coring locations for experiments A02 and A03 are included in **Table 3.4.1**.

A02 Coring Locations (cm)	A03 Coring Locations (cm)
70	91
170	227
270	295
320	330
370	363
384	382
394	396
420	431
470	499

Table 3.4.1: Table of coring locations for the deposits formed during experiments A02 and A03. The locations are in cm from the start of the flume.

A diagram displaying the final deposit for study A02 with the coring locations is visible in **Figure 3.4.2** and in **Figure 3.4.3** for A03.

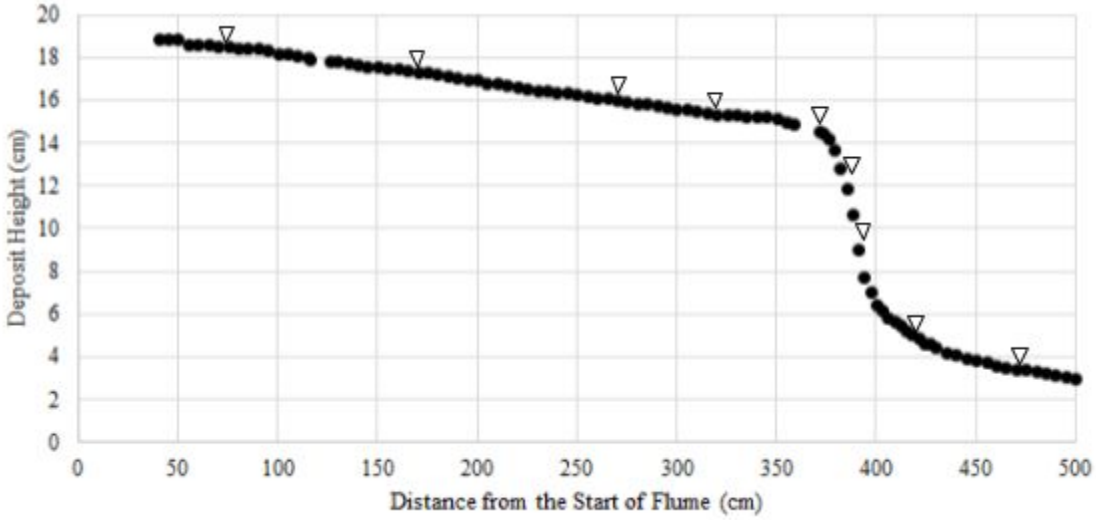

Figure 3.4.2: The final deposit for A02 with triangles indicating the locations where cores were extracted.

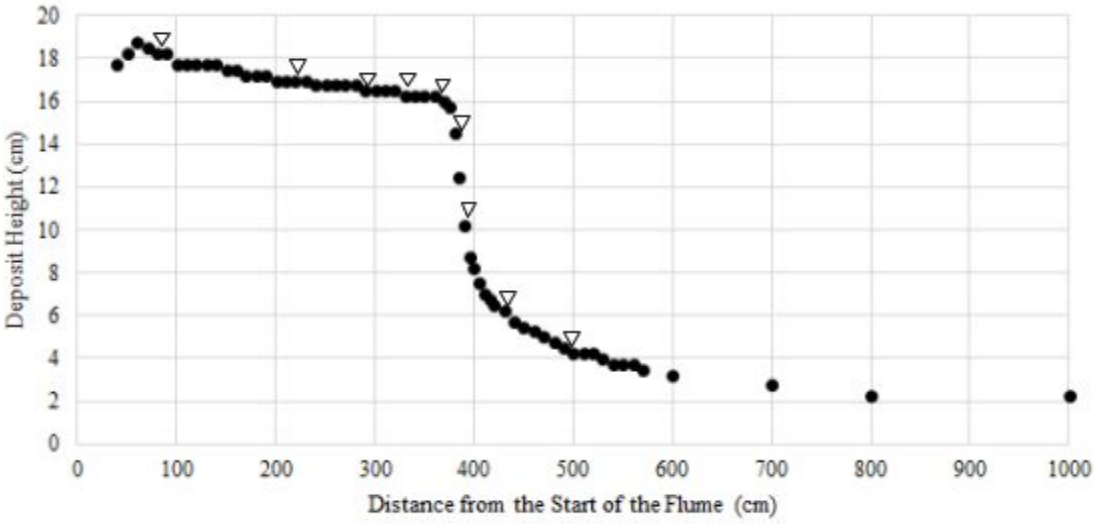

Figure 3.4.3: The final deposit for A03 with triangles indicating the locations where cores were extracted.

3.5 Presentation of Grain Size Analysis Results for A02 and A03

Originally, we considered examining the variability in the vertical sections of the deposit by considering the averaged median grain size for all of the distributions received for each coring location. We present the averaged median values for the different vertical

sections of the deposits for A02 and A03 in **Figure 3.5.1**. Along with the median values, we also plot the representative uncertainties of the median values. For clarity reasons, we only include half of the relative uncertainty values. We derived these uncertainty values from averaging all of the standard deviations from each of the subsample distributions received from the Horiba when conducting the grain size analysis. This was done for the top, middle, and bottom samples taken from every coring location for each experiment.

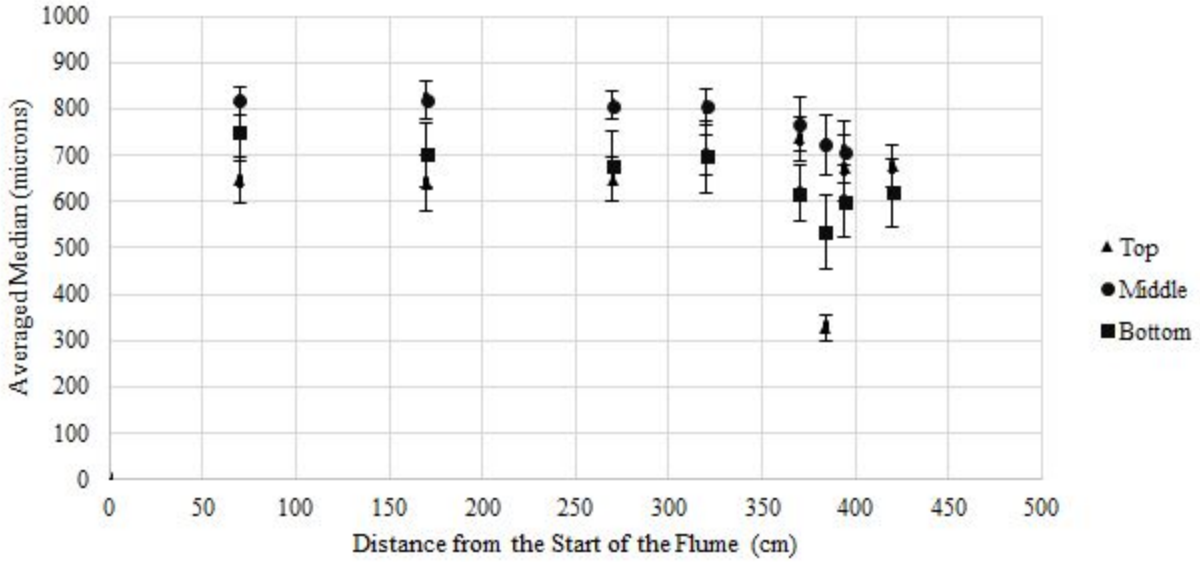

(a)

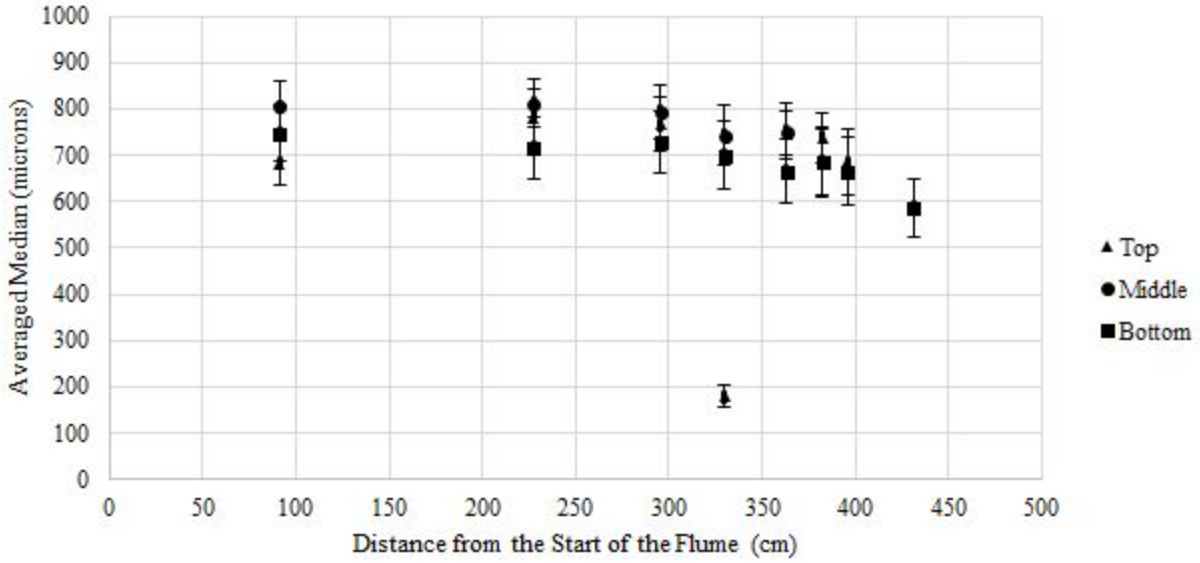

(b)

Figure 3.5.1: Averaged median grain sizes with representative error bars of the top, middle, and bottom sections for experiments **(a)** A02 and **(b)** A03 at varying distances from the start of the flume. The averaged medians were calculated by averaging all of the distributions collected for each subsample at each coring location and each deposit layer for both experiments. We derived the uncertainty values from averaging all of the standard deviations from all of the subsample distributions received from the Horiba. This was done for the top, middle, and bottom samples taken from every coring location for each experiment. For clarity reasons, we have plotted half of the representative error bars due to overlapping.

A noticeable trend in these plots is the gradual decrease in the averaged median grain size with distance from the start of the flume. By looking at **Figure 3.5.1**, we can also see that the middle section had the coarsest grain size out of all of the sections.

We realized that not all of the depositional dynamics contained in the grain size distributions can be observed in the average median grain size distribution so we considered other methods for displaying this data. In the next section we will discuss additional insights into the deposit.

3.5.1 Grain Size Distribution Variability

While analyzing a single sample, we would frequently get two completely different grain size distributions even though the samples were well-mixed. An example of this can be seen in **Figure 3.5.2** with two varying grain size distributions for the middle layer of the A02 core sample taken at x=170 cm. **Figure 3.5.2 (a)** was the first subsample to be tested and had a median grain size of 811 microns. **Figure 3.5.2 (b)** was the fifth subsample to be tested and had a median grain size of 195 microns. Both of these subsamples were extracted from the same core sample after it had been well-mixed.

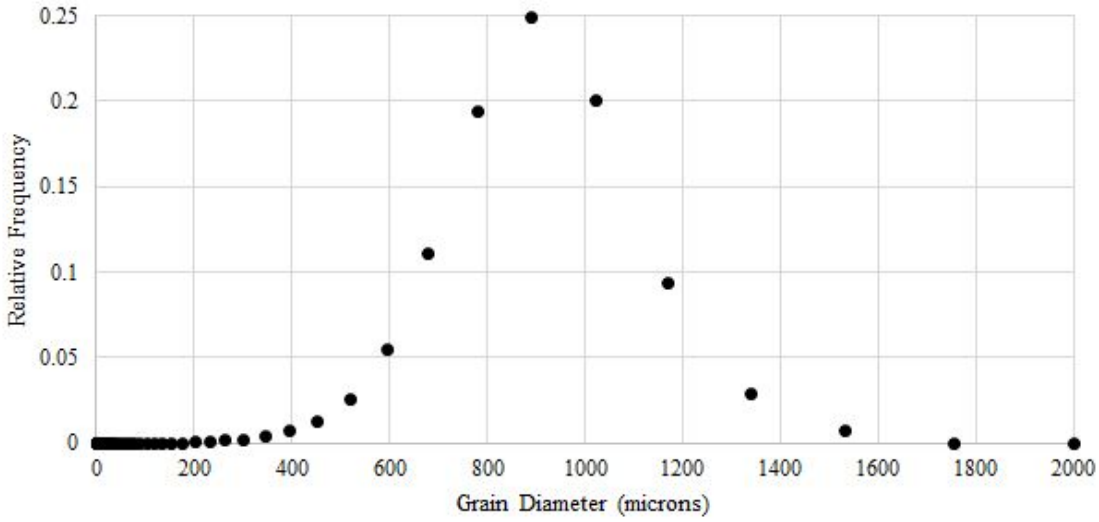

(a)

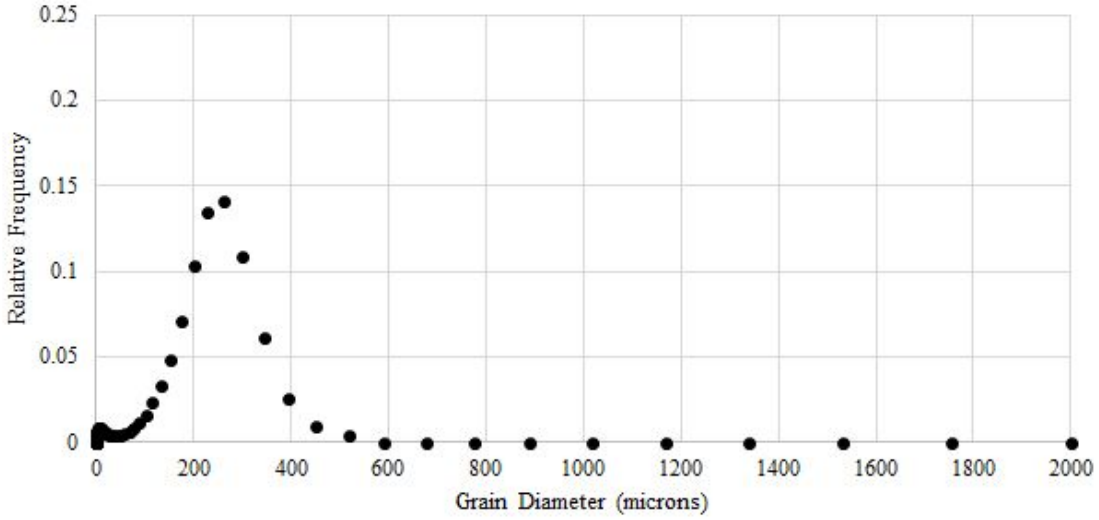

(b)

Figure 3.5.2: Grain size distributions for the middle layer of the A02 core sample located at x=170 cm where **(a)** was the first subsample to be tested and **(b)** was the fifth subsample to be tested. The median grain size for **(a)** was 811 microns and the median grain size for **(b)** was 195 microns. Both of these samples were taken from the same bottle after it had been well-mixed.

This concern is discussed more in section **5.2.3**. To ensure our subsampling methods were consistent and representative, we needed to condition the sample until an ideal water content was achieved that allowed particles to be stuck together with no

visible liquid that would separate the fines from the coarse particles of the sample. If the sample was too wet i.e. there was visible liquid in the sample bottle, the bottle and its contents were dried in an oven until the liquid was no longer visible. On the other hand, if the sample was too dry, water droplets were added to the sample until it reached the correct consistency.

We worked extensively to ensure our subsampling method and analysis methods with the laser diffraction analyzer were correct, and we still measured differing grain size distributions for the samples. We proceeded by assuming that the measured data was correct. Our solution to the same sample returning two very different grain size distributions was to average all of the distributions from each sample. An example of this can be seen in **Figure 3.5.3**. The plot shows the average relative frequency distribution for all of the subsamples taken from experiment A02 at coring location 170 cm in the middle section of the deposit.

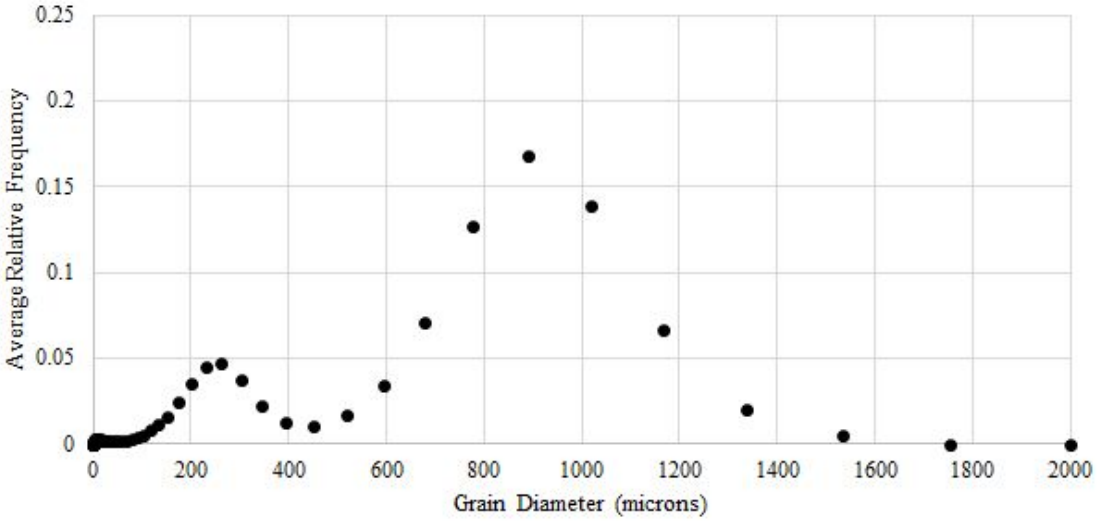

Figure 3.5.3: Plot of average relative frequency values for all of the samples taken, including the plots shown in **Figure 3.5.2 (a)** and **(b)**, from experiment A02 at the coring location 170 cm in the middle section of the deposit.

3.5.2 Downstream Trend

Figure 3.5.4 includes the average relative frequency distributions from upstream and downstream locations from the bottom layers of deposits formed during experiments A02 and A03. As was expected, downstream fining can be frequently seen in the bottom and middle layers of the A02 and A03 deposits.

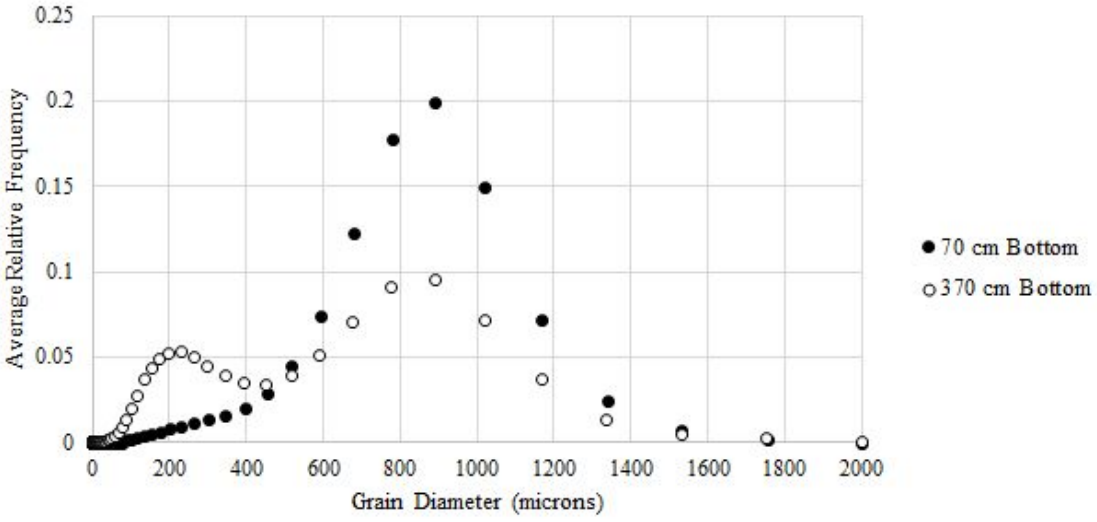

(a)

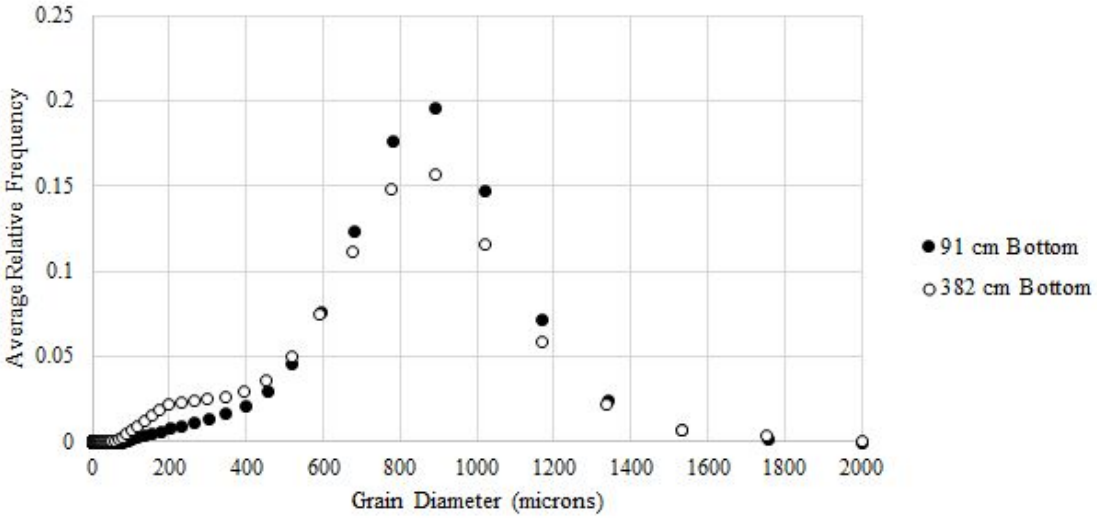

(b)

Figure 3.5.4: Plot of average relative frequency plots from **(a)** A02 and **(b)** A03 showing evidence for downstream fining in the bottom section of the deposits. Both of these plots exhibit a decrease in the size of

the large-grain size peak and an increase in the small-grain size peak at distances farther from the head of the flume.

As seen in **Figure 3.5.4 (a)**, the upstream average relative frequency distribution had a single large peak near 900 microns whereas the downstream distribution had a similar peak location but the peak was not as large. This would imply that fewer large particles traveled to the downstream coring location. The downstream distribution had a peak near 200 microns that the upstream distribution did not exhibit to such an extent; showing that there were more fine materials farther downstream in the flume. The 900 micron peak for the downstream distributions was also slightly skewed left which would indicate that there were fewer large particles farther downstream than there were upstream. Similar results are noted in **Figure 3.5.4 (b)** for experiment A03.

3.5.3 Vertical Trend

By breaking the core samples up into bottom, middle, and top sections, we were able to investigate how the samples varied in the vertical direction. We examined the grain size analysis results for the A02 core samples and noticed that the primary peak for the middle section had a slightly larger grain size diameter than the primary peak for the bottom section of the core sample. The intensity of the primary peak for the middle section was also greater than that of the bottom section. The bottom section also contained more fine-grain particles than the middle section. The top section had the least intense coarse-grained peak and the most intense fine-grained peak. This phenomenon was present throughout the length of the deposit and can be seen in **Figure 3.5.5 (a)** at 70 cm and **Figure 3.5.5 (b)** at 384 cm.

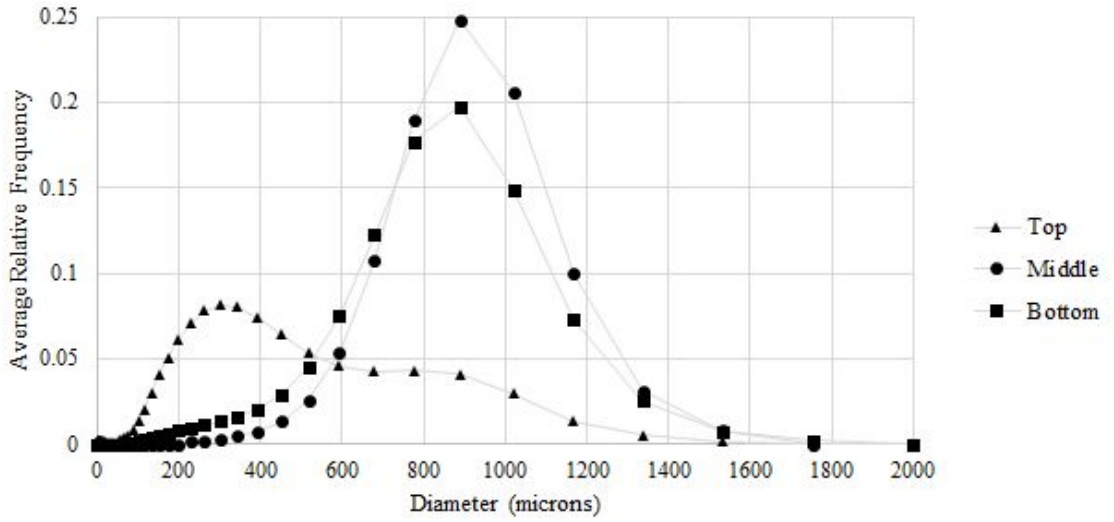

(a)

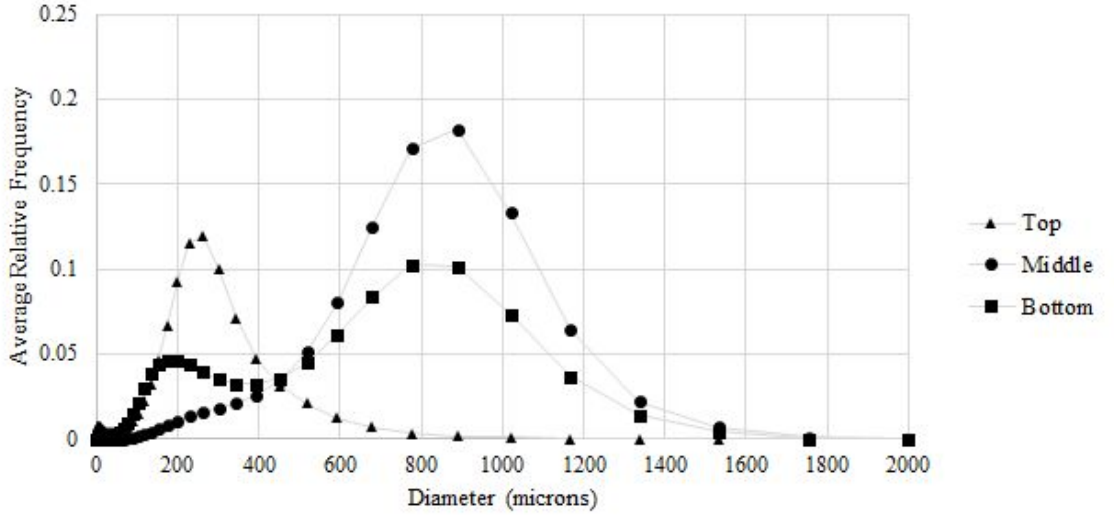

(b)

Figure 3.5.5: Grain size analysis results from core samples located at **(a)** 70 cm and **(b)** 384 cm from the start of the flume for experiment A02. **(a)** represents the upstream location while **(b)** represents the downstream location. These plots show evidence supporting our vertical trend persisted at both upstream and downstream locations.

These observations were also visible in the results of the grain size analysis for the core samples taken from A03 and are included in **Figure 3.5.6**.

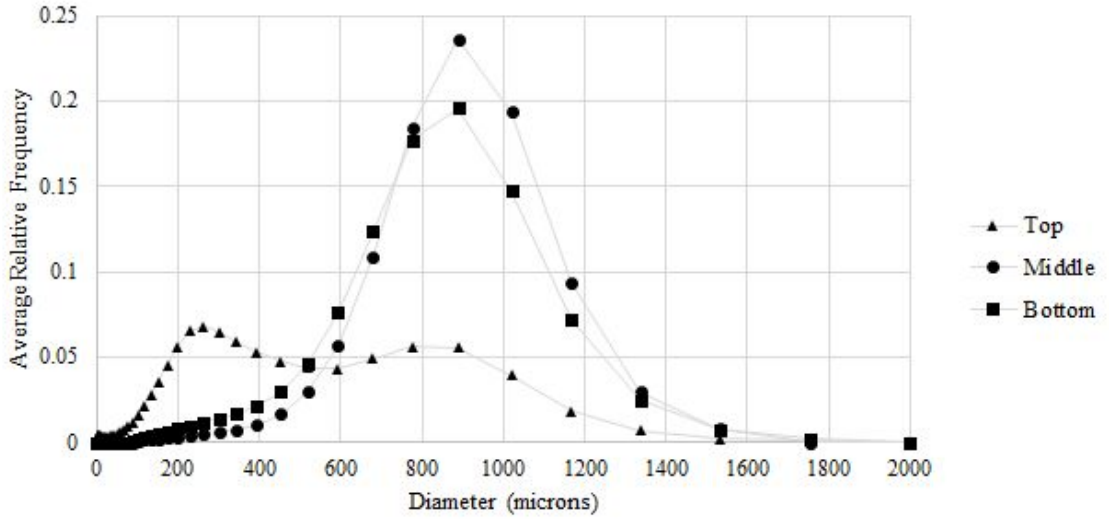

(a)

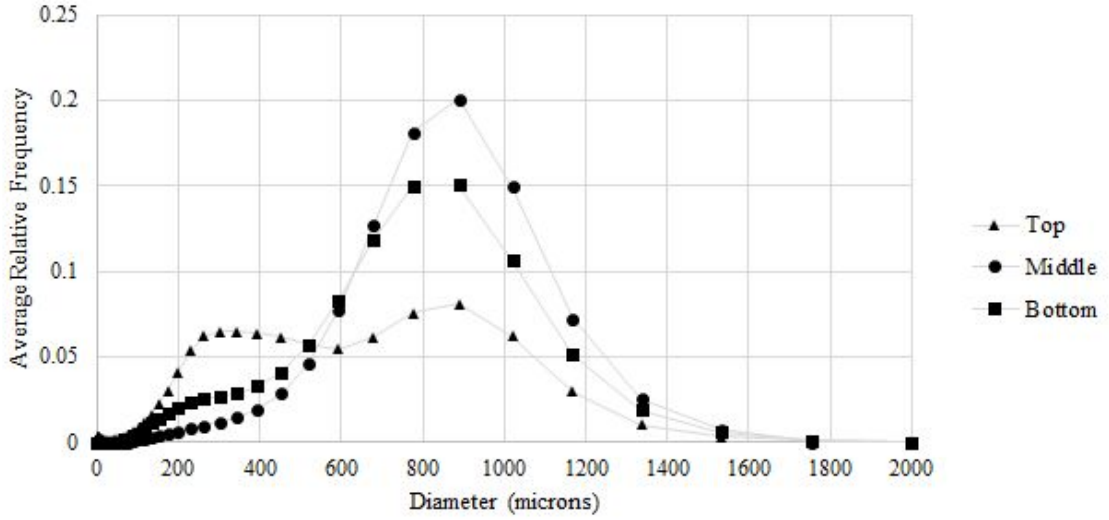

(b)

Figure 3.5.6: Grain size analysis results for core samples taken at **(a)** 91.3 cm and **(b)** 363.2 cm from the start of the flume for A03. **(a)** represents the upstream location and **(b)** represents the downstream location. These plots provide evidence for our vertical trend which was discovered at both upstream and downstream locations.

3.5.4 Finer Grains Capture in Topset

By comparing the average relative frequency plots from corresponding coring locations for both A02 and A03, we found the topset distribution for A02 had a higher small-grain peak. We tested this for another set of corresponding coring locations and observed similar results. The average relative frequency plots for the topsets depicting this trend are included in **Figure 3.5.7**. **Figure 3.5.7 (a)** shows the average relative frequency plots from the topsets of A02 at 170 cm and A03 at 227 cm. **Figure 3.5.7 (b)** includes the average relative frequency plots from the topsets of A02 at 270 cm and A03 at 295 cm. The corresponding coring locations are shown in **Table 3.4.1**.

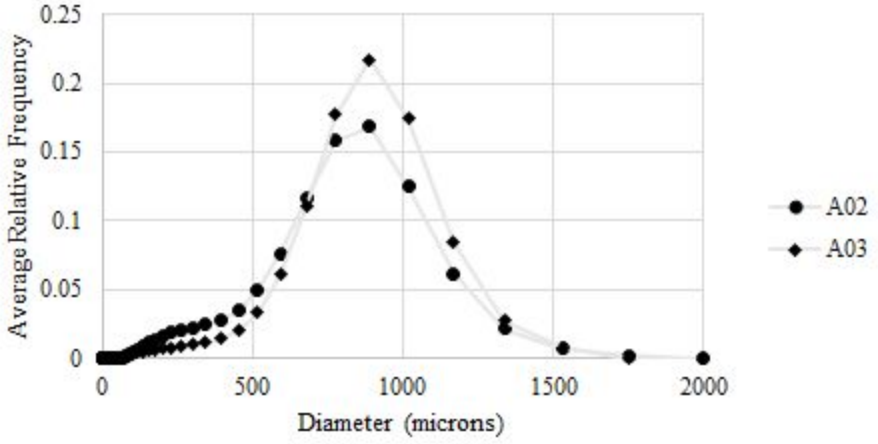

(a)

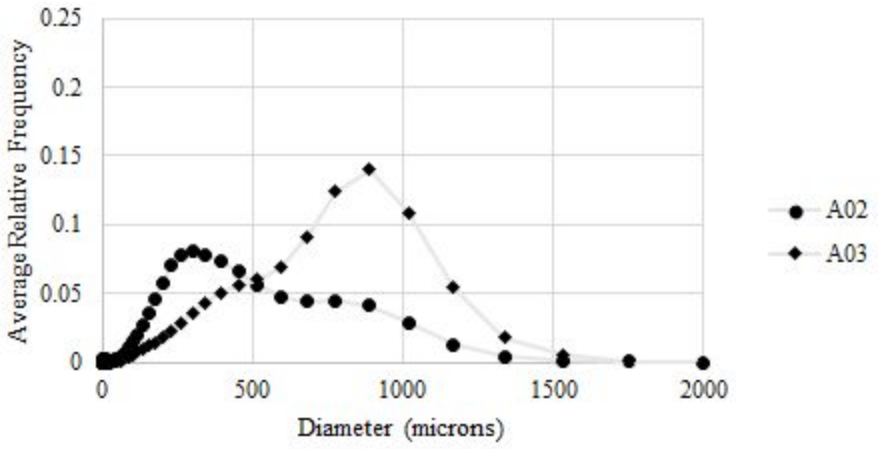

(b)

Figure 3.5.7: Average relative frequency plots for the topset of equivalent coring locations for A02 and A03. **(a)** shows the average relative frequency plots from the topsets of A02 at 170 cm and A03 at 227 cm. **(b)** includes the average relative frequency plots from the topsets of A02 at 270 cm and A03 at 295 cm. The corresponding coring locations are shown in **Table 3.4.1**. By comparing **(a)** and **(b)**, we found the topset of A02 demonstrated slightly higher small-grain peaks in both plots. This displays the enhanced capture of finer grains along the topset for experiment A02 which had a smaller inflow of materials. This observation was typical for the averaged relative frequency plots for the topset at other coring locations.

The plots shown in **Figure 3.5.7** display typical results for other coring locations. By comparing **Figure 3.5.7 (a)** and **(b)**, we found the plots from A02 both demonstrated a slightly higher small-grain peak. This observation implies the enhanced retention of finer grains along the topset for experiment A02 which had a smaller inflow of materials. More discussion on these results is included in section **3.6.5**. This is an important discovery for the oil sands industry and we discuss it further in section **3.7**.

3.6 Analysis and Discussion of Results

In this section, we provide details concerning the notable behaviors we observed in the results of our experiments with anthracite coal and kaolinite clay. We first provide a detailed look into the formation of these particular trends and further explore the reasoning behind these trends. Finally, we compare our results to the Gilbert deltas examined by Kleinhans.

3.6.1 Examination and Discussion of Profile Trends

Recall from section **3.3.1 Plots of Profiles**, we display profiles of the deposits at various times throughout experiments A02 and A03. As was evident from these plots, the deposits for both cases aggraded more significantly perpendicular to the surface of the foreset than the topset. Witnessing the deposit prograde primarily in the downstream

direction is what we would expect for a system with a constant sediment supply and a relatively stable water level such as ours (Paola et al., 2011).

In nature, if a river is unable to transfer bedload or channel material, then the material is deposited in the channel and aggradation occurs (Mugade & Sapkale, 2015). For our experiments, a large amount of the sediment carried by the incoming flow traveled rapidly over the surface of the topset with high shear stresses, permitting a limited amount of the sediment to deposit. This behavior resulted in a relatively slow accumulation rate along the topset, as compared to the foreset region, and is consistent with the findings of others (e.g. Pirmez et al., 1998).

We can see from the plots shown in **Figure 3.3.1** that the edge of the topset remained consistently around 15 cm which matched the water level inside the flume set by the upstream and downstream weirs. Due to this fact, the downstream edge of the topset was limited in its growth adjacent to the surface of the topset. On the contrary, the portion of the deposit upstream from the edge of the topset was not barred by this feature, allowing for the topset to aggrade slightly upward. We calculated the area of the topset at each time step using the following equation:

$$A = \left[\int_{x=50\ cm}^{x=x_{edge}} (mx + b)dx \right] - \left[15\ cm \times (x_{edge} - 50\ cm) \right] \qquad \textbf{Equation 3}$$

where A is the area of the topset, x_{edge} is the horizontal location of the edge of the topset, m is the slope of the topset, and b is the y-intercept. The lower limit of the integral was set to 50 cm since all of the experimental deposits had stabilized topset slopes by this point in the flume. Aggradation rates for the topset were determined by comparing the area of sediment had aggraded in a set amount of time. The averages of the topset aggradation rates for experiments A02 and A03 are recorded in **Table 3.6.1**.

By using the previously mentioned average topset aggradation rates and additional experimental data, we established the average topset velocity or the normalization of the topset aggradation rate with the average length of the topset through the following equation:

$$v_{top,exp} = \frac{a_{top}}{\frac{d_{final}}{2}} \qquad \textbf{Equation 4}$$

where $v_{top,exp}$ denotes the average experimental velocity of the topset, a_{top} is the average topset aggradation rate, and d_{final} is the final length of the topset. The average experimental topset velocity corresponds with the movement of the topset perpendicular to the surface with time. The average experimental topset velocities for experiments A02 and A03 are also included in **Table 3.6.1**.

Exp. #	**Discharge, Q (L/s)**	**Average Topset Aggradation Rate, a_{top} (m^2/s)**	**Standard Deviation of a_{top} (m^2/s)**	**Average Experimental Topset Velocity, $v_{top,exp}$ (m/s)**	**Standard Deviation of $v_{top,exp}$ (m/s)**
A02	0.5	7.48×10^{-5}	2.44×10^{-5}	4.68×10^{-5}	1.53×10^{-5}
A03	1.0	1.35×10^{-4}	3.73×10^{-5}	8.44×10^{-5}	2.33×10^{-5}

Table 3.6.1: Discharge rates, average topset aggradation rates with standard deviations, and average experimental topset velocities with corresponding standard deviation for experiments A02 and A03. The average vertical topset aggradation rates refer to the amount the topset aggraded perpendicular to the topset surface in time. The velocity of the topset signifies the normalization of the aggradation rate of the topset with the average length of the topset.

We see from **Table 3.6.1** that on average, there was twice the amount of sediment deposited along the topset during experiment A03 as there was for A02 in a set amount of time. Additionally, the average experimental velocity of the topset for experiment A03 was double what we established for A02. Both of these outcomes are attributable to experiment A03 experiencing double the rate of sediment discharge into the system. The excess sediment was unable to be transported by the flow and contributed to the deposition along the topset. The extent of aggradation is equivalent to the difference in the sediment entering at the upstream end of the topset and the sediment transported out of the system at the edge of the topset.

Through viewing **Figure 3.3.1**, we notice that although there existed some aggradation of the topset in the adjacent to the topset surface, the majority of the growth took place normal to the surface of the foreset. One of the major limiting factors in the

topset progression was the water level inside of the flume. Since the upstream and downstream weirs kept the water level inside the flume constant throughout the duration of the experiments, the topset was unable to notably aggrade further.

With the intention of quantitatively demonstrating the average experimental velocity of the foreset, we again make use of the data recorded in **Figure 3.3.1**. This information enabled us to confirm the rate at which the foreset advanced adjacent to the surface and further calculate the average of these values for both experiments. The values produced from this work are included in **Table 3.6.2**.

Experiment #	**Discharge, Q (L/s)**	**Average Experimental Foreset Velocity, $v_{fore,exp}$ (m/s)**	**Standard Deviation of $v_{fore,exp}$ (m/s)**
A02	0.5	2.43×10^{-3}	8.42×10^{-5}
A03	1.0	4.70×10^{-3}	7.65×10^{-4}

Table 3.6.2: Discharge rates and average experimental foreset velocities with standard deviations for experiments A02 and A03. The velocities were found through tracking the downstream movement of the edge of the topset or the upper edge of the foreset with time and averaging the results.

The average experimental velocity of the foreset for experiment A03 is nearly double the rate for experiment A02, as displayed in **Table 3.6.2**. This trait, similar to what we witnessed in the velocity of the topset, is attributable to the larger discharge rate exhibited by experiment A03. Through comparing the average experimental velocity values for the topsets in **Table 3.6.1** and the average experimental foreset velocities, we see that the foreset velocities far surpass the topset velocities. For both experiments, the foreset velocities are over fifty-times what we determined for topset velocities. The certainty of these values is displayed by the relatively standard deviation values we calculated and included above.

3.6.2 Discussion of Final Slope Trends

As was previously introduced in section **3.3.2**, the final topset slopes for experiments A02 and A03, shown in **Table 3.3.1**, vary roughly by a factor of two. Experiment A02 had half the discharge rate into the flume resulting in the flow across the topset to travel at a slower rate since the velocity of fluid flow is proportional to inflow. This system still required the movement of the sediment and fluid across the topset to accommodate the continuous introduction of new material. Subsequently, this required the slope of the topset to adjust by steepening and therefore allow for the materials to flow more easily in this region. For A03, the experiment with the higher inflow rate, the slope did not have to steepen to allow for proper flow since the materials were traveling at a faster rate along the topset. The forces acting on the uppermost layer of sediment along the topset include gravity pulling downward, shear stress from the bed opposite the direction of flow, and shear stress from the fluid acting with the direction of flow. The slope of the topset is set so that the shear stress of the fluid on the sediment allows for the sediment to flow downstream. If an experiment would have a different inflow rate, the system would respond by altering the slope of the topset in a similar fashion.

When the sediment-laden flow arrives at the edge of the topset, it experiences a sudden and drastic increase in the deposit slope in addition to an increase in the fluid depth. The increased fluid depth results in a decline in the fluid velocity and subsequently reduces the shear stress of the fluid acting on the sediment. At this point, the gravity acting on the sediment dominates, causing the sediment to drop and collect at the upper-portion of the foreset. From there, the collection of sediment avalanches down the foreset surface after reaching the threshold of the static angle of repose and further sets the slope of the foreset to the dynamic angle of repose, as mentioned by Kleinhans.

For the bottomset, the fluid velocity in the downstream direction dropped substantially and allowed for the sediment to settle. As is evident in the deposit profiles, such as **Figure 3.3.2**, more settling occurred closer to the foreset rather than farther downstream in this space. This phenomenon is attributable to gravity which pulled the larger suspended sediment out of the fluid sooner, before being transported farther downstream in the flume. The amount of sediment that was allowed to settle along the

bottomset gradually decreased horizontally and resulted in a smooth, shallow slope in this region. The bottomset slopes between these two experiments are very similar, contributing to the fact that these regions were formed almost completely through settling and doubling the inflow rate of material did not substantially affect this action.

3.6.3 Discussion of Sediment Transport Trends

In this section we work to further understand the transport and aggradation trends we observed during our surrogate experiments. When the slope of the topset is set in such a way that the flow can transport all of the sediment entering the system, we would anticipate no aggradation to occur. However, if the flow is unable to perform this transport there would be deposition throughout the topset region. We quantify the capacity of the flow or the expected sediment transport according to bed slopes, flow depth, and water discharge then compare the capacity with the discharge of the sediment and water mixture into the system. If these values are the same, we would predict that the discharge at the upstream end of the topset would be the same as that at the downstream end. When the transport capacity is less than the supply, some sediment is deposited to develop the topset which results in less material arriving at the front to aggrade the foreset.

We start by calculating the sediment supplied at the inlet. We assume that the flow occurring across the topset does not vary throughout the width of the flume so we consider the unit discharge of sediment:

$$\frac{Q}{b} = q_{mix} \qquad \textbf{Equation 5}$$

with Q being the volume discharge of the fluid and sediment mixture, b being the width of the flume, and q_{mix} as the unit discharge of the mixture. Since there are exclusively two main components to the mixture and we are simply concerned about the transport of the sediment, we can break the unit discharge of the mixture into two parts:

$$q_{mix} = q_{sed} + q_{water} \qquad \textbf{Equation 6}$$

where q_{sed} represents the transport of sediment and q_{water} is the transportation of the water. In order to determine how much of the transport was sediment, we multiplied the transport of the mixture by the percent of the volume that was sediment, *% Vol. of Sed.*:

$$q_{sed} = q_{mix} \times (\%\ by\ Vol.\ of\ Sed.) \qquad \textbf{Equation 7}$$

We consider these quantities experimental total sediment transport and have them included in **Table 3.6.3.**

Next, we calculate the sediment transport capacity of our measured hydraulic conditions. That is, we use the depth and slope over the topset in combination with published sediment transport predictions to calculate the likely transport of sediment across the topset.

So to predict the portion of the total sediment transport that occurred in bedload, we consider the well-known formulation initially introduced by Meyer-Peter and Müller (1948) and later corrected by Wong and Parker (2006):

$$q_b^* = 3.97(\tau_b^* - 0.0495)^{1.50} \qquad \textbf{Equation 8}$$

where q_b^* is the dimensionless bedload sediment transport and τ_b^* represents the dimensionless shear stress at the bed. From the dimensionless bedload sediment transport calculated using the Wong and Parker corrected Meyer-Peter and Müller equation we can further determine the dimensional bedload sediment transport using:

$$q_b = q_b^* \sqrt{RgD} D \qquad \textbf{Equation 9}$$

where q_b is the dimensional bedload sediment transport, R is the submerged specific gravity, g is gravity, and D is the grain diameter. Before calculating the sediment transport, we need to first find the shear stress, τ, of the bed using:

$$\tau = \rho_f g H S \qquad \textbf{Equation 10}$$

with ρ_f as the density of the fluid, H as the height of flowing fluid, and S as the slope of the bed. Then, to get the dimensionless shear stress, τ^*, of the bed, we use:

$$\tau^* = \frac{\tau}{(\rho_s - \rho_f) g D} \qquad \textbf{Equation 11}$$

where ρ_s is the density of the sediment. The values calculated via the Wong and Parker correction of the Meyer-Peter and Müller equation are visible in **Table 3.6.3**.

In an attempt to further investigate our experimental sediment transport values, we consider total sediment transport as described by Engelund and Hansen (1967), who theorized about the sediment transport of alluvial streams. In this context, total sediment transport or total load includes both suspended and bedload transport and is therefore more appropriate for use in high transport conditions such as these. For the purposes of this thesis, we use the generalized Engelund and Hansen equations presented by Naito et al. (2019). The dimensionless total sediment transport, q_t^*, according to Engelund and Hansen is determined via:

$$q_{EH}^* = \frac{0.05}{C_f}(\tau^*)^{5/2} \qquad \textbf{Equation 12}$$

where C_f is a friction coefficient and τ^* is the dimensionless shear stress. In order to calculate the dimensionless shear stress of the bed, we determine the bed shear stress for the Engelund and Hansen equation:

$$\tau_{EH} = \rho_{mix} g H S \qquad \textbf{Equation 13}$$

with τ_{EH} as the bed shear stress for the Engelund and Hansen transport equation, ρ_{mix} as the density of the water-sediment mixture, g as gravitational acceleration, H as the flow depth, and S as the downstream channel slope. For the dimensionless bed shear stress, we use the following equation:

$$\tau^* = \frac{\tau_{EH}}{(\rho_s - \rho_f) g D} \qquad \textbf{Equation 14}$$

in which ρ_s denotes the sediment density, ρ_f signifies the density of the fluid, and D represents the median grain size. So as to calculate the friction coefficient for the dimensionless total sediment transport equation, we use another equation presented by Engelund and Hansen:

$$C_f = \frac{u_*^2}{U^2} \qquad \textbf{Equation 15}$$

where u_* is the shear velocity and U is the depth-averaged flow velocity. The shear velocity is determined using the equation:

$$u_* = \sqrt{\frac{\tau_{EH}}{\rho_{mix}}} \qquad \textbf{Equation 16}$$

We are able to compute the depth-averaged flow velocity by dividing unit discharge of the mixture into the system, q_{mix}, by the flow depth, as shown here:

$$U = \frac{q_{mix}}{H}$$ **Equation 17**

To dimensionalize Engelund and Hansen's total sediment transport, we use the equation included below:

$$q_{EH} = q^*_{EH}\sqrt{RgD^3}$$ **Equation 18**

where q_t denotes the total sediment transport and *R* symbolizes the submerged specific gravity of the sediment. The resultant total sediment transport values determined from Engelund and Hansen's work are documented in **Table 3.6.3.**

To compare the amount of sediment that the system had the capacity to transport according to Engelund and Hansen with the quantity that was physically transported, we calculated the ratio of these values and included them in **Table 3.6.3**. These ratios revealed that the experiment with the lesser inflow rate had the capacity to transport a larger portion of the newly introduced sediment. This finding contradicts our expectations considering experiment A03 had twice the inflow of sediment, requiring more sediment to be transported.

The Engelund and Hansen transport values were calculated assuming the density of the flow over the topset was equivalent to the density of water, when in fact, the flow density was higher due to the sediment suspended in the flow. To account for this, we modified the density values used for the Engelund and Hansen transport values. With these adjusted density values, our modified Engelund and Hansen transport capacities for both experiments are on the same order of magnitude as our experimental sediment transport values. The modified sediment transport ratios better match our predictions where both experiments have roughly half of the sediment being fed into the flume being transported across the topset. The modified Engelund and Hansen total sediment transport values and the modified sediment transport ratios are documented in **Table 3.6.3**.

Exp. #	Q (L/s)	Exp. Total Sediment Transport, q_{sed} (m^2/s)	MPM-WP Bedload Transport, q_{MPM-WP} (m^2/s)	EH Total Sediment Transport, q_{EH} (m^2/s)	Sediment Transport Ratio (-)	Modified EH Density (kg/m^2)	Modified EH Total Sediment Transport, q_{EHm} (m^2/s)	Modified Sediment Transport Ratio (-)
A02	0.5	2.50×10^{-4}	4.31×10^{-5}	2.34×10^{-5}	0.0936	2000	1.33×10^{-4}	0.532

A03	1.0	5.0×10^{-4}	2.99×10^{-5}	3.53×10^{-5}	0.0706	2000	2.01×10^{-4}	0.403

Table 3.6.3: Collection of discharge rates, experimental total sediment transport values, Wong and Parker corrected Meyer-Peter and Müller bedload transport values, Engelund and Hansen total sediment transport values, sediment transport ratios, modified densities, modified Engelund and Hansen total sediment transport values, and modified sediment transport ratios for experiments A02 and A03.

As we can see from **Table 3.6.3**, the bedload transport values according to the corrected Meyer-Peter and Müller equations imply that the majority of the transport occurred as suspended load transport as opposed to bedload. We expected the results from the Wong and Parker corrected Meyer-Peter and Müller equation to be small since it only considers the transport of the bedload and not suspended load. For these reasons, we discount these values from further analysis.

Following the methods mentioned in Naito et al. (2019), we consider replacing the fluid density with the density of the sediment and fluid mixture for the Engelund and Hansen calculations. Consequently, we do not have access to the precise quantity of the suspended sediment; therefore, we can only estimate the value based on observations of our significant suspended load. To accomplish this, we consider the sediment suspended by the fluid causing an increase in the density of the flow since the sediment density is higher than the density of water. We arbitrarily selected a flow density equal to twice the value of the fluid density. This selection is acceptable considering the density of coal is 1.495 g/ml and the density of clay is 2.82 g/ml. The modified density values provided us with reasonable modified Engelund and Hansen total sediment transport values on the same order of magnitude as the experimental total sediment transport values. If roughly half of sediment that is fed into the flume arrives at the edge of the topset, we know that the remaining portion of the sediment was deposited along the topset. This addition of sediment along the topset contributes to the topset velocity. When the inflow of sediment is doubled, there would be twice the amount of sediment introduced to the flume at the head of the topset. Again, if around half of the sediment is transported across the topset, then the remaining portion would deposit on the topset. The amount of sediment left on

the topset for this experiment would be double the amount we saw with the previous experiment or double the average topset velocity. This would also be the case for the amount of sediment transported. A visual representation of this behavior is included in **Figure 3.6.1**.

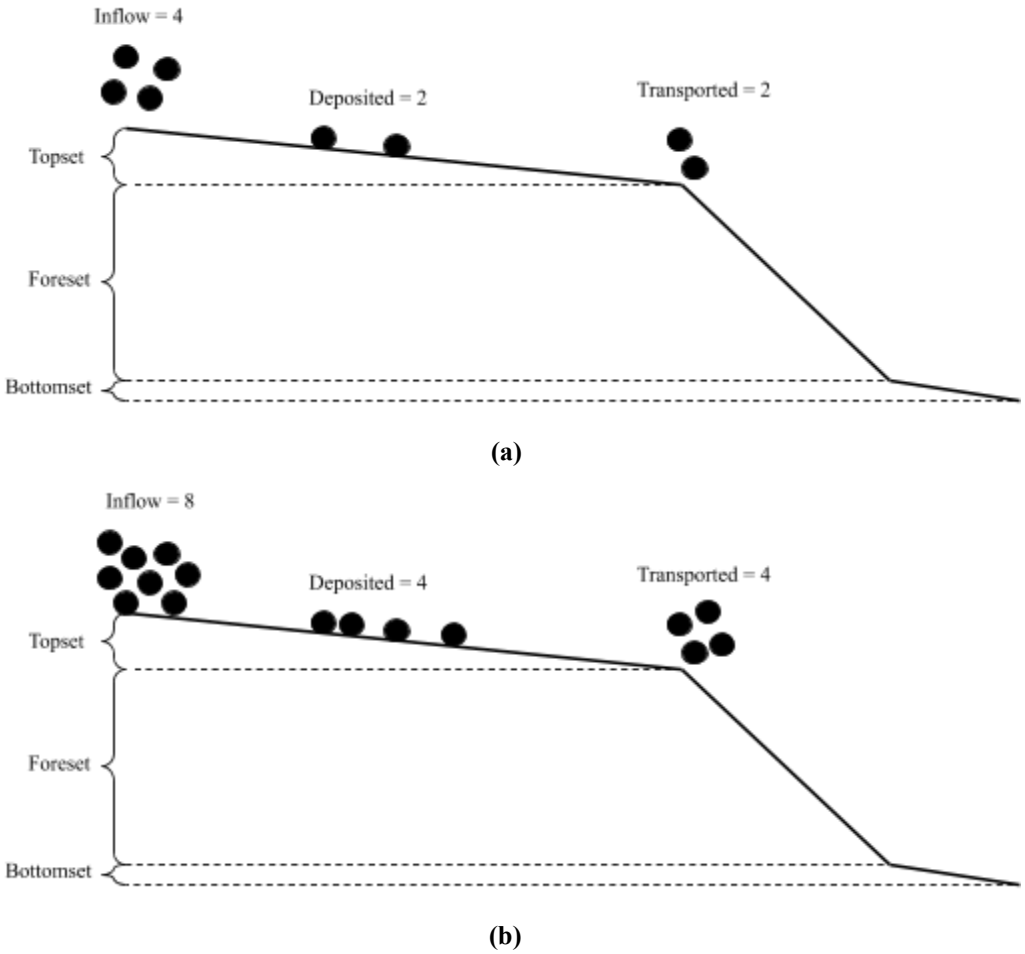

Figure 3.6.1: Simple depiction of deposition and transport behaviors witnessed along the topsets of **(a)** experiment A02 and **(b)** experiment A03. When the amount of sediment introduced at the inlet is doubled, there is twice the amount of sediment deposited along the topset, doubling the topset velocity. This situation also results in double the amount of sediment transported to the edge of the topset.

At this point, we had acquired sufficient information to determine theoretical topset and foreset velocities to compare with our previously mentioned experimental values. In order to identify our theoretical velocities, we assumed the quantity of topset aggradation equated to the difference in the feed of sediment into the system and the

amount of sediment transported away from the topset. We calculated our theoretical average topset velocities from dividing this difference by the average length of the topset and our approximated solid fraction, as shown here:

$$v_{top,theory} = \frac{q_{exp} - q_{EHm}}{SF \times d_{avg}} \quad \textbf{Equation 19}$$

where $v_{top,theory}$ is the average theoretical topset velocity, q_{EHm} represents the modified Engelunds and Hansen total sediment transport values, SF is the approximated solid fraction of 0.6, and d_{avg} is the average length of the topset. The average theoretical topset velocities for experiments A02 and A03 are presented in **Table 3.6.4**.

When calculating the average theoretical foreset velocity, we consider all of the sediment transported according to the modified Engelund and Hansen values to be spread evenly over the surface of the foreset. The average theoretical velocity of the topset was then determined by dividing this value by the estimated solid fraction:

$$v_{fore,theory} = \frac{q_{EHm}}{SF \times h_{avg}} \quad \textbf{Equation 20}$$

where $v_{fore,theory}$ symbolizes the average theoretical foreset velocity and h_{avg} is the average length of the foreset. The results from this work are documented in **Table 3.6.4**.

Exp #	Q (L/s)	Average Experimental Topset Velocity, $v_{top,exp}$ (m/s)	Average Experimental Foreset Velocity, $v_{fore,exp}$ (m/s)	Average Theoretical Topset Velocity, $v_{top,theory}$ (m/s)	Average Theoretical Foreset Velocity, $v_{fore,theory}$ (m/s)
A02	0.5	4.68×10^{-5}	2.43×10^{-3}	1.22×10^{-4}	1.48×10^{-3}
A03	1.0	8.44×10^{-5}	4.70×10^{-3}	3.11×10^{-4}	2.23×10^{-3}

Table 3.6.4: Average theoretical topset and average theoretical foreset velocities for experiments A02 and A03 with discharge values. The theoretical values were established by dividing the accumulation of sediment by the length of the region and the solid fraction.

Similar to the average experimental topset and foreset velocities, the average theoretical values for experiment A03 are nearly double those found for A02. This matched what we expected with having twice the amount of sediment deposited along the

topset when the amount of sediment fed into the flume was doubled. Similar to our experimental results, the average topset velocities were significantly smaller than the average foreset velocities, further providing a physical justification for the difference in aggradation rates.

For the topset, our average theoretical velocities surpassed our experimental values which suggests our theory underpredicted the sediment transport capacity of the flow. Effectively, this was represented in the theoretical prediction as excess sediment along the topset that contributed to the overprediction of the topset velocity.

The average theoretical foreset velocities were very similar to our experimental values and only underpredicted the velocity values slightly. The smaller theoretical values may indicate our theory overestimates the solid fraction or the average length of the foreset. It is also possible there was more sediment transported than what the modified Engelund and Hansen total sediment transport values predicted as mentioned in the previous paragraph.

3.6.4 Description of Grain Size Trends

The grain size analysis for both A02 and A03 resulted in extreme variability in sample grain size distributions despite multiple attempts at reducing this effect. The variability visible in **Figure 3.5.2** was somewhat resolved by averaging all of the grain size distributions that came from the same sample bottle i.e. the same location and section of the deposit as seen in **Figure 3.5.3**.

By looking at grain size distributions from the bottom sections of the deposits formed during experiments A02 and A03, we found evidence for downstream fining as shown in **Figure 3.5.4**. The plots proved that the samples from farther downstream locations had a less intense larger-grain size peak and a more intense small-grain size peak.

Figures 3.5.5 and 3.5.6 allowed for us to examine the vertical variability in the A02 and A03 deposits at both upstream and downstream locations. For both experiments,

we observed that the middle section of the deposits had the largest large-grain size peak and the smallest small-grain size peak compared to the other sections. It was also determined that the bottom section had a medium sized large-grain peak and a medium small-grain peak. We also found that the top section had the smallest large-grain size peak and the largest small-grain peak.

As we saw in **Figure 3.5.7**, there was more retention of finer grains in the topset during experiment A02 when compared to A03 at corresponded deposit locations. This trend appeared in the plots as a slightly higher small-grain peak for the A02 distributions.

3.6.5 Reasons Behind Grain Size Trends

There are many potential reasons as to why we witnessed such intense variability in our grain size distribution results. Although there was extensive mixing performed on each of the samples, it is possible that this measure was not enough to properly intermix the particles before they were placed in the Horiba. There is a chance that when the samples were dampened that particles of similar sizes remained together in clumps and that the mixing performed was unable to separate those clumps which brought into fruition the profound variability between each of the samples evaluated by the Horiba.

The bottom section of the A02 and A03 deposits exhibited a downstream fining trend due to gravity causing larger grains to settle closer to the inlet. Particles that were suspended in the fluid were propelled past the edge of the topset into a region where the flow decreased dramatically. At this point, the suspended particles were allowed to settle. The particles that settled first, as a result of gravity, were the largest of those suspended at locations closer to the head of the flume or farther upstream. The smaller particles remained in suspension for longer and progressed farther downstream before depositing. We found this particular downstream trend to be more prevalent in the bottomset since it was primarily formed by the action of settling and not the more complex mechanisms such as those present in the formation of other layers of the deposit.

As for the vertical trend, we have many assumptions as to the grain sizes exhibited by each of the deposit layers. We presume that the sediment that made up the bottom layer was a combination of different sizes of sediment that settled after the initial plume traveled downstream as well as throughout the experiment before being covered by the foreset. Some of the larger particles that settled during this time likely captured some small-sized particles. These behaviors would result in the finding that we observed. For the middle section of the deposit, we saw mostly large particles, placed there by the avalanching front. The fact that primarily large particles were captured at the upper end of foreset would explain the results we found for this section. For the topmost section of the deposit, we saw a roughly even mix of large- and small-grain sediment. These results can be attributed to the fact that this section included some of the avalanching front as well as the materials that settled after the experiment had finished.

We know that the inflow rate of the fluid and sediment mixture directly affects the flow velocity and therefore the bed shear stress. Due to this, if we have a higher inflow of materials, the flow across the topset will increase as well as the shear stress at the bed. When the flow across the topset was doubled for A03, fewer small grains were able to remain in this region and as a result, these grains were transported past the topset. The transport of the finer grains away from the topset is interpreted as a decrease in the retention of smaller grains. When the smaller particles were transported past the topset, they were typically suspended in the pond and remained in suspension due to their lower settling velocities.

There were four mechanisms that contributed to both the vertical and downstream segregation dynamics including: variable settling velocity, kinetic sieving on the steep foreset, differing mobility, and winnowing. The varying settling velocities of the grains contributed to the downstream fining in that fast settling particles dropped out of suspension farther upstream than grains with slower settling velocities. The shear segregation along foreset aided the front in resurfacing and deposited large particles closer to the bottomset. The differing mobility contributed to the sorting when smaller grains were forced into small pore spaces while larger grains continued to progress down

the foreset slope during avalanches. Winnowing affected the retention of finer grains along the topset of the deposits. When the flow increased, winnowing occurred which caused many smaller grains previously deposited to become agitated and from there, transported across the topset (McCrone, 1962).

In order to further understand the reasoning for the additional fines in the topset, we consider reviewing the work completed in Parker (1990) which studied the change in surface segregation conditions with surface shear stress. The further investigation of this behavior is beyond the scope of this work.

3.6.6 Comparison to Gilbert Delta Sorting Experiments

Summary of Kleinhans' Sorting Experiments

Gilbert deltas are often found in nature when rivers deposit large, coarse sediment into freshwater lakes. Since we are concerned with the sorting and segregation that occurs in this type of formation, we looked into the work completed by Kleinhans, who extensively studied the sorting mechanisms occurring at the lee slope or foreset of deltas. In his experiments, Kleinhans worked with a narrow flume and varied flow conditions as well as sediment mixtures, similar to our experiments. Some of the experiments studied by Kleinhans used sand and gravel mixtures as well as some purely sand mixtures. Kleinhans recorded a similar overall decrease in grain size and the accumulation of sediment with downstream distance from the delta that we also observed. Similar to our own experiments, Kleinhans noted the deposition of transported sediment on the upper part of the foreset which he called grainfall. Once this material exceeded a threshold, it flowed down the slope in an action he called grainflow. In both our experiments and the sand experiments studied by Kleinhans, there was a continuation of grainflows or avalanches that caused the delta to progress downstream.

Height Variations of Relative Grain Size

Kleinhans conducted a series of experiments with a variety of sediment mixtures that generally produced an upward fining trend as the result of kinetic sieving and grainflows. This vertical trend, as displayed graphically in **Figure 3.6.2**, was consistently presented in Kleinhans' deposits apart from the occasional deviation in the bottomset.

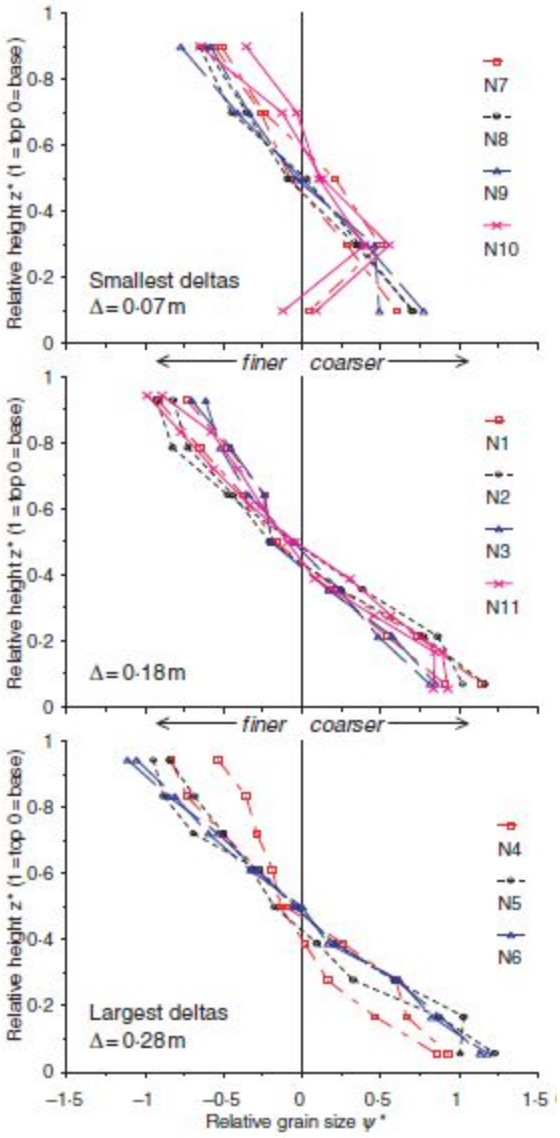

(a)

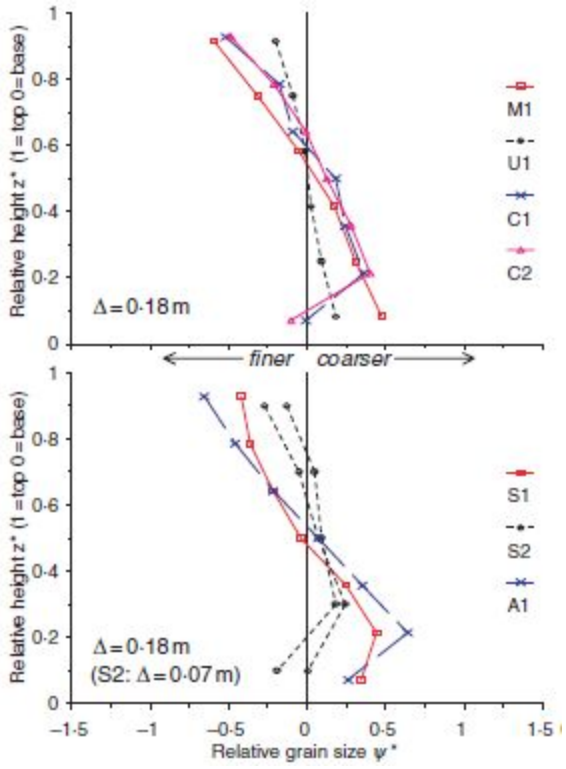

(b)

Figure 3.6.2: (a) Portrayal of the vertical grain size sorting trends that Kleinhans reported for his wide sand-gravel mixture and **(b)** Kleinhans' relative grain size plots for his various mixtures. Plots from Kleinhans (2005). The relative grain sizes were calculated according to **Equation 21**. The relative heights were calculated by dividing the local height by the total deposit height.

Kleinhans mentions that the deviation in the upward fining trend that he observed with some of his experiments was due to the mixing of the fine sediment from the bottomset and the coarse sediment from the lowest parts of the foreset.

We generated the overall average relative frequency distributions of the top, middle, and bottom layers for experiments A02 and A03 shown in **Figure 3.6.3 (a)** and **(b)**. To better compare our results with Kleinhans, we calculated our relative grain sizes with the following equation:

$$\psi^*_{rel} = log_2\left(\frac{D_{loc}}{D_{mix}}\right) \qquad \textbf{Equation 21}$$

with D_{loc} as the local median grain size for each area of the deposit, D_{mix} as the median grain size of the entire mixture, and ψ^*_{rel} representing the relative median grain size. We

established our relative heights according to **Table 3.6.5**. We plotted our relative grain sizes as a function of relative deposit height in **Figure 3.6.3 (c)**.

Deposit Layer	Relative Height
Top	1
Middle	0.67
Bottom	0.33

Table 3.6.5: Deposit layers and their corresponding relative heights used for our analysis.

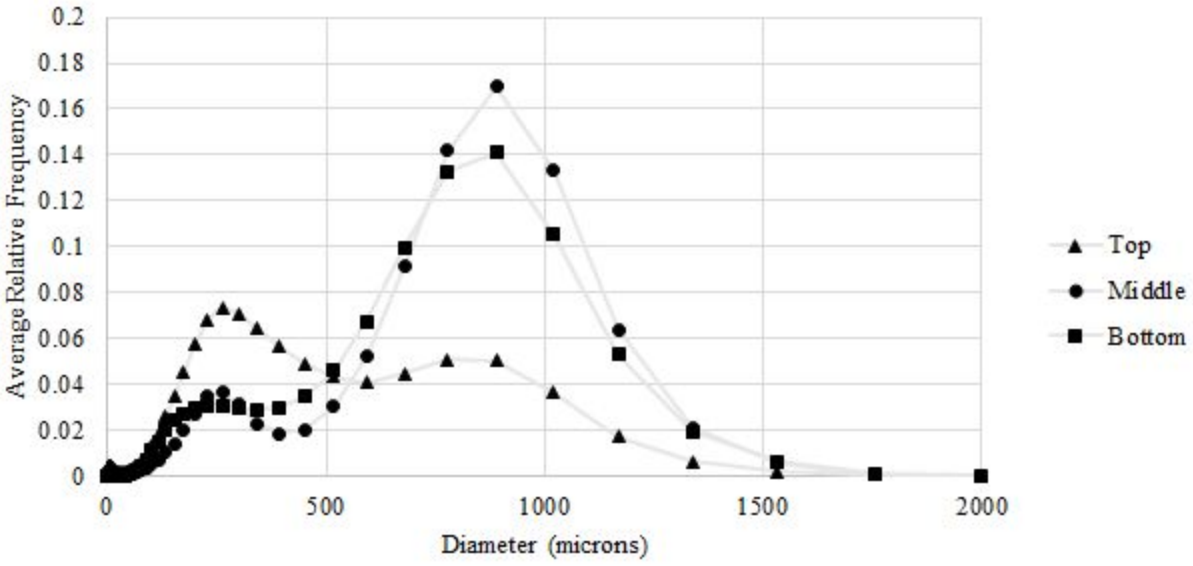

(a)

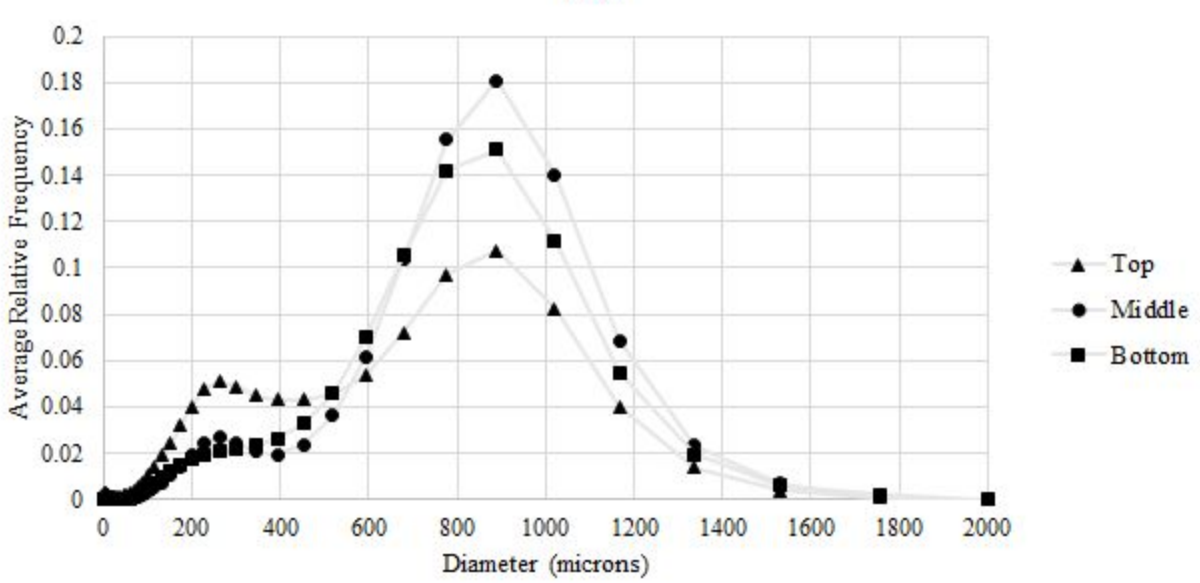

(b)

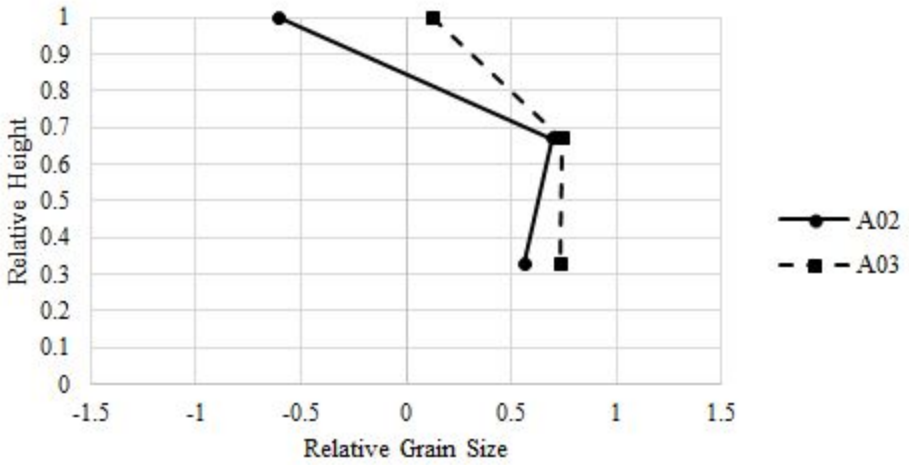

(c)

Figure 3.6.3: (a) Overall average relative frequency plot for A02 averaged for each deposit layer over all coring locations. We can see the highest large-grain peak in the middle layer, followed by the bottom, and then the top. This is the same case for A03 in **(b)**. We include the relative median plots for A02 and A03 in **(c)** to better compare with Kleinhans. The relative grain sizes were calculated according to **Equation 21** and the relative heights were established according to **Table 3.6.5**. We did not include the average relative frequency distributions from the coring locations where the deposit had not yet fully formed.

When comparing our relative grain size plots in **Figure 3.6.3 (c)** to those documented by Kleinhans in **Figure 3.6.2 (b)**, we see relatively similar upward fining trends. The plots shown in **Figure 3.6.2 (b)** were for Kleinhans' experiments with a variety of grain size distributions. The majority of the experiments conducted by Kleinhans using the wide sand and gravel mix, shown in **Figure 3.6.2 (a)**, did not display this variation in the upward fining trend. We present a detailed description of the vertical trend we observed for our experiments in section **3.6.5**. We further discuss the cause of the variation in the bottomset for both our experiments and those studied by Kleinhans in ***Formation of the Bottomset***.

Height Variation in Relative Standard Deviation

In order to observe the level of sorting in each layer of his deposits, Kleinhans generated relative standard deviation plots as shown in **Figure 3.6.4.**

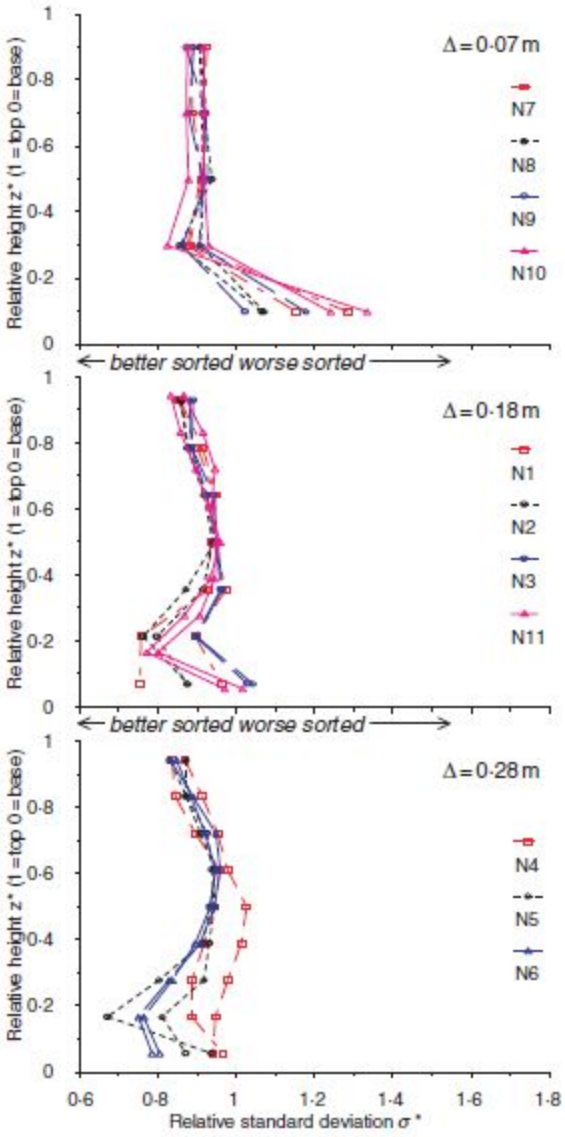
Δ = 0·07 m
N7
N8
N9
N10
Δ = 0·18 m
N1
N2
N3
N11
Δ = 0·28 m
N4
N5
N6
Relative height z* (1 = top 0 = base)
← better sorted worse sorted →
0·6
0·8
1
1·2
1·4
1·6
1·8
Relative standard deviation σ*

(a)

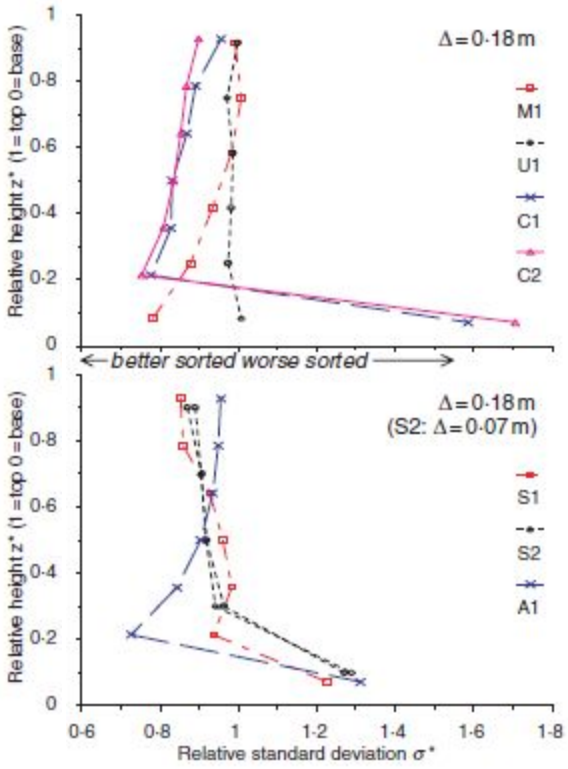

(b)

Figure 3.6.4: Relative standard deviation plots for Kleinhans' experiments with **(a)** a wide sand and gravel mix and **(b)** a variety of grain size distributions. Plots from Kleinhans (2005). Kleinhans calculated his relative standard deviation values according to **Equation 22**.

For Kleinhans, the relative standard deviations for his deposits were smaller than one since the sediment in the deposits was vertically sorted and therefore better sorted than a sample of the total mix. The occasional exception to this trend occurred in the bottom portion of **Figure 3.6.4 (b)**. According to Kleinhans, this was due to the fine sediment from the bottom of the deposit mixing with the coarse sediment from the lower section of the foreset. The mixing of the fine and coarse grains would result in larger relative standard deviation values while the rest of the deposit was well-sorted. Kleinhans mentions that this trend was only observed for the experiments conducted with a portion of fine grains.

We generated relative standard deviation plots for our experiments to compare with those displayed in **Figure 3.6.4**. The relative standard deviations were determined using the following equation:

$$\sigma^*_{rel} = \frac{\sigma_{loc}}{\sigma_{mix}} \qquad \textbf{Equation 22}$$

with σ_{loc} as the local standard deviation for each area of the deposit, σ_{mix} as the standard deviation of the entire mixture, and σ^*_{rel} representing the relative standard deviation. Our relative standard deviation plots are included in **Figure 3.6.5**. The relative heights were set by the values in **Table 3.6.5**.

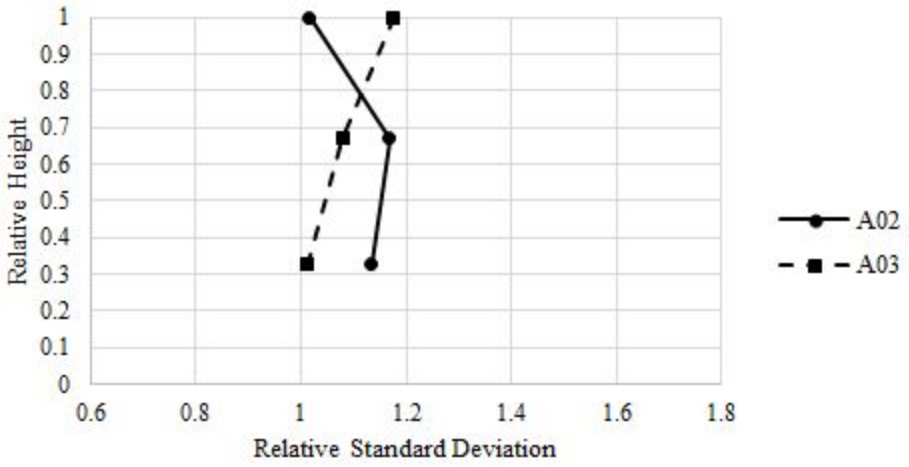

Figure 3.6.5: Relative standard deviations for A02 and A03 from **Figure 3.6.3** at various deposit heights. For A02, the sediment was better sorted at the top and least sorted in the middle of the deposit. For A03, the sediment was best sorted at the bottom and least sorted at the top of the deposit. The relative standard deviations were calculated according to **Equation 22** and the relative heights were established according to **Table 3.6.5**.

In **Figure 3.6.5** we can see our relative standard deviations were all fairly similar in size. Unlike Kleinhans, we did not see such extreme sorting as he detected in the bottom region of his deposits. This implies that overall, we did not see the extensive mixing of vastly varying grains anywhere in our deposits as Kleinhans did. From viewing **Figure 3.6.3 (a)** and **(b)**, we can see that all three of our deposit layers had relatively

similar spreads in their distributions. This is reasonable for the relative standard deviations that we plotted in **Figure 3.6.5**.

Formation of the Bottomset

As displayed in **Figure 3.6.2**, Kleinhans measured a reversal of the height-dependent segregation trend in the bottom layers of several deposits. We noticed a similar trend with all of our coal and clay experiments as shown in **Figure 3.6.3**. For Kleinhans, the grains found at the bottom were a mix of large particles and a significant fraction of smaller particles resulting in a significantly wide distribution. Kleinhans attributed this trend to a mixing of the previously settled fine grains in the bottomset and the largest grains from the foreset grainflow. Although we did discover some fines at the bottom of our deposits, this sediment did not affect our relative standard deviation in **Figure 3.6.5** to the extent Kleinhans observed in **Figure 3.6.4 (b)**. Thus, we attribute our reversal to a different effect. Our bottomset was formed as the result of two separate settling behaviors. The initial contribution to the formation of the bottomset occurred as some sediment settled after the plume travelled down the flume. The second and more significant contribution came from the deposition of the sediment that became suspended in the pond after being transported across the topset. The increased fluid depth in the pond allowed for the suspended grains to gradually settle and form the bottomset. The grains that made up the bottomset were smaller than the sediment found in the middle section, therefore producing a reverse height-dependent segregation trend in the bottomset.

Upward Fining Trend

Through viewing **Figure 3.6.2**, we can see that some of the sediment mixtures considered by Kleinhans revealed similar upward fining trends with the largest grains located at the bottom and the smallest grains at the top of the deposit. According to Kleinhans, the experiments that displayed this behavior were those that contained only

large grains such as sand and gravel. We did not achieve results such as these since our mixtures were not composed of large sediments such as gravel.

Grain Size Distribution of Mixtures

The experiments documented in Kleinhans (2005) were primarily performed with sand mixtures and some with sand and gravel with geometric mean sizes on the order of 1 mm. Our experiments, on the other hand, contained a portion of clay-sized particles with the typical grain size of 0.5 microns. We chose to include clay particles in our mixtures since this composition was an accurate representation of TSRU tailings produced by the oil sands industry. Additionally, these clay particles have relatively small settling velocities that added a unique component to our surrogate experiments.

Quantity of Suspended Sediment

Kleinhans states that during the formation of many of his deltas, there was very little suspended sediment downstream from the top of the delta. On the other hand, we had a fair amount of particles suspended in the pond or the fluid that collected downstream of the topset and foreset, above the bottomset. This suspended sediment caused the pond water to be cloudy throughout the duration of our experiments and even after the experiments had been completed. Once the suspended fines did completely settle, there was a thin layer of clay particles across the portion of the bottomset that had not been overtaken by the foreset of the deposit. It is likely that some of these clay particles were captured during the formation of the deposit as well.

Initial Flume Conditions

We realize that the initial conditions inside of the flume of our experiments presumably varied from those present for Kleinhans' work. For our experiments, we used a flume with the length of 10 m, a width of 10 cm, and a height of 50 cm whereas Kleinhans' flume had a length of 7 m, a width of 7.5 cm, and a height of 38 m. Although our experimental flumes had relatively similar dimensions, the initial conditions present

at the head of Kleinhans' flume varied greatly from our own. Whereas our inflow was first introduced to a stilling basin set by our upstream weir before progressing downstream, Kleinhans had his inflow first flow horizontally over a surface before traveling down a preset slope where the deposit was finally allowed to begin formation.

Conclusion

Although there were several differences between our experiments and those examined in Kleinhans (2005), we still found many similarities in the formation and development of our deposits. This could indicate that the proposals made by Kleinhans are more broadly applicable than just simply sand and sand-gravel mixtures but also for mixtures containing small-grained clay particles. Since these behaviors have also been noted in natural systems, it is further likely that actual TSRU tailings deltas in similar conditions would behave in this manner.

3.7 Conclusions from Coal and Clay Study

We initially compared various mixtures of sediment and water to the TSRU tailings sample we had received. After finding the closest surrogate mixture, we studied the settling rate of the initially settled layer in both the surrogate mixture and the TSRU tailings. We then examined our surrogate materials in detail by performing grain size analysis on them and viewing them under a microscope. With all of this information gathered, we ran our first experiment, A02, with a discharge rate of 0.5 L/s in our experimental flume. The videos and data we received from this run were compiled and studied. We also extracted core samples from various locations along the length of the deposit for the purpose of studying the variations of the deposit in the streamwise and vertical directions. This procedure was repeated for experiment A03 with the same surrogate mixture but with a discharge rate of 1.0 L/s.

From looking at our data and watching the videos, we noticed that the two deposits from both studies formed similarly with the shape of a Gilbert delta. At the start

of both experiments, a plume traveled the length of the flume, depositing sediment as it went. Then, a wedge of sediment started to form at the downstream end of the upstream weir that eventually flattened out on the top and the deposit began to advance downstream. This downstream movement was powered by the act of particles building up on the upper end of the foreset and then avalanching down the foreset. Graphical representations of the forward progression of the deposit front are included in **Figure 3.7.1**.

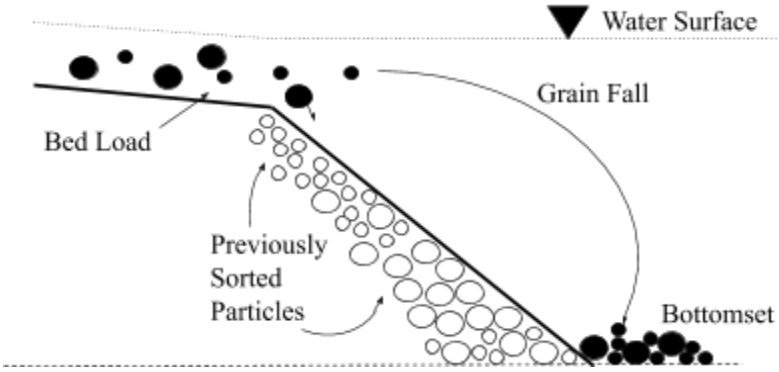

(a)

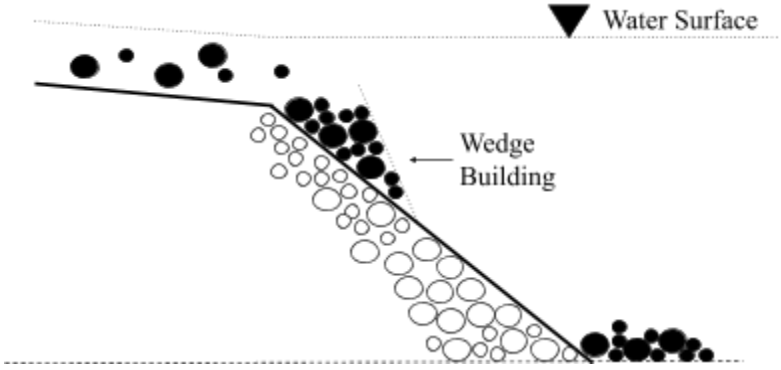

(b)

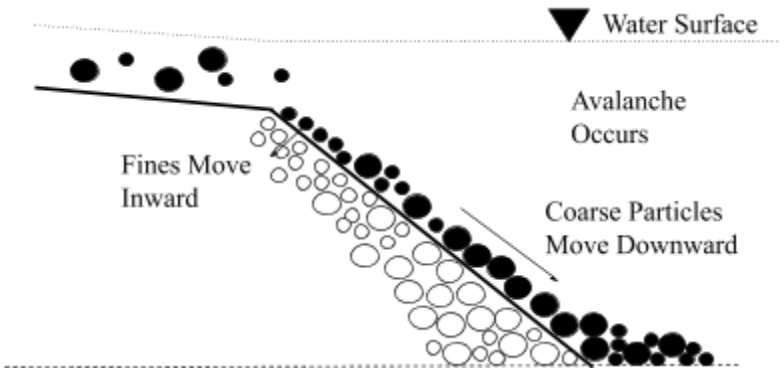

(c)

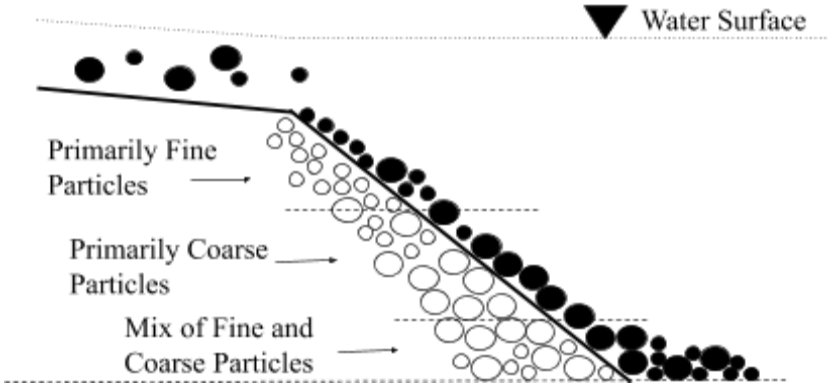

(d)

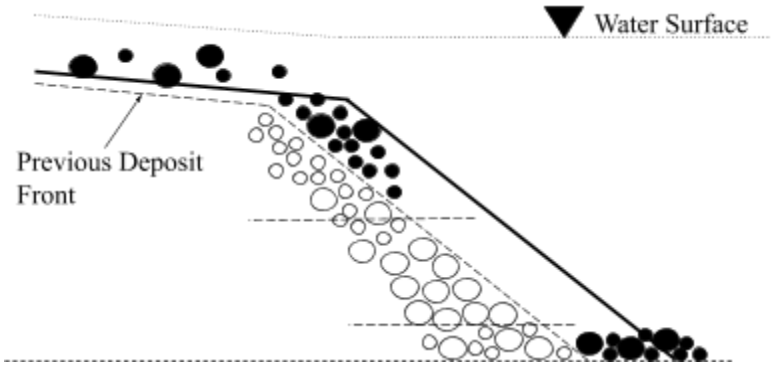

(e)

Figure 3.7.1: Sketches recounting the sorting mechanisms present at the fronts of our surrogate deltas, comparable to **Figure 1.3.3** from Kleinhans, 2005. **(a)** and **(b)** illustrate the initial stages where grain falls form the sediment wedge at the upper edge of the foreset and small grains fall to the bottomset. The second step is described in **(c)**, which includes the avalanching of the built up sediment and kinetic sieving. **(d)** represents the formation resulting from the previous stages. Finally, **(e)** presents the continuation of the earlier processes.

As time passed, the front of the deposit continued to progress downstream through aggradation. At the end of each experiment, the materials suspended in the fluid were allowed to settle and formed a thin layer over the deposit.

By examining the deposit profiles drawn for both experiments at various times, we perceived that the deposits progressed more in the direction perpendicular to the surface of the foreset than the topset in the same amount of time. These observations were later validated through further data analysis. The data from these experiments additionally revealed that the front of the deposit with double the inflow rate advanced downstream at nearly twice the rate. This was also the case for the upward rate of the topset. Furthermore, we discovered these results agree with our theoretical calculations.

From looking at the final topset, foreset, and bottomset slopes, we learned experiment A02 had steeper topset and foreset slopes. These slopes steepened in order to transport sediment more easily in these regions. The inflow rate for A03 was doubled so the topset and foreset slopes did not need to adjust in this manner. As for the bottomsets, the final recorded slopes were the same largely due to the fact that these areas were formed by settling and the greater inflow of material did not significantly affect this behavior.

Since the topset and the foreset velocities both doubled for experiment A03, we know that the modified sediment transport ratios for A02 and A03 would have to be similar. Our original and modified ratios from **Table 3.6.3** provide evidence for this statement. The modified sediment transport ratios were the result of considering the increased flow density with the high amount of suspended sediment that we observed during our experiments. These values demonstrated that roughly half of the sediment that entered the flume was deposited along the topset whereas the remaining half was transported to the edge of the topset. These modified ratios are better suited to our results with more sediment arriving at the foreset which allowed the foreset to aggrade at a faster rate than the topset.

Through performing a grain size analysis on our core samples from both experiments, we uncovered numerous trends and behaviors relating to sorting and

deposition, including: (1) variability in our grain size distributions, (2) downstream fining in the bottomset, (3) more fines found in our deposits downstream, and (4) the largest average grain sizes in the middle sections of our deposits. Since we were unable to completely remove the effect of the grain size distribution variability, we averaged our grain size distributions to account for this. Our grain size analysis provided evidence for a downstream fining trend in the bottomset that was formed as the result of gravity depositing larger particles farther upstream. This behavior resulted in more fines being detected downstream. The foreset sediment which covered the bottomset was located in the middle of the deposit and was found to contain the largest grains due to the avalanching foreset consisting primarily of large particles.

Although we included a mixture that incorporated very fine grains, the deposits formed during our experiments still appeared to develop similarly to those reviewed in Kleinhans (2005). Many of the phenomena that Kleinhans observed were also witnessed during the generation of our deposits. Like Kleinhans, we saw the topset, foreset, and bottomset regions gradually take shape as the sediment and fluid mixture was introduced into the flume. At the upper slope of the foreset, we found a collection of large grains that eventually flowed down the foreset surface and performed kinetic sieving. Kleinhans also observed the sediment travelling down the foreset slope and defined this action as grainflow. After examining his core samples, Kleinhans found results that matched an upward fining trend, apart from the bottommost layer. Kleinhans ascribed this discovery to the mixing of previously settled fines with coarse sediment from the bottom of the foreset. We also uncovered a similar reversal in height-dependent segregation, however, we attributed our results primarily to the settling of suspended sediment that occurred before the foreset advanced horizontally over the bottomset. It is important to note that we incorporated a complex grain size distribution with a portion of fine clay particles that Kleinhans did not include in any of his mixtures. Nevertheless, we still found many similarities between the results of our experiments and those conducted by Kleinhans.

In conclusion, we found that altering the inflow rate of the coal and clay surrogate mixture into the flume notably affected the deposition and transport of sediment. We

were also able to provide verification that doubling the inflow rate revealed some distinct segregation behaviors. We found our study of prograding Gilbert deltas supported previous results presented in Kleinhans (2005). Unlike Kleinhans, we included a portion of finer particles with much smaller settling velocities that gave rise to the unique results in our findings. Through examining the core samples from both of our experiments, we found evidence for grain size variability, downstream fining, a unique vertical trend, and the retention of finer grains on the topset.

A major motivation for this work was to uncover information that would be useful to the oil sands industry with the reclamation of their tailings ponds. One of the biggest concerns with the tailings pond reclamation process is the extensive amount of time required for the settling of fine grains in the ponds. One way to combat this issue would be to keep as many fines as possible from reaching the pond or to capture them along the beach or topset. With our research, we found a slight increase in the amount of finer grains retained in the topset when our inflow rate was lowered. The oil sands industry could incorporate a technique such as this by discharging their tailings into the ponds at a decreased rate. This could also be interpreted as discharging tailings materials at a lower and continuous rate versus intermittent periods of higher discharge.

Chapter 4 - Experiments with Coal, Clay, and Sand Mixture

4.1 Description of Mixture

The coal and clay surrogate mixture used in Chapter 3 was a mixture that we believed to be very similar to the TSRU tailings we received. For the set of studies described in this chapter, we used a similar mixture as previous, however, we replaced half of the coal with silica sand. Part of our reasoning for incorporating sand in the mixture was the importance of this component in actual tailings. Depending on the deposit quality, source, and extraction process, oil sands tailings contain approximately 70 to 80 wt% water, 20 to 30 wt% solids (i.e., sand, clay, and silt), and 1 to 3 wt% bitumen (Allen. 2008). The oil sands industry constitutes the sand and silt transitional grain size to be 44 microns (Beier et al., 2013; Hande, 2014). Due to the presence of sand in the tailings, we incorporated silica sand into our surrogate mixture. At the same time, we realized that adding this key component of TSRU tailings to our own surrogate mixture might bring about some interesting and important physical behaviors. Although silica sand is smaller in size than anthracite coal, it has a higher density. We believe that this characteristic could enhance the segregation behavior present in our surrogate mixture. In the end, understanding the physics behind these behaviors may help guide the oil sand industry in improving settling processes in scenarios other than tailings ponds.

4.1.1 Determination of Surrogate Sediment Mixture

The actual amounts of coal, clay, and sand used in experiments A05 and A06 were included in **Table 2.5.3**. Due to the success with previous experiments, we did not want to greatly alter our surrogate composition. Therefore, the mixtures used for experiments A05 and A06 had the same % sediment by volume as experiments A02 and A03, however, 50% of the coal was replaced by silica sand.

4.1.2 Time Dependent Pictures and Observations

We conducted settling column experiments on our new surrogate mixture of coal, clay, and sand similarly to section **3.1.2**. The surfaces of the initially settled, coarse layer for both the TSRU tailings sample and the coal, clay, and sand mixture were tracked in videos as seen in **Figure 4.1.1**.

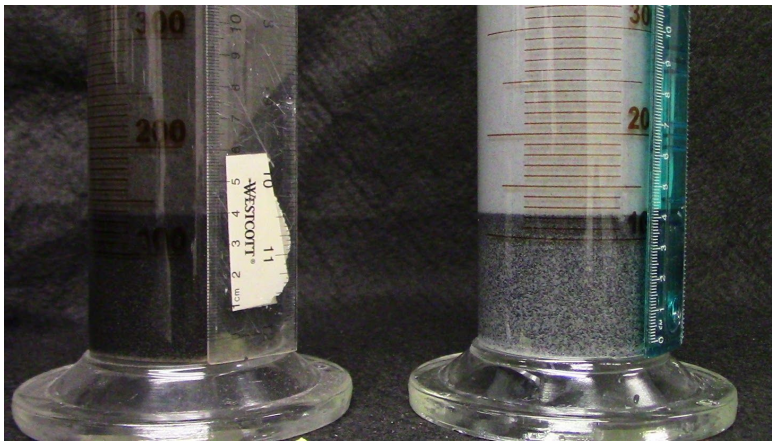

(a)

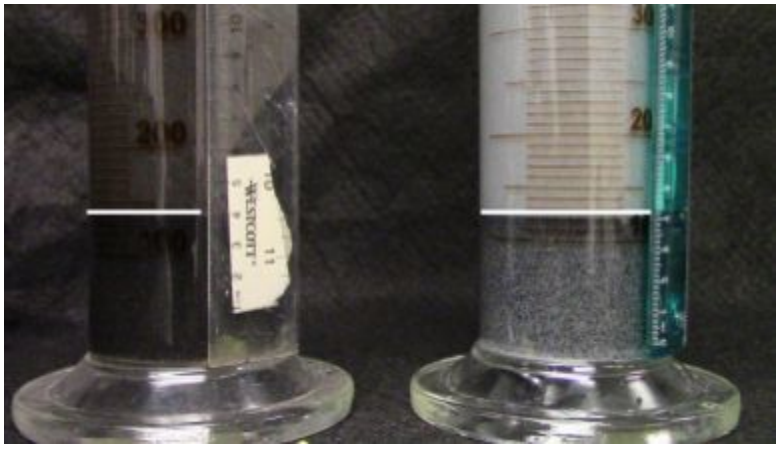

(b)

Figure 4.1.1: **(a)** Screenshot of video from settling column experiment with TSRU tailings on the left and the coal, clay, and sand mixture on the right. **(b)** The same image with white lines to indicate the surface of the settled coarse layer. Rulers were attached to the sides of the columns to provide scales.

Both of the columns were mixed simultaneously and the timer was started as soon as the columns were both placed in front of the camera. By using the rulers, the locations of the interfaces for both columns were recorded at various times. The data recorded from tracking the interface of the coarse layer is documented in **Figure 4.1.2**.

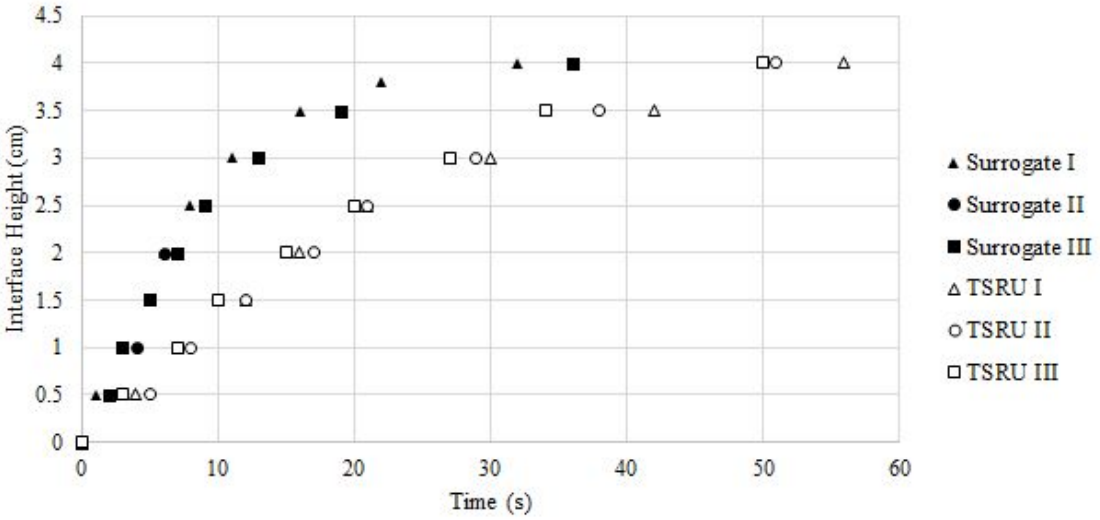

Figure 4.1.2: Results from tracking the surface of the initially settled coarse layer of particles in both the TSRU tailings samples and the coal, clay, and silica surrogate mixture. There were three videos recording the settling of the surrogate mixture and three videos for the settling of the TSRU tailings.

A numerical derivative was performed on the location and time data so as to calculate the settling velocities of the interfaces for both samples and is included in **Figure 4.1.3**.

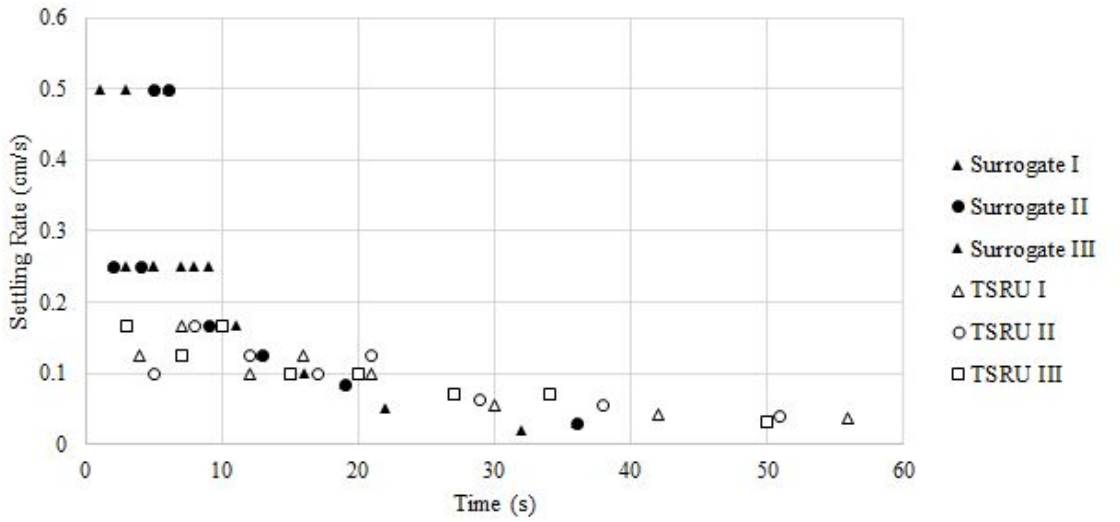

Figure 4.1.3: Plot of calculated settling velocities of the surface of the settled coarse particle layer inside of the settling columns for both the TSRU tailings sample and the coal, clay, and silica surrogate mixture. There were three videos recording the settling of the surrogate mixture and three videos for the settling of the TSRU tailings.

Over the same amount of time, the settling velocities for the TSRU tailings sample ranged between 0.031 and 0.167 cm/s and between 0.02 and 0.5 cm/s for the surrogate mixture consisting of coal, clay, and sand.

4.1.3 Laser Diffraction and Microscope Results

We placed samples of dampened silica sand into the Horiba as described in detail in **2.8.2 Grain Size Analysis Procedure**. For the purpose of reducing the effect of settling inside of the sample bottle, the silica sand was wetted. A total of four grain size distributions were returned by the Horiba for the silica sand samples and the average relative frequency for the four plots can be seen in **Figure 4.1.4**. The reason for calculating the average relative frequency is explained in detail in **4.5.1 Grain Size Distribution Variability**.

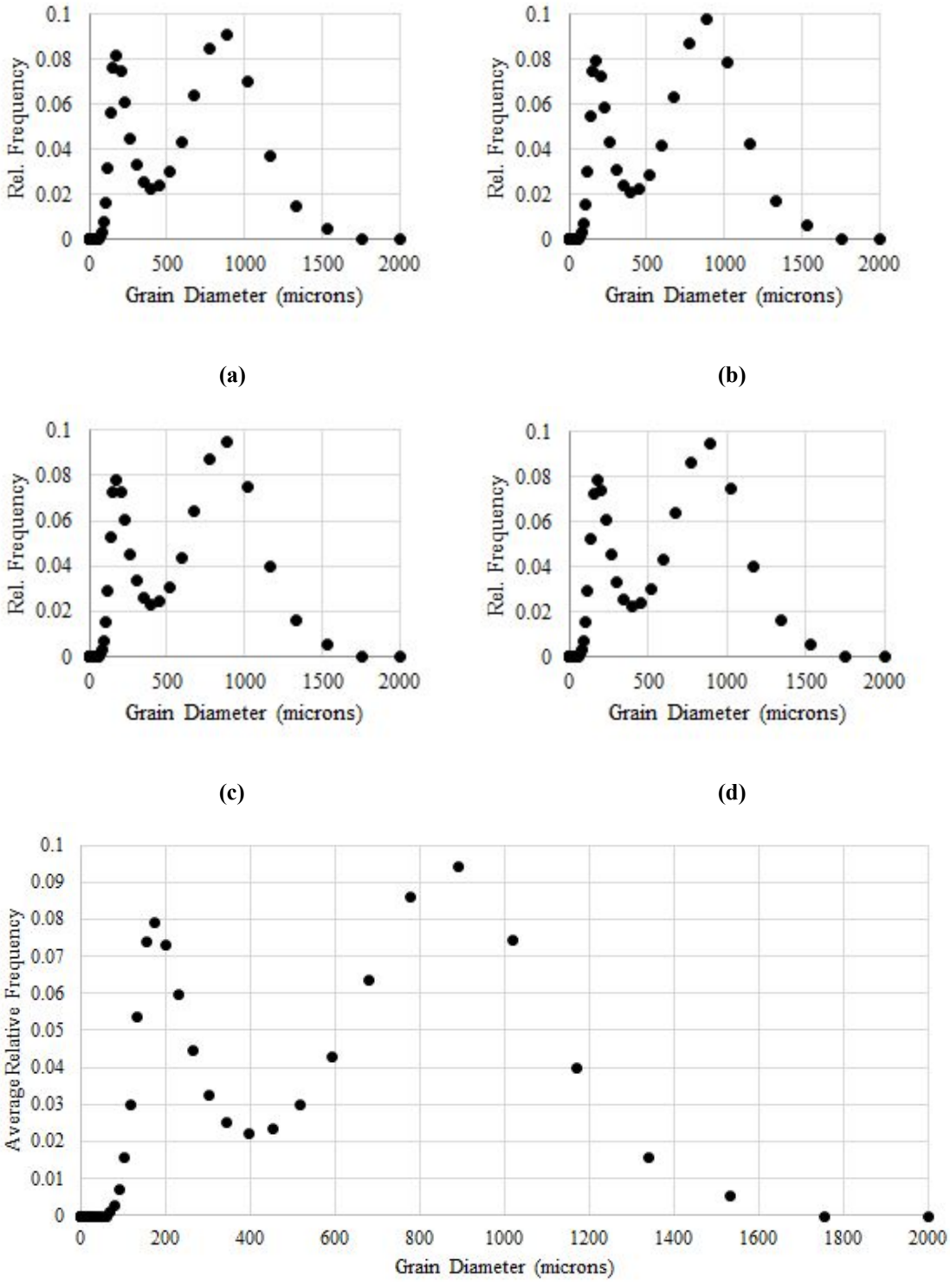

Figure 4.1.4: **(a)-(d)** Relative frequency plots for four silica sand samples. **(e)** The average relative frequency plot for the four plots for silica sand.

Microscopic images were taken of a sample of silica sand in order to better understand the shape and grain size variation of the sand. A sample of these pictures is included in **Figure 4.1.5**. The images shown in **Figure 4.1.5** were taken with a Leica Wild M10 microscope. The bar in the top left corner of the images provides a scale of 2 mm.

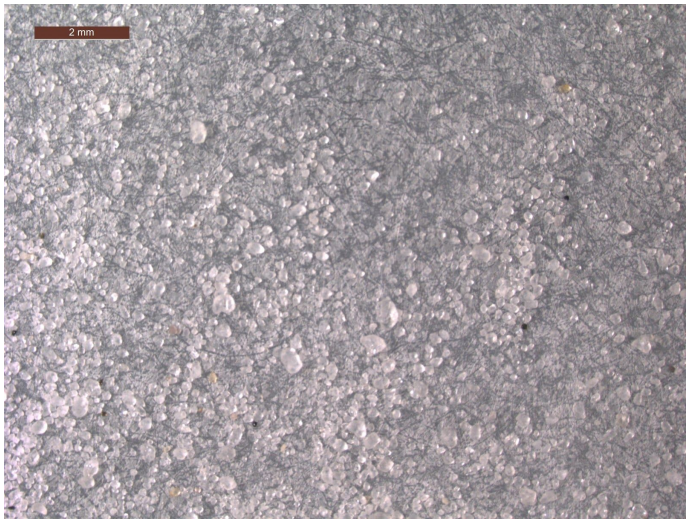

Figure 4.1.5: Image taken with a Leica Wild M10 microscope of silica sand. The scale in the top left corner is 2 mm.

This image taken with the microscope shows the spherical shape of the silica sand particles. We can also see two very different grain sizes present in this image that would explain the bimodality of the grain size distribution.

4.2 Observations of Experimental Depositional Formation

Similar to the experiments conducted in **Chapter 3**, we tested our new mixture at two different discharge rates: 1.0 L/s for experiment A05 and 0.5 L/s for experiment A06. Altering the inflow rate is a relatively attainable adjustment that can be made by the oil sands producers. We varied the discharge for the purpose of determining if altering the

inflow rate had any significant effect on the segregation and depositional behaviors exhibited by the new, more complex mixture.

The deposit formation processes observed in experiments A05 and A06 were divided into three main stages. The first phase was when the materials first entered the flume and began to build up the deposit. The second stage, also called the "steady state" stage, occurred when the profile of the deposit did not change with time, the front merely progressed downstream. The last phase included any additional formation of the deposit after pumping had stopped.

4.2.1 Early Stage

We first ponded the flume by filling it with water until the level reached the top of the downstream weir. The materials entered the flume at the inlet and first traveled over the upstream weir before entering the main section of the flume and mixing with the pond water. The mixture traveled in the form of a plume in hypopycnal flow, as seen in **Figure 4.2.1**, down the entire length of the flume.

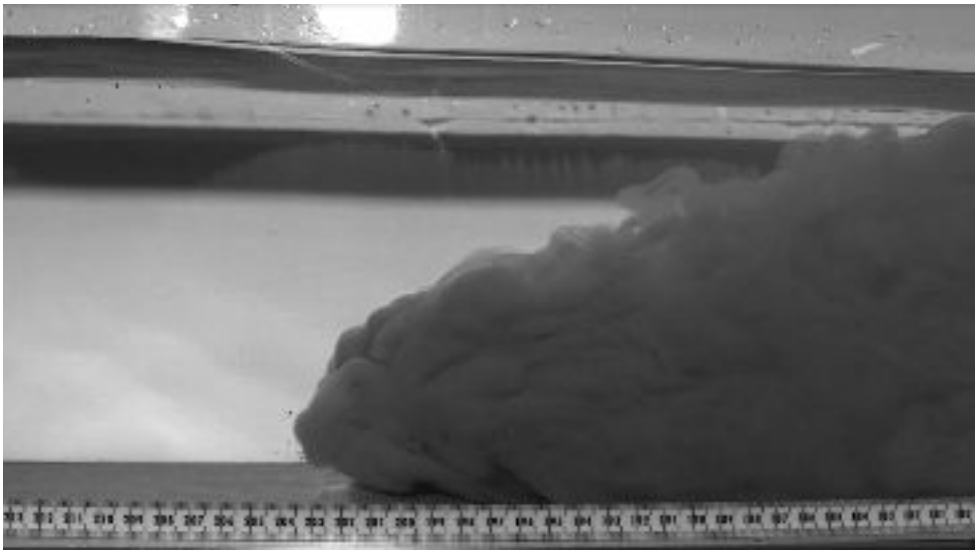

Figure 4.2.1: Screenshot from video from experiment A05 with the mixture in the form of a plume proceeding down the length of the flume. The plume traveled from right to left in the flume.

The particles left behind by the plume were allowed to settle and form the bottommost layer of the deposit, as seen in **Figure 4.2.2**.

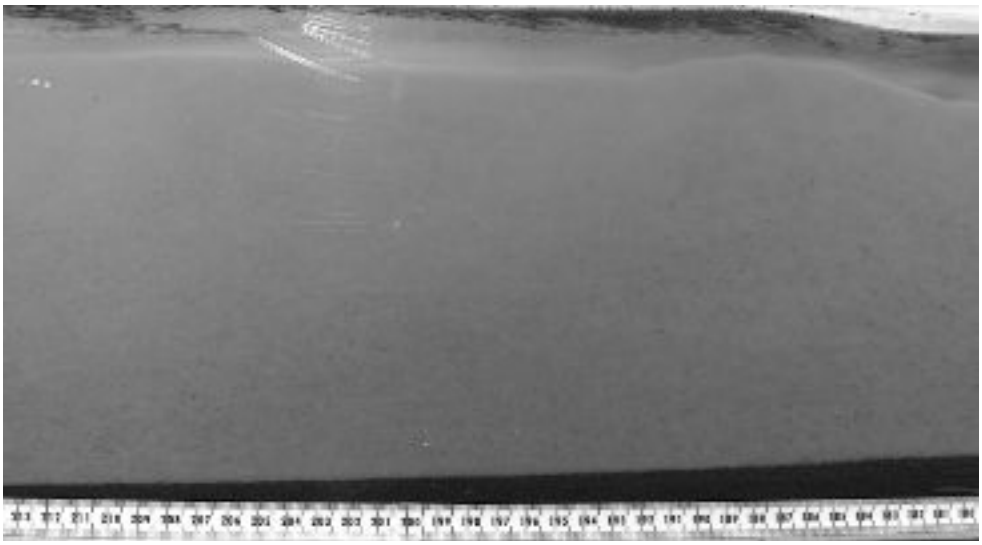

Figure 4.2.2: Snapshot from a video from experiment A05 after the plume advanced through this section of the flume. The large particles carried by the plume gradually settle and form a thin layer of the deposit.

At this time, there was little disturbance in the fluid so the large particles were able to settle and form a thin layer relative to the depth of the pond. Also during this time, newly introduced particles were beginning to form a triangular wedge at the downstream edge of the upstream weir. Once the top of the wedge reached the surface of the water in the flume, it leveled off and took the shape of a Gilbert-style delta as seen in **Figure 4.2.3**.

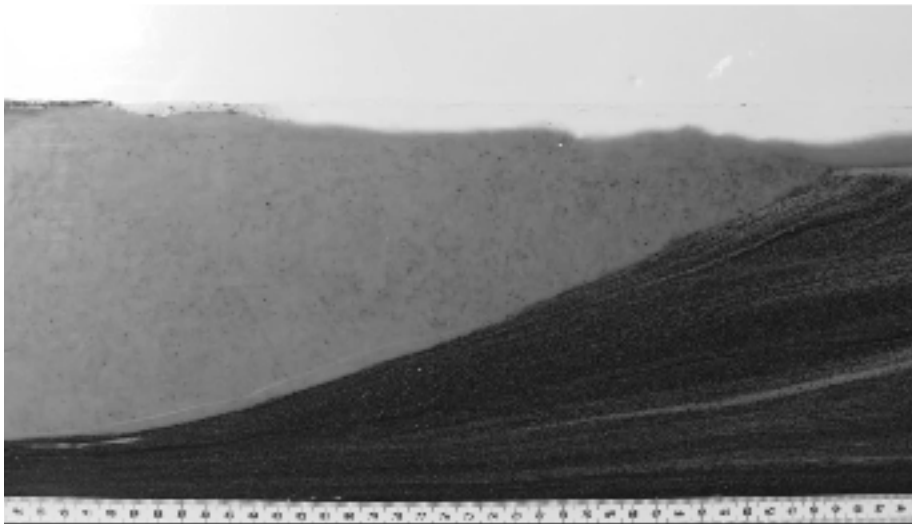

Figure 4.2.3: Screenshot from a video recording of experiment A06 at an upstream location where the deposit had the form of a Gilbert delta and traveled from right to left.

As the fast-traveling stream skimmed over the flat top of the pre-existing topset, it carried with it a fair amount of particles in suspension and bedload while occasionally depositing some particles. At the edge of the topset, the largest particles amassed at the upper slope of the foreset that intermittently avalanched down the foreset in hyperpycnal flow. The process of deposition, build-up, and failure continued and resulted in the downstream progression of the front of the deposit. These avalanches gradually covered the previously settled layer of the particles along the bottomset. The particles that did not collect at the upper edge of the foreset traveled in homopycnal flow and settled relatively slowly along the foreset and bottomset compared to the rate of the stream. After 3 to 5 minutes had passed, the geometries of the topset, foreset, and bottomset became steady i.e. they did not change with time and prograded down the length of the flume.

4.2.2 Steady State

Eventually, the profile of the front of the deposit did not vary significantly in shape with time but simply continued to travel down the length of the flume. Two images displaying this behavior are included in **Figure 4.2.4**.

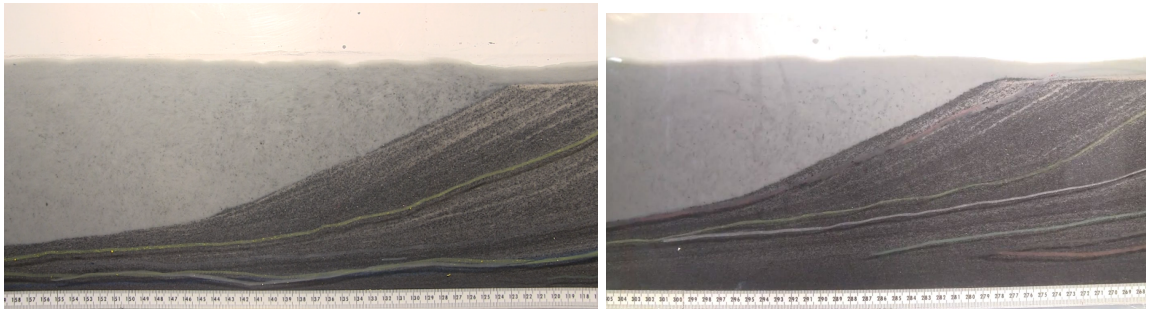

(a) **(b)**

Figure 4.2.4: Video screenshots from experiment A06 with **(a)** at an upstream location (x=118-158 cm) and **(b)** at a downstream location (x=269-305 cm). The shape of the front in both images did not vary greatly in shape even after the deposit had advanced over 100 cm.

While in steady state, particles continued to collect at the upper end of the foreset and the avalanche down the slope of the foreset while the topset aggraded at a much slower rate.

4.2.3 After Pumping Ceased

Eventually, the level of mixed materials inside of the mixing tank reached a level that the mixer could no longer reach and pumping ceased. With no new material being added to the flume, the stream traveling over the topset stopped and the materials inside of the flume began to calm and settle. The section of the flume not reached by the advancing foreset was primarily filled with clouded pond water. As the water stilled, the suspended particles in the pond began to settle and form a thin layer, relative to the depth of the pond, of fine particles as shown in **Figure 4.2.5**.

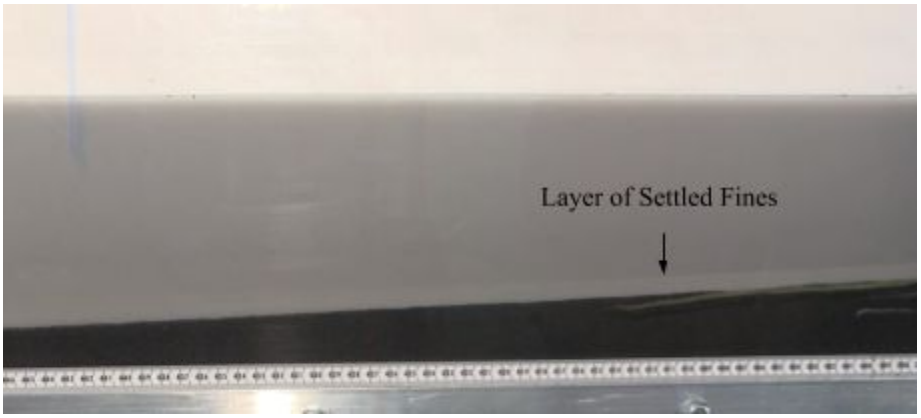

Figure 4.2.5: Screenshot taken of video captured during experiment A06 with a thin layer of fine particles settling over the bottomset left by the plume.

4.3 Measurements of Profiles

We recorded the profiles of the deposits formed during experiments A05 and A06 in order to visualize the vertical and horizontal progressions of the deposits. Throughout this section we present data and plots relating to deposit profiles in **4.3.1** and final deposit slopes in **4.3.2**. A more detailed analysis and discussion on this information is later covered in section **4.6** for experiments A05 and A06.

4.3.1 Plots of Profiles

At roughly 1-2 minute intervals, we drew the surface deposit lines for both A05 and A06 on the side wall of the flume as explained in detail in **2.7.2 Surface Lines**. After the experiment had finished, we measured the lines drawn on the side of the flume with a ruler and recorded this in **Figure 4.3.1**.

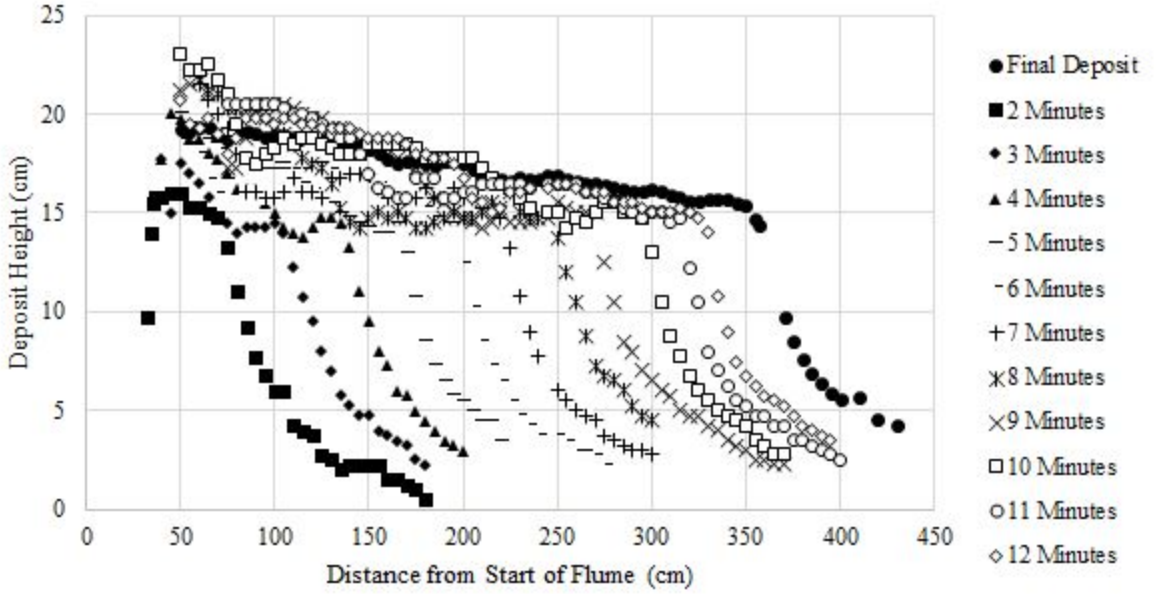

(a)

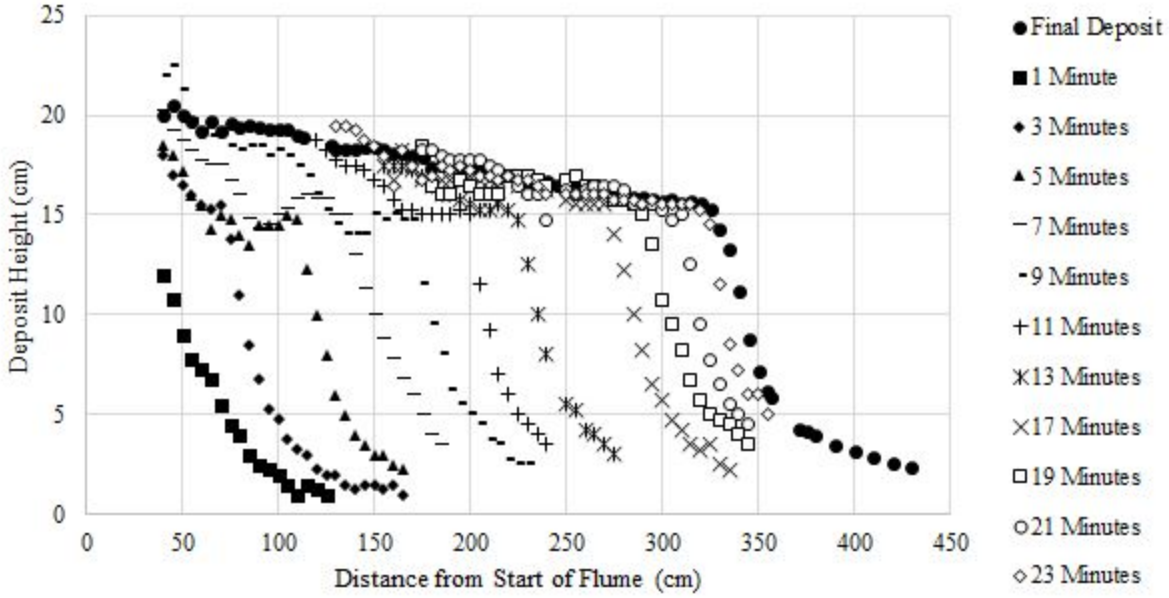

(b)

Figure 4.3.1: Plots of bed surface profiles taken at assorted times and the final deposit for experiments **(a)** A05 and **(b)** A06. Some of the bed surface profile data for A05 and A06 is incomplete due to the front progressing too far before the lines were finished. Anticipating future discussion starting in section **4.6.1**, we here define the topset and foreset aggradation rates and velocities. The aggradation rates for both the topset and foreset refer to the change in area beneath each surface divided by the time between two profiles.

The topset and foreset velocities refer to the distance between two profiles divided by the time passing between the two measurements.

The plots shown in **Figure 4.3.1** show the vertical and horizontal progression as more coal, clay, silica sand, and water were pumped into the flume. Similar to experiments A02 and A03, the horizontal velocity of the deposit exceeded the movement in the vertical direction. Section **4.6.1** provides more analysis on this behavior of the deposit.

4.3.2 Final Topset, Foreset, and Bottomset Slope Values

Figure 4.3.2 displays the final deposits for both A05 and A06. These values were measured with a point gauge that was attached to the top of the flume.

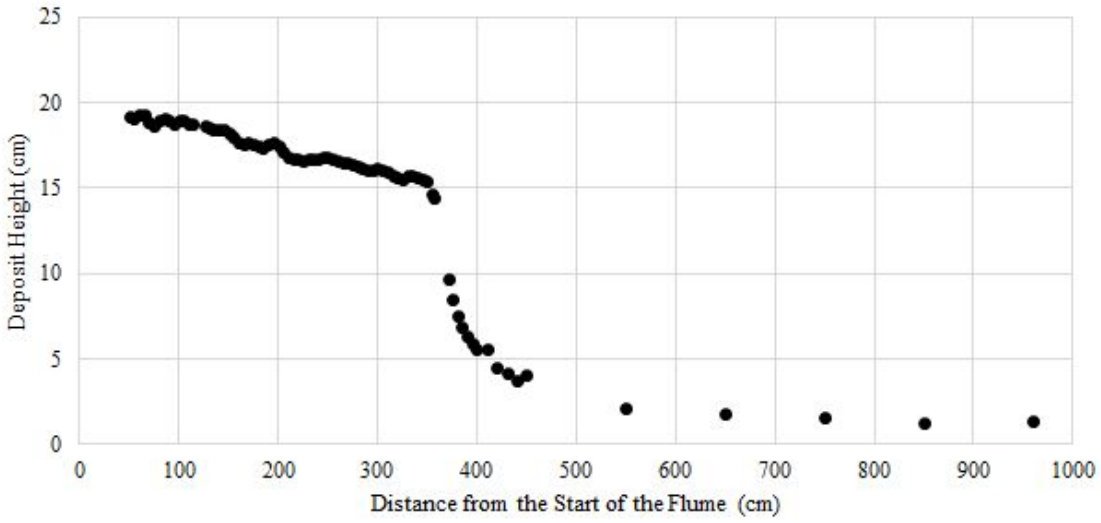

(a)

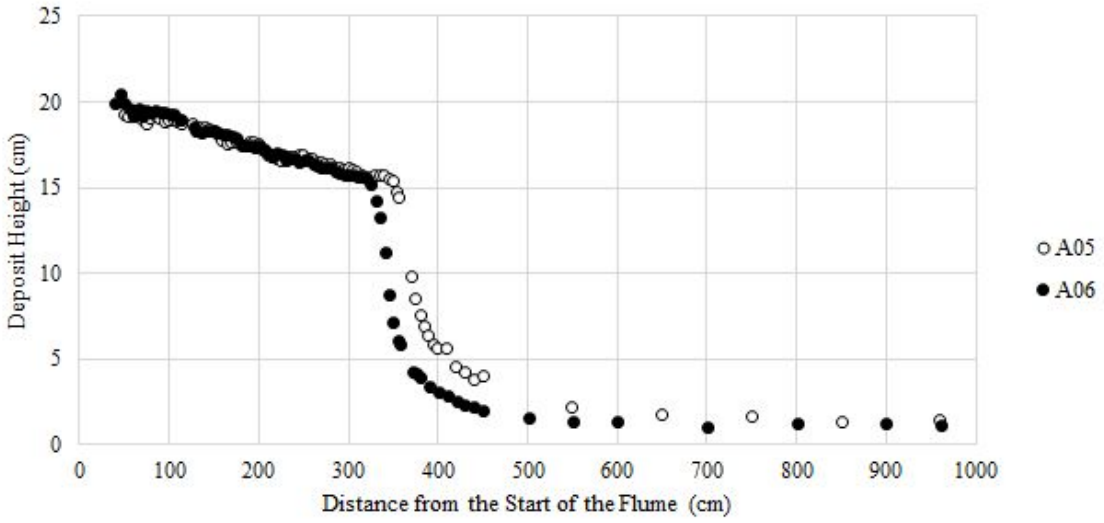

(b)

Figure 4.3.2: Final deposits recorded for experiments **(a)** A05 and **(b)** A05 and A06 together. The values were measured by a point gauge attached to the top of the flume. There are occasional gaps in the data due to the point gauge not being able to take values at the locations of the aluminum supports.

In order to retrieve the slopes of the topset, foreset, and bottomset for the final deposits of A05 and A06, we fit the data points indicated in **Figure 4.3.3** to linear fits. We repeated this technique for A06. So as to collect the best results, we chose not to include data points with a lot of variability i.e. near the inlet or near the edge of the topset or edge of the bottomset.

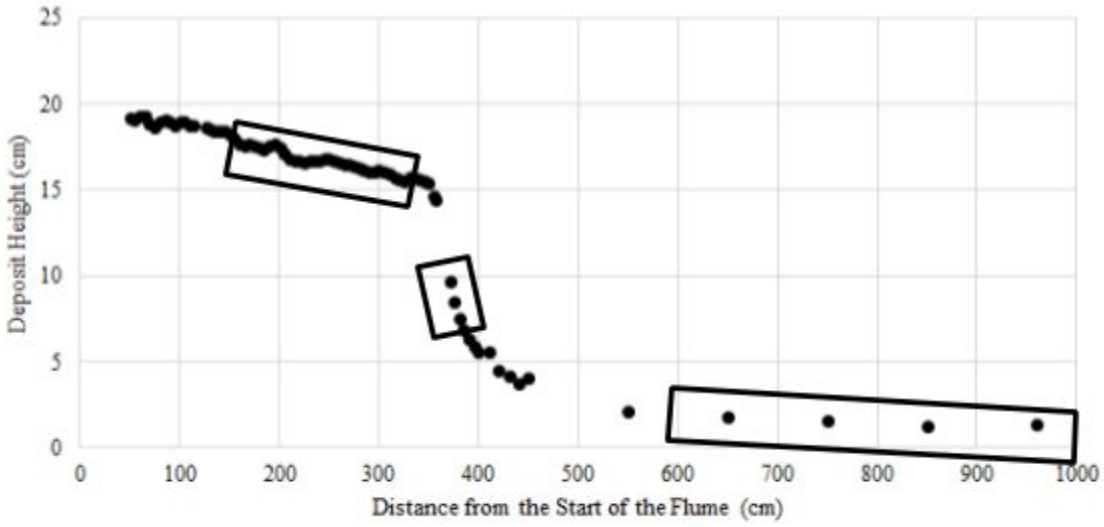

Figure 4.3.3: Final deposit for study A05 with boxes to indicate the regions of data used to determine the topset, foreset, and bottomset slopes.

The final slope values for the topset, foreset, and bottomset for A05 and A06 are reported in **Table 4.3.1**.

Experiment #	Discharge (L/s)	Topset Final Slope	Foreset Final Slope	Bottomset Final Slope
A05	1.0	-0.0135	-0.2413	-0.0024
A06	0.5	-0.0167	-0.4084	-0.0002

Table 4.3.1: Final slope values for the topset, foreset, and bottomset for experiments A05 and A06 along with discharge rates.

The bottomset final slope values for A05 and A06 were not similar, contrasting our observations from A02 and A03. However, the bottomset slopes for these experiments still exhibited similar behavior to the previous experiments; being relatively shallow compared to the slopes in other areas. The topset and foreset final slopes yielded similar flow-dependent results to that of the previous set of experiments in that the study with a smaller discharge had steeper negative slopes. In the case of the foreset, the final

slope for experiment A06, with half the discharge into the system, was almost twice as steep as what we recorded for experiment A05. Section **4.6.2** has a more extensive discussion on the final deposit slope values for the coal, clay, and silica sand experiments.

4.4 Locations of Cores

As was mentioned earlier in section **2.7.5 Coring Process**, we extracted nine cores along the length of the experimental deposits formed by studies A05 and A06 with the intent of examining the vertical and horizontal variability exhibited throughout both deposits. Starting with the deposit formed during study A05, we found the edges of the topset and bottomset as seen in **Figure 4.4.1** by first plotting the slopes for the topset, foreset, and bottomset and determining the horizontal locations where these lines intersected.

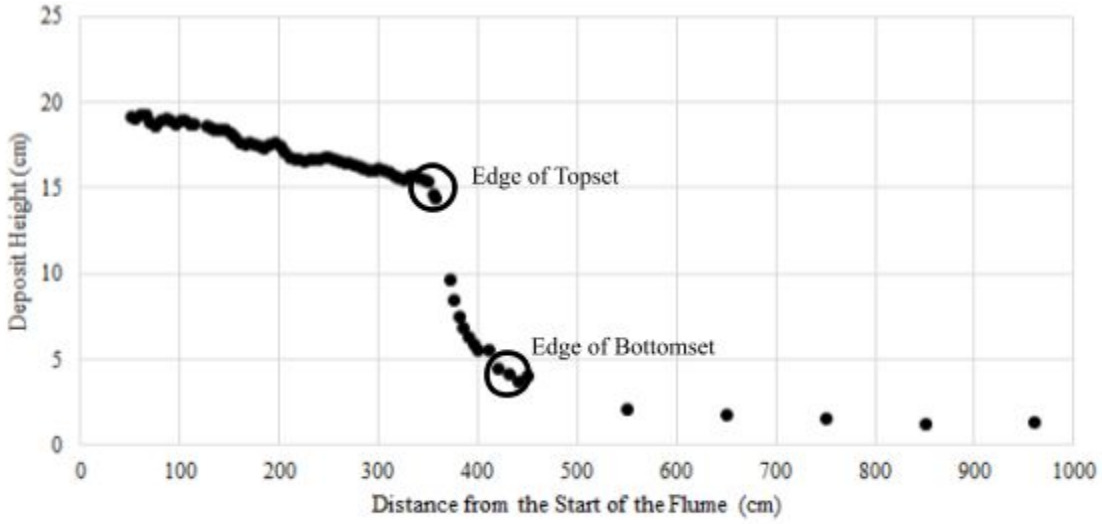

Figure 4.4.1: Plot of final deposit from A05 with circles indicating the locations of the topset and bottomset edges.

We then used the horizontal distances between the edge of the topset and the edge of the bottomset from A02 and A05 to determine the scale between the deposits. This

technique was then used to find the new coring locations for A05. These steps were repeated for the deposit formed during experiment A06. The core locations for experiments A05 and A06 are included in **Table 4.4.1**.

A05 Coring Locations (cm)	A06 Coring Locations (cm)
39	59.5
143	149
247	238
299	283
351	328
366	340.5
376	349.5
403	373
455	417.5

Table 4.4.1: Table of coring locations for experiments A05 and A06. The locations are in cm from the start of the flume.

Figure 4.4.2 and **Figure 4.4.3** display the core locations for experiments A05 and A06, respectively.

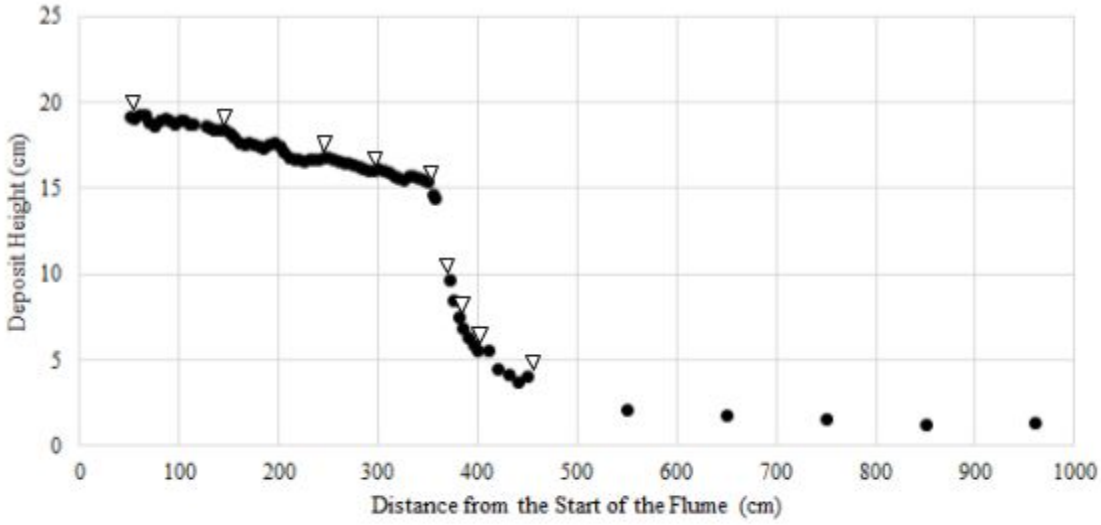

Figure 4.4.2: Final deposit for experiment A05 with triangles indicating the coring locations.

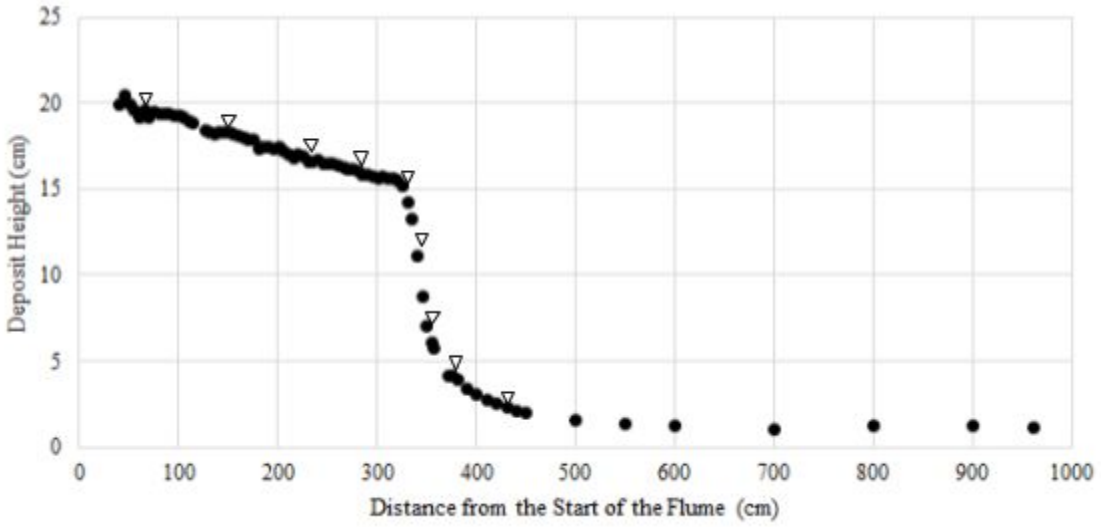

Figure 4.4.3: Final deposit for experiment A06 with triangles indicating the coring locations.

4.5 Presentation of Grain Size Analysis Results for A05 and A06

In order to observe the variability in the vertical and horizontal directions of the deposit, we averaged all of the median grain size values we received from each sample bottle and plotted these values in **Figure 4.5.1**. In addition to the median grain size

values, we include the representative uncertainties for these median values. To provide clarity, we only plotted half of the representative error bars. We generated the uncertainty values by averaging all of the standard deviations from our subsample grain size distributions obtained from the grain size analysis. We repeated this process for the bottom, middle, and top samples taken from each coring location for both A05 and A06.

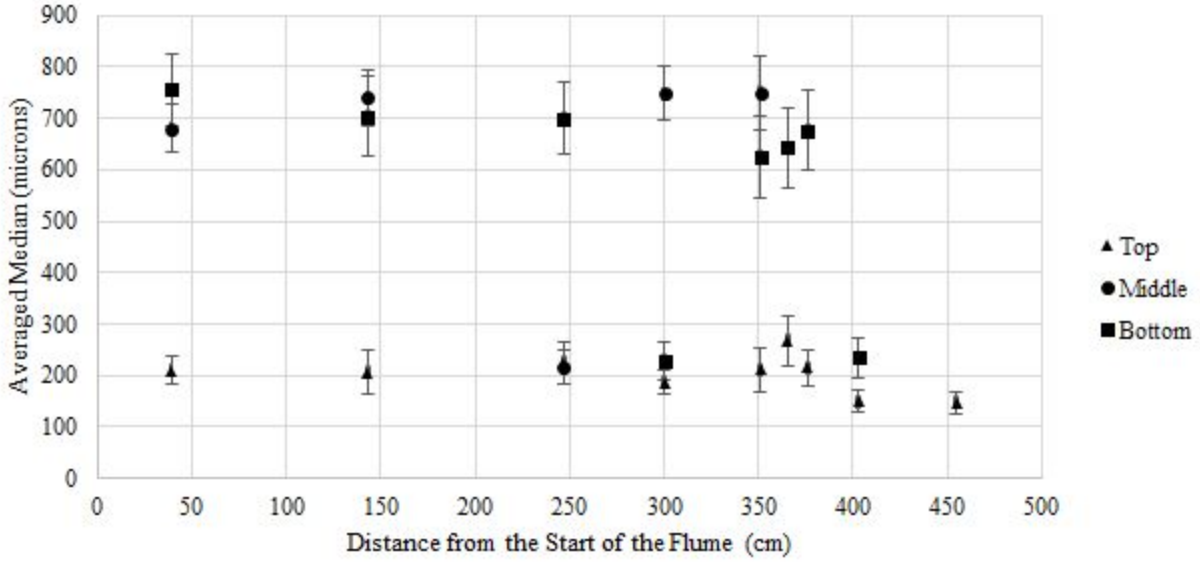

(a)

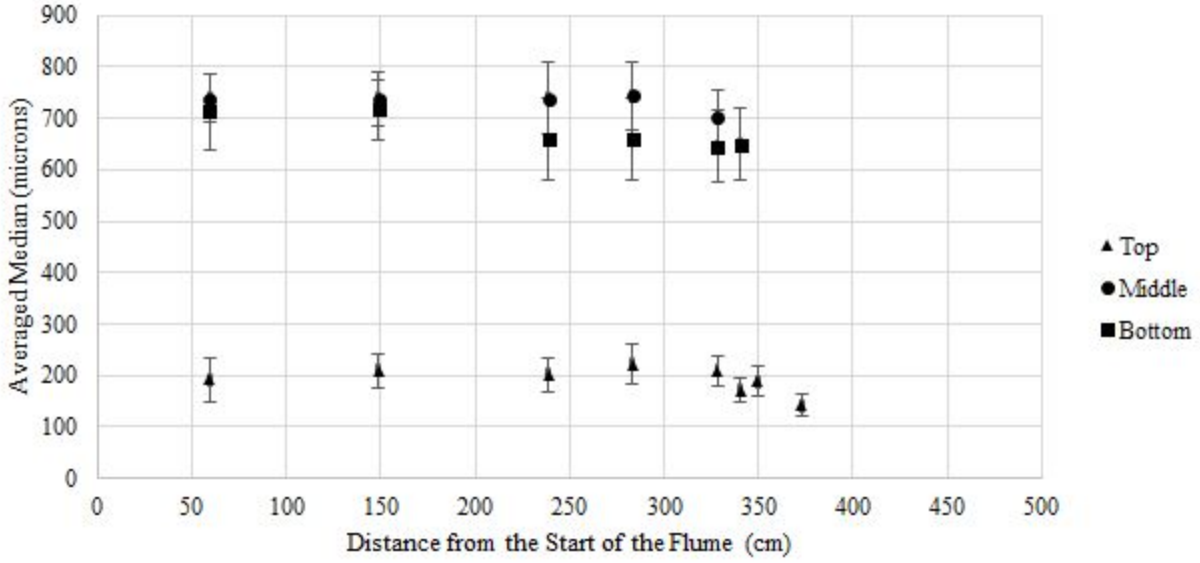

(b)

Figure 4.5.1: Averaged median grain sizes with representative uncertainties for the top, middle, and bottom layers from experiments **(a)** A05 and **(b)** A06 at varying horizontal distances from the start of the flume. The averaged median grain sizes were determined by averaging all of the subsample distributions for each coring location and each layer of the deposit for both A05 and A06. The error bars were produced by averaging all of the standard deviations from each subsample grain size distribution reported by the Horiba. This was done for the top, middle, and bottom samples from each coring location for A05 and A06. For clarity reasons, we have plotts half of the representative error bars due to overlapping.

The averaged median grain sizes for studies A05 and A06 had a similar trend to the values for A02 and A03 where the averaged medians gradually decreased with distance from the start of the flume. However, the averaged median values for the top sections of both A05 and A06 were around 200 microns compared to roughly 600 microns in A02 and A03. We did notice a lot of variability in the averaged median grain sizes for A05 for some of the middle and bottom sections. This is potentially due to not enough samples being run through the Horiba. Since this method of displaying our data is potentially misleading and does not contain a lot of information, we instead looked at the actual grain size distributions to compare and analyze our data.

4.5.1 Grain Size Distribution Variability

Often, we would see completely different grain size distributions for the same samples despite all attempts to avoid this issue. An example of this complication is included in **Figure 4.5.2** as two relative frequency plots from the middle core sample taken at x=143 cm from experiment A05. **Figure 4.5.2 (a)** was the first subsample tested from the core extracted and had a median grain size of 258 microns. **Figure 4.5.2 (b)** was the fourth subsample to be tested and had a median grain size of 757 microns. These samples were both taken from the same sample after it had been mixed.

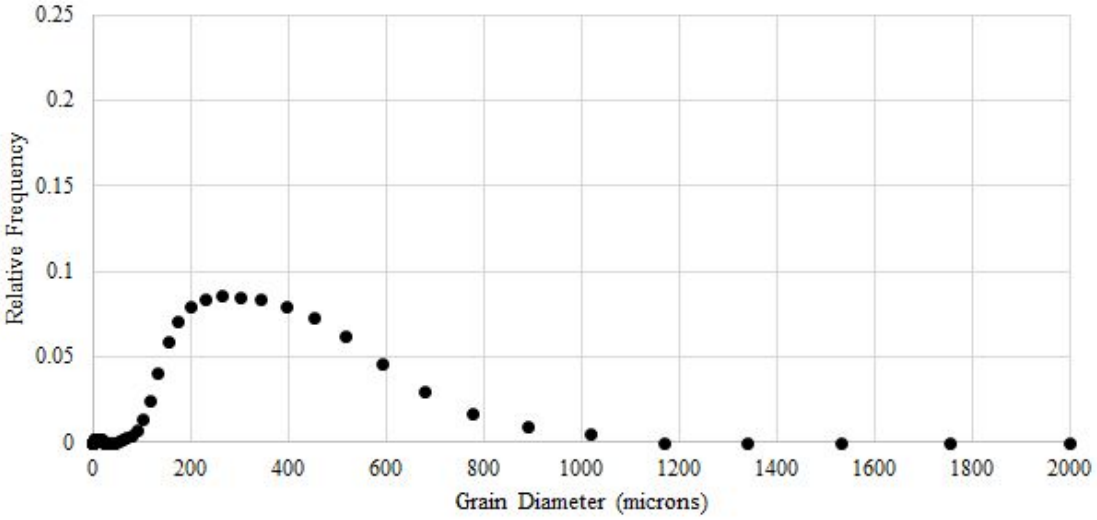

(a)

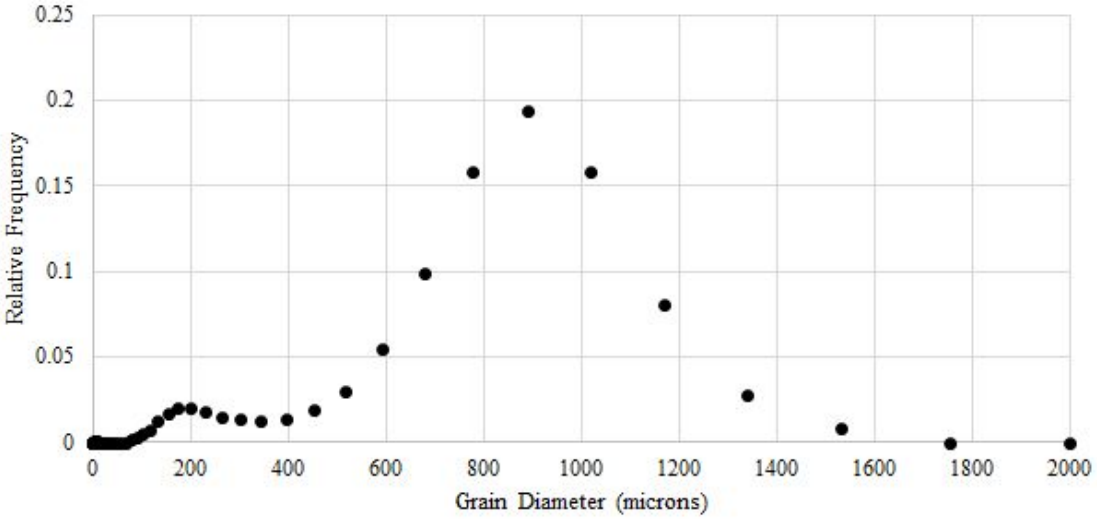

(b)

Figure 4.5.2: Relative Frequency plots from experiment A05 from the middle core samples extracted at x=143 cm from the start of the flume where **(a)** is the first distribution received from the Horiba and **(b)** is the fourth distribution. The median grain size for the first distribution shown in **(a)** was 258 microns and 757 microns for the fourth sample shown in **(b)**. These samples were both taken from the same bottle after it had been properly mixed.

We review the grain size variability matter in detail in section **5.1.3 Grain Size Analysis Sampling Complications**. To help resolve this issue, we tried to limit the

amount of settling that could occur in the sample bottles before testing the materials in the Horiba by dampening the samples. The samples were considered ready to be tested when the particles began to stick together and there wasn't any liquid that separated from the solids in the bottle. If there was visible liquid in the sample bottle, we placed the bottle in an oven until the liquid dried up. If the contents of the sample bottle were too dry i.e. not sticking to each other, we added water droplets until the materials exhibited this quality.

To account for all of the data received from the Horiba, we averaged all of the grain size distributions from each section of the deposit and coring location as shown in **Figure 4.5.3**. The plot shows the average relative frequency distribution for all of the subsamples taken from experiment A05 at location x=170 cm in the middle section of the deposit.

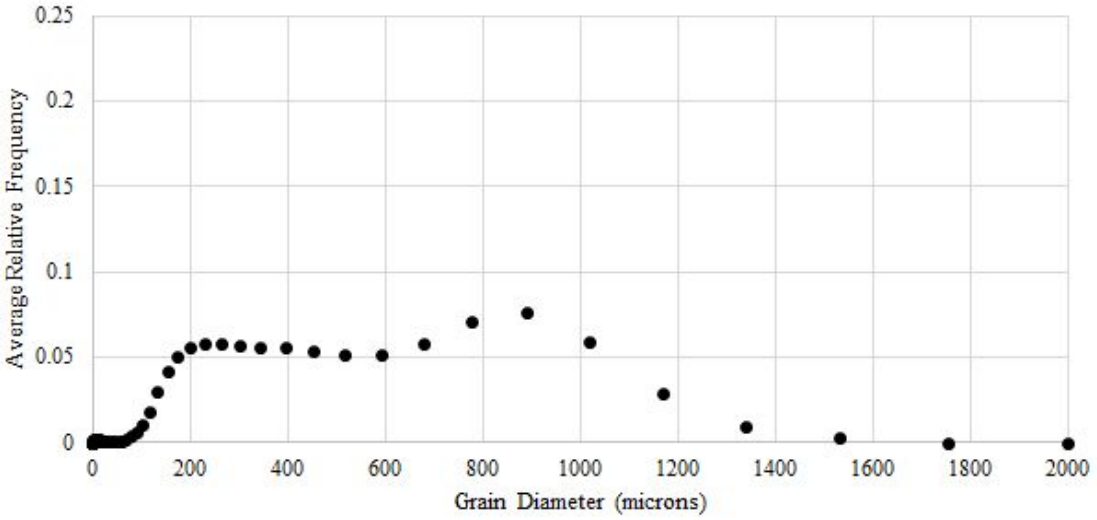

Figure 4.5.3: Average relative frequency plots for the middle section of the core sample taken from x=143 cm in A05. This average includes the two subsample distributions shown in **Figure 4.5.2 (a)** and **(b)**.

4.5.2 Downstream Trend

When examining the average relative frequency plots of the bottom of the core samples, we noticed a similar downstream fining trend in the results from A05 and A06

as we had found in A02 and A03. The average relative frequency plots for upstream and downstream locations for both A05 and A06 are shown in **Figure 4.5.4**.

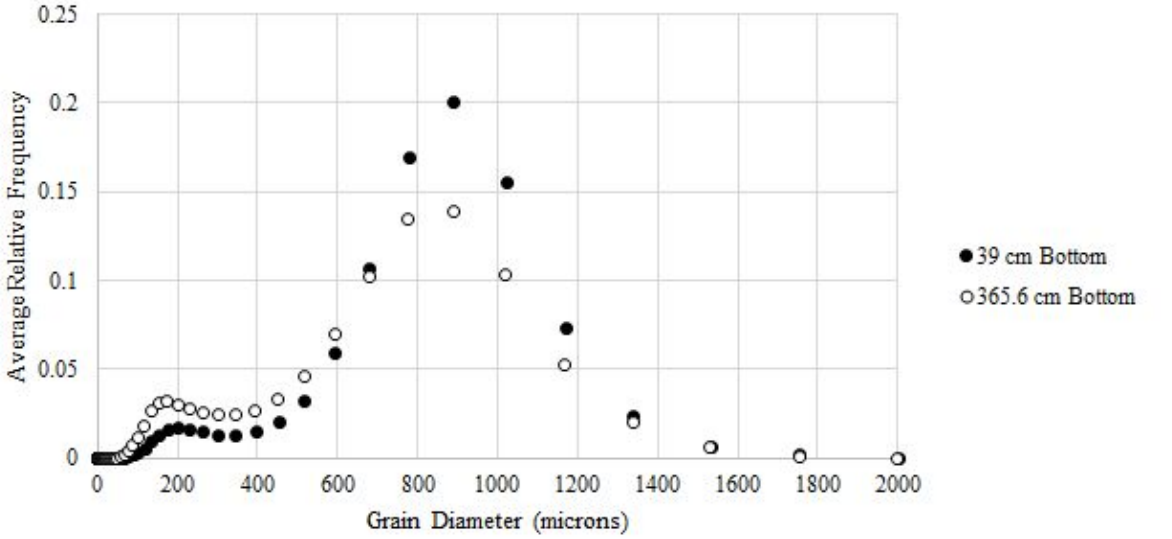

(a)

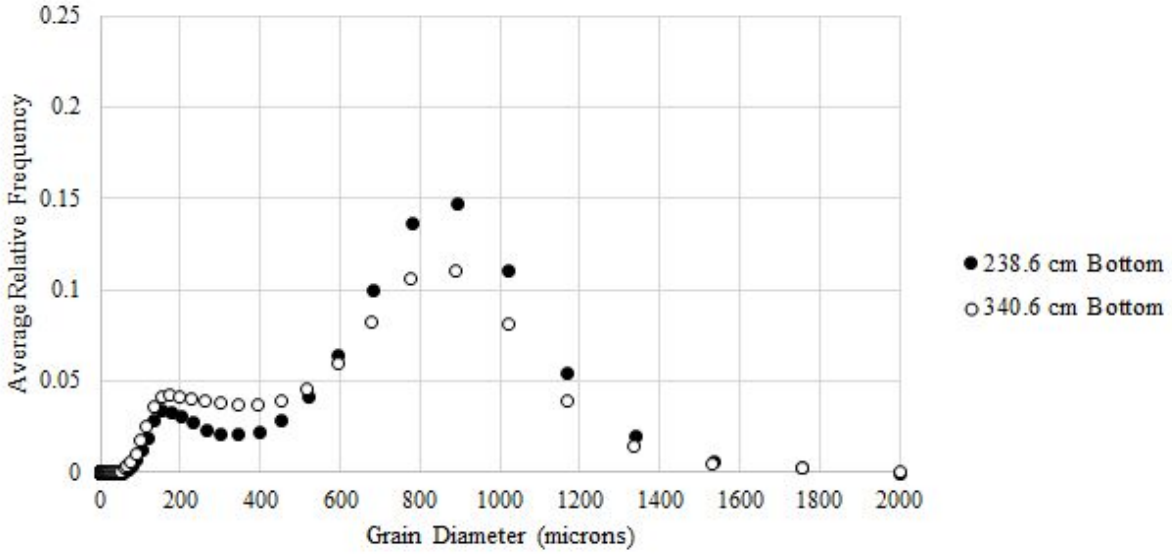

(b)

Figure 4.5.4: Average relative frequency plots for **(a)** A05 and **(b)** A06 displaying downstream fining in the bottom section of the deposits. Both plots show a decrease in the large grain size peak and an increase in the small grain size peak at distances farther from the start of the flume.

For **Figure 4.5.4 (a)**, the upstream location of 39 cm displayed a large peak near 900 microns and a much smaller peak around 200 microns. At the downstream location of 365.6 cm, the 900 micron peak was smaller and the 200 micron peak was larger than the peak from the upstream location. These observations imply that less large sized particles traveled to the downstream location and more small sized particles did. Similar observations can be noted in **Figure 4.5.4 (b)**.

Similar to the results found with experiments A02 and A03, the downstream trend was less noticeable in the results from the middle and top sections of the deposits. Again, this is presumably due to the different mechanisms present in the formation of the top and middle sections of the deposits.

4.5.3 Vertical Trend

We were able to study how the deposits differed in the vertical direction by dividing the core samples up into top, middle, and bottom sections. This information for A05 is presented in **Figure 4.5.5** at **(a)** an upstream location of 39 cm and **(b)** at a downstream location of 247 cm. By examining the grain size distributions, we noticed the bottom section had the most intense peak at 900 microns and a small secondary peak at the small grain size near 200 microns. This suggests that this section contained primarily large-grained particles with very few small-grained particles. We found that the middle section had two peaks at 200 and 900 microns, both roughly the same size meaning the middle section contained a mix of the small-and large-grained particles. The top section had the most intense peak at 200 microns, implying that this section contained predominantly small-grained particles. These results were mostly similar to the results found in previous experiments apart from the middle sections of the deposits having differing results.

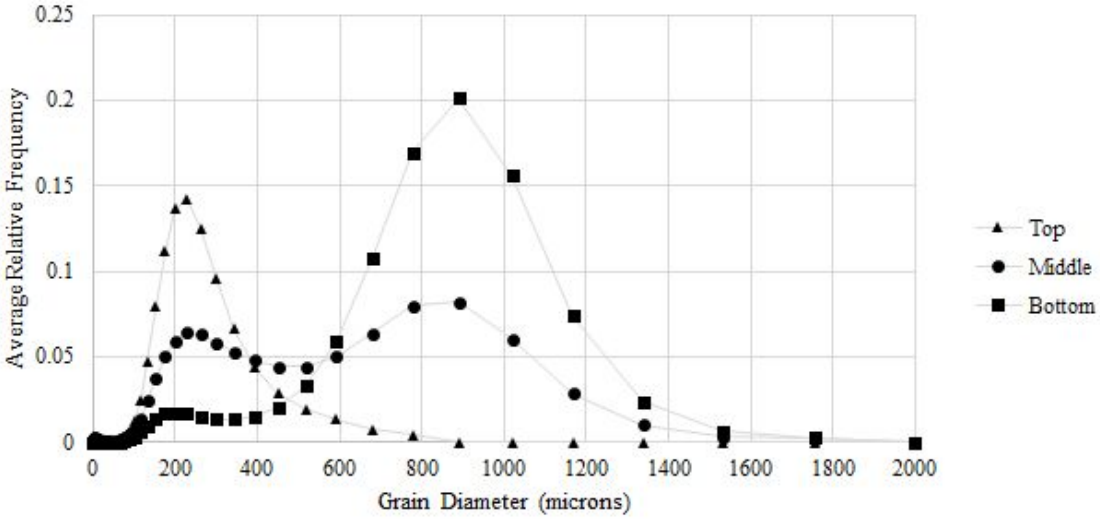

(a)

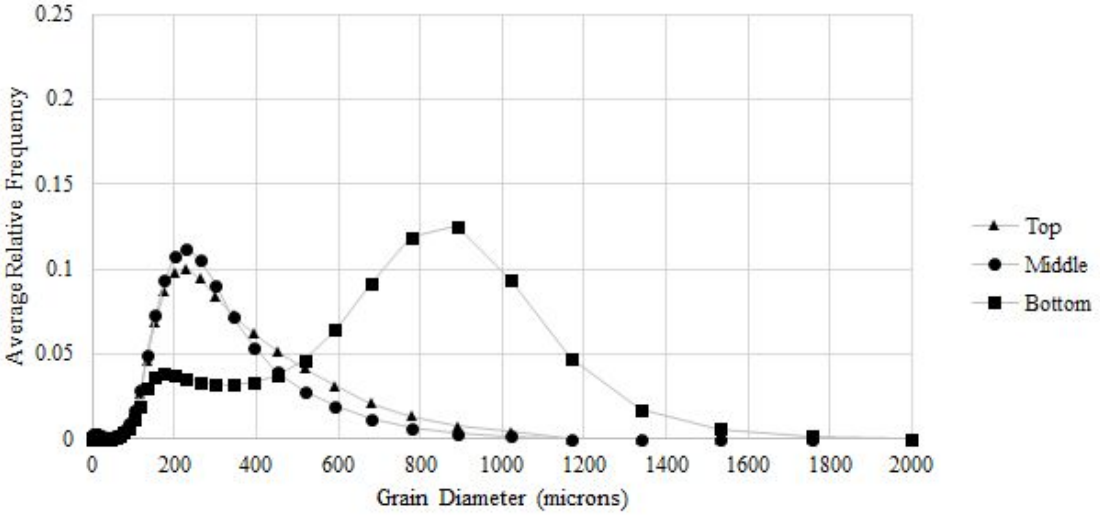

(b)

Figure 4.5.5: Average relative frequency plots the top, middle, and bottom sections of the core samples taken at **(a)** x=39 cm and **(b)** x=247 cm from the start of the flume. **(a)** represents the upstream location while **(b)** represents the downstream location. These plots show evidence supporting our vertical trend persisted at both upstream and downstream locations.

These observations were also visible in the results of the grain size analysis for core samples taken from A06 as seen in **Figure 4.5.6**.

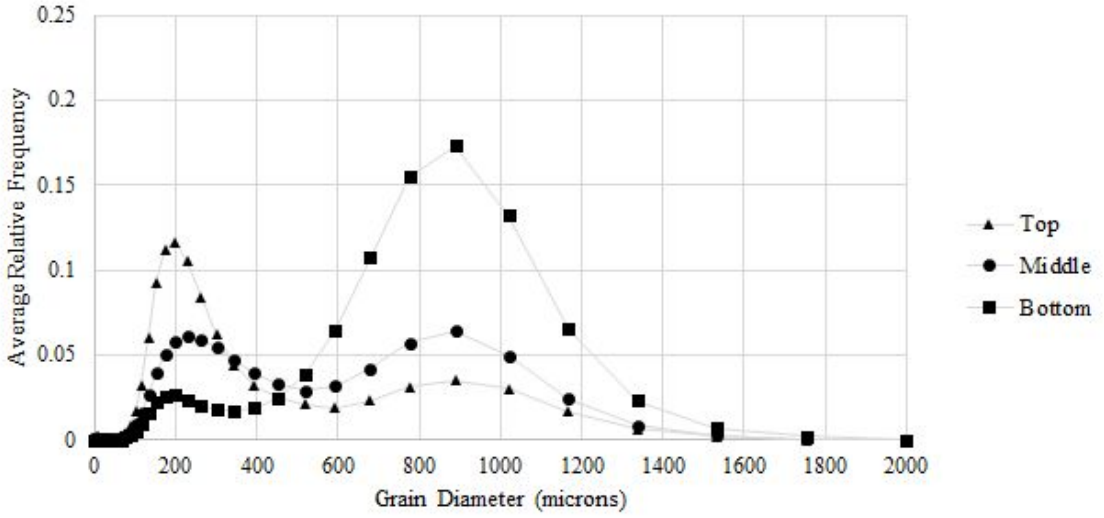

(a)

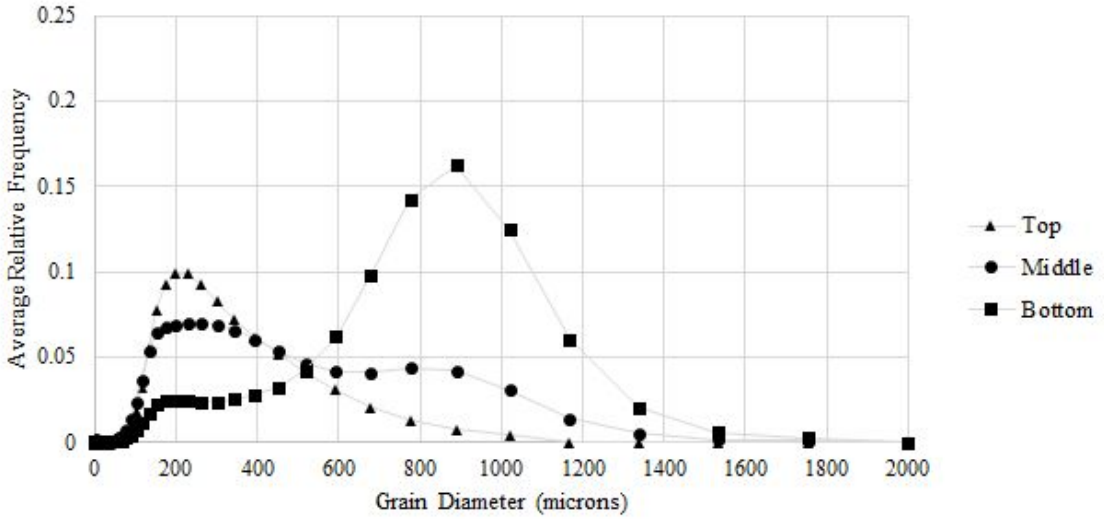

(b)

Figure 4.5.6: Average relative frequency plots the top, middle, and bottom sections of the core samples taken at **(a)** 59.5 cm and **(b)** 283.3 cm from the start of the flume. **(a)** represents the upstream location and **(b)** represents the downstream location. These plots provide evidence for our vertical trend which was discovered at both upstream and downstream locations.

4.5.4 Finer Grains Capture in Topset

We compared the average relative frequency topset plots taken at corresponding locations for experiments A05 and A06 and found A05 had a slightly higher small-grain peak. We also performed this comparison for another set of corresponding locations and uncovered the same results. We have included the plots that display this trend in **Figure 4.5.7**. The average relative frequency plots shown in **Figure 4.5.7 (a)** are from the topsets of A02 at 170 cm and A03 at 227 cm. **Figure 4.5.7 (b)** contains the average relative frequency plots from the topsets of A02 at 270 cm and A03 at 295 cm. The corresponding coring locations are shown in **Table 4.4.1**.

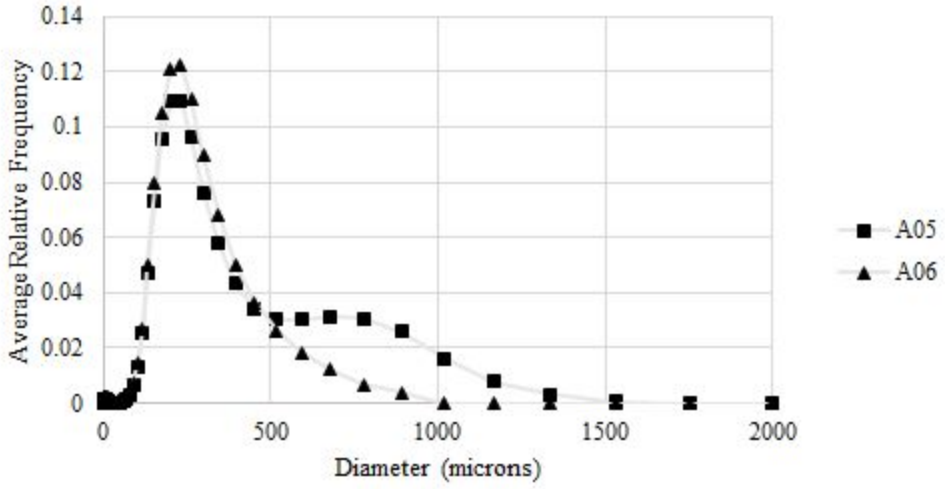

(a)

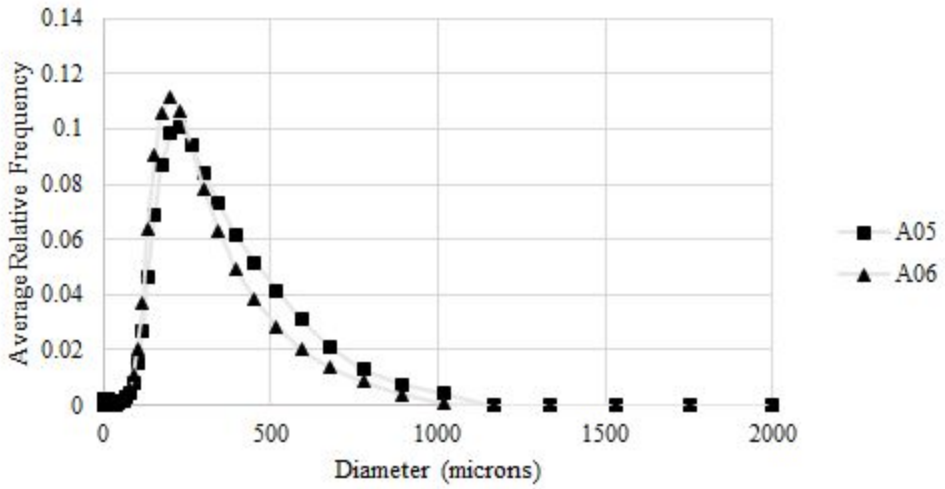

(b)

Figure 4.5.7: Average relative frequency plots for the topset for equivalent coring locations for A05 and A06. **(a)** shows the plots from the topsets of A05 at 143 cm and A06 at 149 cm. **(b)** contains the topset plots of A05 at 247 cm and A06 at 238 cm. The corresponding coring locations are shown in **Table 4.4.1**. When comparing **(a)** and **(b)**, we found A06 had slightly higher small-grain peaks in both cases. This demonstrates the increased capture of finer grains along the topset for experiment A06 which had a lower inflow rate. This observation was typical for the averaged relative frequency plots at other coring locations.

The results presented in **Figure 4.5.7** were typical for other sets of corresponding coring locations for A05 and A06. We compared **Figure 4.5.7 (a)** and **(b)** and found both topset distributions from A06 exhibited higher small-grain peaks. This trend leads us to believe that experiment A06 captured more finer particles along the topet due to it having a smaller discharge of materials into the flume. We found similar results for experiment A02. Section **4.6.5** contains a more detailed discussion on this trend. The methods used to produce these results could be implemented by the oil sands industry in their processes. We discuss this further in section **4.7**.

4.6 Analysis and Discussion of Results

In this section, we discuss the significant features we discovered in our results for experiments with anthracite coal, kaolinite clay, and silica sand. Initially, we review the trends we found in the experiments and then discuss the reasoning behind these trends. Then, we compare our findings to the Gilbert deltas studied in Kleinhans (2005).

4.6.1 Examination and Discussion of Profile Trends

The plots from section **4.3.1** confirm that the aggradation of the deposits took place primarily in the downstream direction along the surface of the foreset and not adjacent to the topset. The topset was limited in its ability to aggrade by the overwhelming inflow velocity, resulting shear forces on the sediment, and the water level

inside of the flume. We found this fact to be consistent with our observations from experiments A02 and A03.

Using the same methods as described in section **3.6.1**, we determined the average topset aggradation rates for experiments A05 and A06 and further obtained our average experimental topset velocities. The results from this work are documented in **Table 4.6.1**.

Exp. #	**Discharge, Q (L/s)**	**Average Topset Aggradation Rate, a_{top} (m^2/s)**	**Standard Deviation of a_{top} (m^2/s)**	**Average Experimental Topset Velocity, $v_{top,exp}$ (m/s)**	**Standard Deviation of $v_{top,exp}$ (m/s)**
A05	1.0	1.27×10^{-4}	3.8×10^{-5}	8.47×10^{-5}	2.53×10^{-5}
A06	0.5	6.20×10^{-5}	3.52×10^{-5}	4.51×10^{-5}	2.56×10^{-5}

Table 4.6.1: Discharge rates, average topset aggradation rates with standard deviations, and average experimental topset velocities together with standard deviations for experiments A05 and A06. The average topset aggradation rates reflect the aggradation of the topset in time. The topset velocities denote the normalization of the topset aggradation rates with the average length of the topset.

The average topset aggradation rates and average experimental topset velocities included in **Table 4.6.1** provided similar results to our findings from section **3.6.1**. We attribute these discoveries to the doubled sediment feed exhibited during experiment A05. When the flow was unable to transport the sediment, it settled along the topset and added to the aggradation in this region.

We can see from **Figure 4.3.1** that the vertical aggradation that transpired along the topset was surpassed by the aggradation along the surface of the foreset. This was partially due to the set water level inside of the flume that limited the elevation of the edge of the topset. We observed this behavior with our experiments with the coal and clay surrogate mixture as well.

Using similar methods to those presented in section **3.6.1**, we calculated the average rate at which the topset progressed perpendicular to the surface to establish the

average experimental foreset velocity. We documented these values for experiments A05 and A06 in **Table 4.6.2**.

Experiment #	**Discharge, Q (L/s)**	**Average Experimental Foreset Velocity, $v_{fore,exp}$ (m/s)**	**Standard Deviation $v_{fore,exp}$ (m/s)**
A05	1.0	4.25×10^{-3}	1.21×10^{-3}
A06	0.5	2.11×10^{-3}	9.46×10^{-4}

Figure 4.6.2: Discharge and average experimental foreset velocities with standard deviations for experiments A05 and A06. Velocity values were determined through tracking the downstream movement of the edge of the topset with time and averaging the results.

The data documented in **Table 4.6.2** revealed that the average experimental foreset velocity for the experiment with the higher discharge rate is twice that of the experiment with the lesser discharge rate. The trend exhibited by these results matches our findings from the previous chapter in section **3.6.1** and our average experimental topset velocities. With a doubled discharge rate, there would be roughly twice the amount of sediment delivered to the upper portion of the foreset, causing twice the amount of avalanches down the slope and contributing to the progression of the foreset two-fold.

With the topset aggradation limited, the constant feed of material into the flume was predominantly delivered to the front of the deposit and aggraded the foreset. When the amount of material introduced into the flume was doubled, the deposit grew at twice the rate. The trends we observed with our average experimental topset and foreset velocities were present in both our surrogate mixtures which draws the conclusion that the addition of silica sand did not alter this behavior.

4.6.2 Discussion of Final Slope Trends

We recorded in section **4.3.2** that the final topset slope value for experiment A05 was more shallow than the value recorded for A06. Although the final topset slopes do

not vary by a factor of two, they still exhibit a similar trend to the coal and clay experiments where the experiment with the lesser inflow rate had a steeper topset slope. As was mentioned previously, the slope along the topset responded by steepening to allow for the sediment and fluid mixture to continually pass through this section.

At the edge of the topset, there was a sudden drop in the deposit elevation and an increase in the bed slope and fluid depth that lowered the velocity of the flow as well as the shear stress acting on the sediment. With the shear stress reduced, gravity pulled the sediment downward where it collected at the upper slope of the foreset. The buildup of sediment avalanched down the surface of the foreset and set the slope to the dynamic angle of repose. This process continued throughout the duration of the experiments. We attribute the steeper foreset slope for experiment A06 to the lower inflow rate for that experiment. In order to account for the continuous addition of new sediment at the upper portion of the foreset, the slope steepened to keep the flow progressing steadily through this region. We noted this behavior for all of our surrogate mixture experiments.

When the flow velocity traveling downstream suddenly dropped, the sediment suspended by the flow was able to settle with more sediment collecting near the foreset. The largest suspended particles were deposited farther upstream as a result of gravity which caused the bottomset to exhibit a gradually decreasing slope that we witnessed with all of our experiments. The final bottomset slopes for experiments A05 and A06 were both very shallow, similar to our findings from the two previous experiments.

4.6.3 Discussion of Sediment Transport Trends

To better understand the transportation trends that occurred during our experiments with coal, clay, and silica sand, we performed a similar analysis to section **3.6.3**. First, we calculated the total experimental sediment transport values to establish the quantity of sediment delivered into the flume. Following that, we determined the experimental bedload transport according to Meyer-Peter and Müller (1948) and Wong and Parker (2006) and the total sediment transport as described by Engelund and Hansen

(1967). Following the same methods as before, we calculated our sediment transport ratios as well as the modified transport ratios. All of these values for experiments A05 and A06 are documented in **Table 4.6.3**.

Exp. #	Q (L/s)	Exp. Total Sediment Transport, q_{sed} (m^2/s)	MPM-WP Bedload Transport, q_{MPM-WP} (m^2/s)	EH Total Sediment Transport, q_{EH} (m^2/s)	Sediment Transport Ratio (-)	Modified EH Density (kg/m^2)	Modified EH Total Sediment Transport, q_{EHm} (m^2/s)	Modified Sediment Transport Ratio (-)
A05	1.0	5.0×10^{-4}	2.55×10^{-5}	4.32×10^{-5}	0.0864	2000	2.46×10^{-4}	0.492
A06	0.5	2.50×10^{-4}	2.26×10^{-5}	1.71×10^{-5}	0.0684	2000	9.76×10^{-5}	0.390

Table 4.6.3: Discharge rates, experimental total sediment transport values, Wong and Parker corrected Meyer-Peter and Müller bedload transport values, Engelund and Hansen total sediment transport values, sediment transport ratios, modified densities, modified Engelund and Hansen total sediment transport values, and modified sediment transport ratios for experiments A05 and A06.

The Wong and Parker corrected Meyer-Peter and Müller bedload transport values displayed in **Table 4.6.3** convey how minimal the transport was in bedload. We dismiss the bedload transport values from further analysis since these values disregard the inclusion of suspended load transport.

As was mentioned previously, we considered the approach of Naito et al. (2019) with replacing the fluid density with a combined sediment and fluid density when calculating the Engelund and Hansen total transport values. When considering this, our modified density values increased due to the sediment densities' being larger than the fluid density. The resultant modified Engelund and Hansen total sediment transport values matched the trend we saw with our previous experiments with the higher flow experiment requiring more sediment transport across the topset. For experiments A05 and A06, the transport nearly doubled when the inflow of sediment also doubled. Since the inflow of sediment and the rate of transport both increased twofold, our modified sediment transport ratios for both experiments were relatively similar in size. We noticed a similar outcome with the coal and clay experiments.

Using some of the information included in **Table 4.6.3**, we established the average theoretical topset and foreset velocities to compare with the average experimental velocities. We used the same methods mentioned in section **3.6.3** to determine the theoretical values that we have included in **Table 4.6.4** along with our previously calculated experimental values.

Exp #	**Q (L/s)**	**Average Experimental Topset Velocity, $v_{top,exp}$ (m/s)**	**Average Experimental Foreset Velocity, $v_{fore,exp}$ (m/s)**	**Average Theoretical Topset Velocity, $v_{top,theory}$ (m/s)**	**Average Theoretical Foreset Velocity, $v_{fore,theory}$ (m/s)**
A05	1.0	8.47×10^{-5}	4.25×10^{-3}	2.82×10^{-4}	2.73×10^{-3}
A06	0.5	4.51×10^{-5}	2.1×10^{-3}	1.85×10^{-4}	1.08×10^{-3}

Table 4.6.4: Average theoretical and experimental topset and foreset velocities for experiments A05 and A06 with discharge values. The theoretical values were established by dividing the accumulation of sediment by the length of the region and the solid fraction.

The average theoretical topset and foreset velocities for A05 were both double the rate of A06, similar to the average experimental velocities. We found the same trend with the coal and clay experiments as well. We expected the velocity of the topset to double when we doubled the amount of sediment being fed into the system. The doubling of the foreset velocity was also justified since the sediment transported across the topset would accumulate at the upper portion of the foreset at twice the rate, resulting in twice the aggradation in this region. All of our experimental and theoretical velocities provided evidence supporting the claim that the aggradation rate along the foreset was far greater than along the topset.

Similar to the findings from our previous experiments, our average theoretical topset velocities were larger than our experimental velocities. This would indicate that the assumptions we made with our theoretical predictions underestimated the sediment transport capacity of the flow. If this were the case, there would appear to be more sediment deposited along the topset resulting in an increased topset velocity.

Our average experimental and theoretical foreset velocities were rather similar with the theoretical values marginally underpredicting the foreset velocity. This discrepancy leads us to believe that we assumed too large of a solid fraction or overestimated the average length of the topset. Additionally, it is possible that the transport capacity of the flow was higher than our calculated total sediment transport values, as we discussed in the previous paragraph.

4.6.4 Description of Grain Size Trends

Similar to previous experiments, we discovered exceptional variability in our grain size analysis for studies A05 and A06 regardless of our attempts to diminish this effect. We were able to somewhat resolve the issue displayed in **Figure 4.5.2** by averaging all of the grain size distributions that came from the same sample bottle as shown in **Figure 4.5.3**.

We found evidence for downstream fining by examining the grain size distributions of the bottom sections of the deposits formed during experiments A05 and A06. The confirmation for this statement is displayed in **Figure 4.5.4**. These plots provide the evidence to support the claim that there were less large-grain particles at downstream locations within the flume and therefore evidence for downstream fining.

We were able to investigate the trend exhibited in the vertical direction of A05 and A06 at both upstream and downstream locations by studying **Figures 4.5.5** and **4.5.6**. The bottom sections for both experiments had the most intense peak at 900 microns and the least intense peak at 200 microns. The middle sections were found to contain a mix of large and small grain particles. The top section, on the other hand, had the most intense peak at 200 microns relative to the other plots. Since the 900 micron peak decreased while the 200 micron peak increased as a function of the vertical height of the deposit, we can say there is evidence for vertical fining.

Kinematic sorting occurred as the pile of sediment avalanched down the front of the deposit. This was seen in the form of stripes in the middle section of the deposit.

Figure 4.5.7 demonstrates how there was a higher retention of fine grains along the topset for experiment A06 which had a lower inflow of materials into the flume. This analysis was conducted by comparing the topset average relative frequency plots for corresponding deposit locations. We uncovered this trend after observing the distributions for A06 had small-grain peaks that were just higher than the small-grain peaks for A05.

4.6.5 Reasons Behind Grain Size Trends

As was noted in **Chapter 3**, we continued to experience undesirable variability in our grain size analysis results, although to a slightly lesser extent than previous. It is possible that the considerable mixing performed on the dampened samples may not have been adequate enough to break up clumps of similarly sized particles. Again, to correct for this variability, we averaged our grain size distributions at each core location.

We believe that the downstream fining trend found in the bottom layer of the deposits of experiments A05 and A06 was due to gravity which caused the larger grains to settle closer to the inlet than smaller grains. There were some particles that deposited following this trend after the initial plume progressed downstream in the flume. The plume was unable to keep the largest grains suspended so these particles were deposited closer to the start of the flume. However, the majority of the bottomset formation took place later, when particles that were suspended in the pond downstream of the topset and foreset were able to settle. These particles became suspended in the pond after being propelled past the edge of the topset. The flow in the pond was significantly less than the flow along the topset which allowed for more sediment to deposit and form the bottomset. Due to their weight, the larger particles settled closer to the topset and foreset whereas the smaller particles remained in suspension for longer and settled farther downstream. It is possible that some of the larger grains captured small grains while settling. The downstream fining trend was more evident in the bottomset since this layer

was predominantly formed through settling and not the intricate mechanisms present in the formation of other layers of the deposit.

We noticed a very clear upward fining trend in the deposit layers formed during experiments A05 and A06. For the bottom layer, we discovered a predominant large-grain peak and a more subtle small-grain peak. This formation is logical considering this layer was formed primarily as the result of particles settling. Any particles that could not remain in suspension after the flow drastically decreased began to deposit and form the bottom section of the deposit. This would cause the bottom layer to consist of large particles and some small particles that were captured during this process. In the middle section, we typically saw a mix of large and small grains which is reasonable due to the nature of the avalanching front that performs kinetic sieving and the similar layers of silica sand and coal found in this area. The results for the top section of the deposit displayed predominantly small grains with some large grains. This result is sensible owing to the avalanching front promoting upward fining and that this section contained a thin layer of settled fine particles that formed post-experiment.

The stripes visible in the middle section of the A05 and A06 deposits were likely the result of the kinematic fining as the materials avalanched down the foreset. Since the coal and silica sand had different grain sizes, they were sorted into separate layers as the smaller grains were packed into small pore spaces and the larger grains continued to travel down the slope.

Fine grains were less likely to settle along the topset when there was an increase of the inflow rate and therefore the flow velocity and bed shear stress. Due to this, more fines were transported across the topset and did not contribute to the fines retention of A05. Any fine grains not captured along the topset arrive at the pond farther downstream and settle slowly due to their lower settling velocities. Conversely, a system with a lesser inflow rate of materials, such as experiment A06, could support the capture of more fines along the topset.

In the end, we know of the four primary mechanisms that caused both the vertical and downstream segregation dynamics we witnessed in our experiments. The first

process was the varying settling velocities of the sediment that brought about the downstream fining where fast settling particles deposited farther upstream than particles with slower settling velocities. The foreset exhibited the second mechanism of shear segregation which helped the front resurface and deposit large particles closer to the bottomset. The differing mobility added to the sorting when smaller grains were forced into small pore spaces while larger grains were allowed to travel farther down the foreset slope during avalanches. Lastly, we had winnowing occur along the topset of our deposits which affected the retention of fine sediment. With an increased flow across the topset, winnowing took place causing the finer grains to be removed from the coarse grains of the topset.

It would be interesting to relate our findings in the topsets of A05 and A06 to the work of Parker (1990). However, this study would be beyond the scope of this work.

4.6.6 Comparison to Gilbert Delta Sorting Experiments

Summary of Kleinhans' Sorting Experiments

We introduce a similar summary of Kleinhans' sorting experiments in section **3.6.6**. We see the development of Gilbert deltas in the natural environment when rivers deposit coarse sediment into large bodies of freshwater such as lakes. In order to learn more about the segregation and sorting that takes place in these deposits, we explored Kleinhans' work on the grain size sorting processes that arise at the lee slope or foreset of deltas. Kleinhans tested his hypothesis in a narrow flume by varying flow conditions and sediment mixtures. These experiments yielded the deposition of sediment at the upper part of the lee slope or foreset which eventually exceeded a threshold and flowed down the slope in a grainflow. As grainflows continued to occur and the delta progressed downstream, Kleinhans recognized grain size sorting and an upward fining trend in his deposits.

Height Variations of Relative Grain Size

Kleinhans observed a general upward fining trend in his experiments conducted with a variety of sediment mixes as the results of kinetic sieving and grainflows. We included the plots from Kleinhans (2005) in section **3.6.6** in **Figure 3.6.2**. Kleinhans recorded this vertical trend for many of his experiments apart from the occasional variance in the bottom portion of some deposits.

We display the overall average relative frequency distributions for the top, middle, and bottom layers for experiments A05 and A06 in **Figure 4.6.1 (a)** and **(b)**. In order to better compare with Kleinhans' relative grain size plots in **Figure 3.6.2**, we calculated our relative grains sizes with **Equation 21** in section **3.6.6**. We set our relative deposit heights according to **Table 3.6.5**, also in section **3.6.6**. We document our relative grain size values as a function of relative deposit height in **Figure 4.6.1 (c)**.

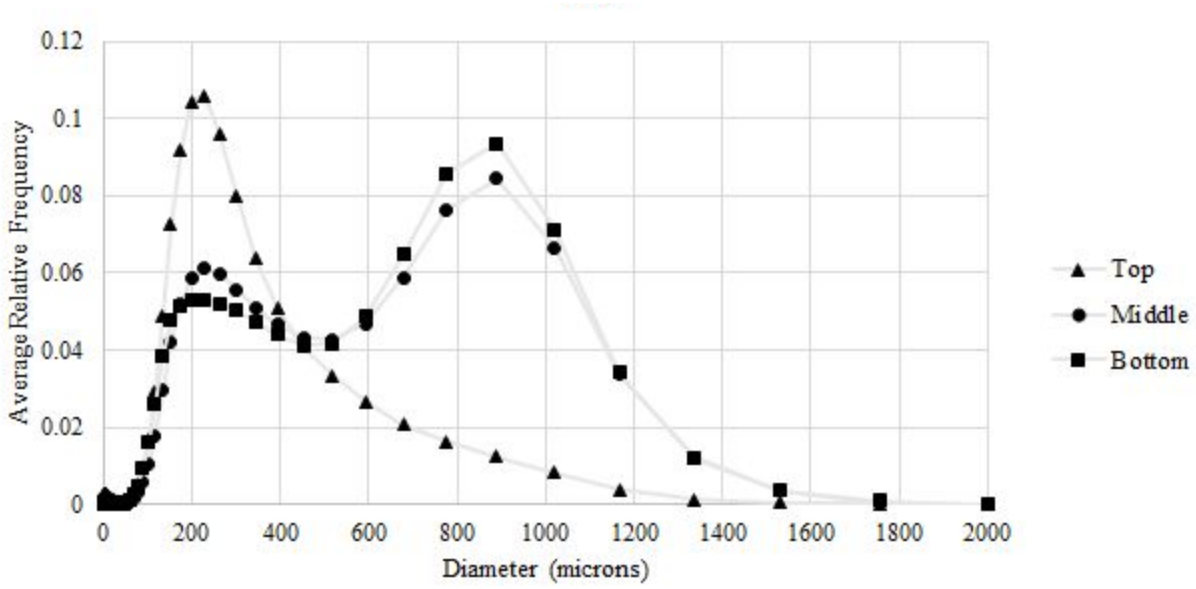

(a)

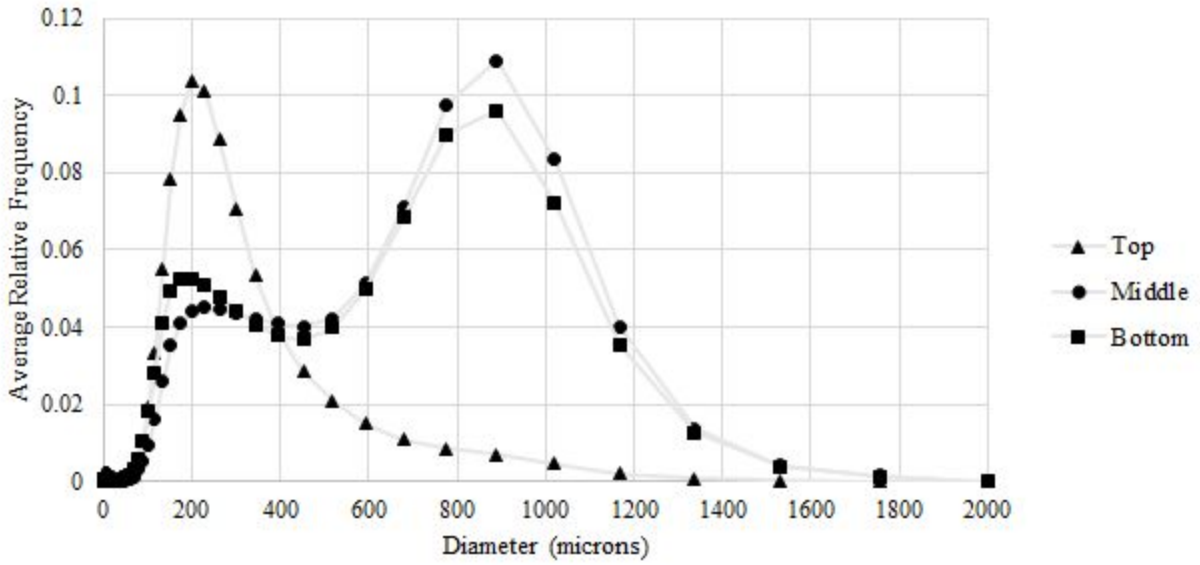

(b)

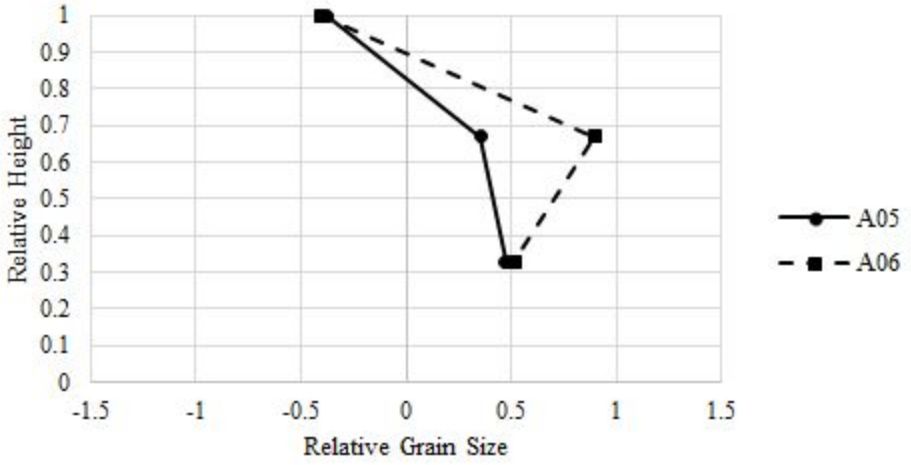

(c)

Figure 4.6.1: (a) Overall average relative frequency plot for A05 averaged for each deposit layer over all coring locations. We can see the highest large-grain peak in the bottom layer, followed by the middle, and then the top. This is not the case for A06 in **(b)** where the highest large-grain peak is in the middle layer instead of the bottom. We include the relative median plots for A05 and A06 in **(c)** to better compare with Kleinhans. The relative grain sizes were calculated according to **Equation 21** and our relative heights were established in **Table 3.6.5** in section **3.6.6**. The average relative frequency distributions from the coring locations where the deposit had not yet fully formed were not included in these plots.

The plots in **Figure 4.6.1 (a)** and **(b)** display the overall average relative frequency distributions for the top, middle, and bottom section from experiments A05 and A06. We compare our relative grain size plot from A06 in **Figure 4.6.1 (c)** to those produced by Kleinhans in **Figure 3.6.2 (b)** to reveal similar upward fining trends. The relative grain size plot for A05 from **Figure 4.6.1 (c)**, on the other hand, matches the Kleinhans plots from **Figure 3.6.2 (a)**. The distributions for the bottom and middle layers of A05 and A06 from **Figure 4.6.1 (a)** and **(b)** are so similar that a result like this is likely. The layer with the higher large-grain peak could change by simply including a few more grain size distributions from the Horiba. We further discuss the vertical trend we documented in our experiments in section **4.6.5**. A detailed examination on the cause of bottomset variation uncovered with our experiments as well as those conducted by Kleinhans is included below in ***Formation of the Bottomset***.

Height Variation in Relative Standard Deviation

We created relative standard deviation plots as shown in **Figure 4.6.2** so as to demonstrate the extent of sorting in each layer of his deposits and to compare to Kleinhans' results from **Figure 3.6.4**

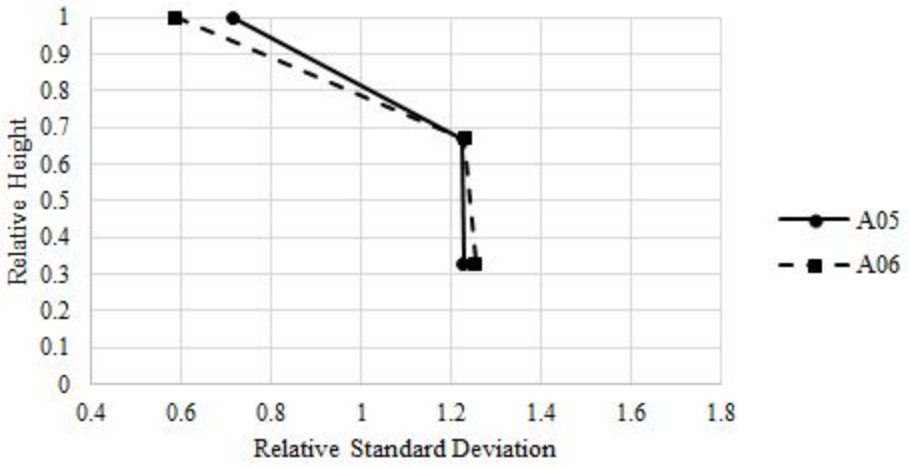

Figure 4.6.2: Relative standard deviation values from A05 and A05 from **Figure 4.6.1** at various deposit heights. For both A05 and A06, the top layer is well sorted resulting in relative standard deviation values less than one. The middle and bottom layers were not sorted as well and therefore have relative standard

deviation values that are greater than one. The relative standard deviations were calculated with **Equation 22** and the relative heights were set according to **Table 3.6.5** in section **3.6.6**.

From viewing **Figure 4.6.2**, we can see that our relative standard deviation values for both experiments were rather similar at each deposit layer. For the top, the sediment was well sorted as shown by the relative standard deviation values that are smaller than one. This feature is also visible in **Figure 4.6.1** for both A05 and A06 where the top distributions are primarily composed of fine grains. As for the middle and bottom layers, the relative standard deviations were somewhat similar and larger than one. **Figure 4.6.1** displays how unsorted these layers were with small- and large-grain peaks that are similar in intensity. Compared to our relative standard deviation values for A02 and A03 from **Figure 3.6.5**, our values for A05 and A06 are, in general, farther from one.

Formation of Bottomset

Kleinhans observed the sediment at the bottom of many of his deposits exhibited a reversal in the height-dependent segregation trend. This is shown primarily in the relative grain size plots in **Figure 3.6.2 (b)**. We witnessed a similar behavior with all of our experiments apart from A05 as displayed in **Figure 3.6.3 (c)** and **Figure 4.6.1 (c)**. As stated by Kleinhans, the considerably larger relative standard deviation in the bottom layer was caused by the mixing of previously settled finer grains and the largest grains at the bottom of the grainflow. For experiments A05 and A06, the relative standard deviations for the middle and bottom sections were larger than one, indicating the sediment was mixed. It is likely that we recorded such poor sorting in these regions partially because of the introduction of silica sand to the mixture. For the bottomset, an initial stage of formation took place when some sediment deposited after the plume progressed downstream. The major contribution to the bottom portion of the deposit came from the deposition of suspended sediment upstream of the advancing foreset. These particles were initially suspended after traveling across the topset once they arrived at the deep pond water past the topset. The suspended particles were able to settle in the pond and form the bottomset since the velocity of the pond was much lower than the

velocity of the flow across the topset. The particles that settled in this region were of a range of grain sizes similar to the range that was included in the middle portion of the deposit as seen in **Figure 4.6.1 (a)** and **(b)**.

Upward Fining Trend

As mentioned in section **3.6.6**, Kleinhans observed a typical height-dependent segregation in **Figure 3.6.2** for some of his experiments with a sand and gravel mix. We did see a trend similar to this in **Figure 4.6.1 (c)** for A05.

Grain Size Distribution of Mixtures

Whereas the experiments studied in Kleinhans (2005) were tested predominantly with sand and sand and gravel mixtures, we included a portion of very fine clay particles in our mixes. The clay was incorporated in order to represent the fines found in oil sands tailings. We also included silica sand in our surrogate mixture for A05 and A06 which has a median grain size smaller than many of the sediments used by Kleinhans.

Quantity of Suspended Sediment

As was previously stated in section 3.6.6, Kleinhans mentions the small quantity of suspended sediment he observed downstream from the topset. We did not witness this effect for our experiments where there was a relatively high amount of sediment suspended in the pond. The clay particles that were suspended during our experiments remained in suspension for a while before depositing.

Initial Flume Conditions

We discuss the specific variations between our flume setup to that used by Kleinhans in section **3.6.6**. Some of these variations include slightly different flume dimensions as well as contrasting initial flow conditions for materials after entering the flume.

Conclusion

Regardless of the variations between our experiments and the experiments performed by Kleinhans, we still had similar formation and development of our deposits. We also found this to be the case even after altering the inflow and the makeup of the sediment mixture. This realization could indicate that the ideas present in Kleinhans (2005) are applicable to Gilbert deltas with a wide range of sediment compositions and flows. Since trends and behaviors such as these have also been identified in some natural systems, it is probable that TSRU tailings deltas could perform comparably in similar conditions.

4.7 Conclusions from Coal, Clay, and Silica Study

Since we had previous knowledge that our coal and clay mixture had imitated TSRU tailings well in **Chapter 3**, we used a similar composition for our experiments in **Chapter 4** with the addition of silica sand. Again, we studied the settling rate of the initially settled layer in both our new surrogate mixture and the TSRU tailings. We examined silica sand in detail by collecting its grain size distribution and viewing it under a microscope. We then ran and recorded experiment A05 with a discharge rate of 1.0 L/s in our experimental flume and once the experiment was completed, we were able to collect data and perform our analysis. For the purpose of examining the layers of the deposit in the vertical and horizontal directions, we took core samples along the length of the deposit. This procedure was repeated for experiment A06 with the same surrogate mixture but with a discharge rate of 0.5 L/s.

Similar to our results from A02 and A03, our deposits formed during A05 and A06 appeared to be similar in style to a Gilbert delta. For both experiments, there was a plume of suspended sediment that traveled the entire length of the flume that initially deposited some sediment as it progressed downstream. As this was happening, a wedge of sediment began to collect at the downstream end of the upstream weir. With time, the wedge grew to the level of the weir, flattened out on top, and started to prograde

downstream. The progression of the deposit front downstream was supported by the continuous accumulation of grains at the upper end of the front and then avalanching down the slope. This process persisted so that the front of the deposit continued to move downstream while the topset aggraded at a much slower rate. When the experiment finished, the suspended particles began to settle and form a relatively thin layer over the coarser material.

We observed that the deposits developed far more in the direction perpendicular to the surface of the foreset than the topset by examining the profiles of the deposits. The velocities of the topset and foreset were quantified to further provide evidence for this statement. In the experiment where the inflow rate was doubled, the progression of the deposit in the direction adjacent to the foreset doubled. This was also the case for the topset velocity. These results agreed with our theoretical predictions as well as experiments A02 and A03.

When comparing the final topset slope values of A05 and A06 to those from A02 and A03, we again found that the experiments with lower inflow rates exhibited steeper topset slopes. The foreset slopes for the coal, clay, and silica sand experiments matched the trend we discovered for A02 and A03 in which the slope was nearly twice as steep for the experiment with the lower inflow rate of material. The final bottomset slopes for these experiments proved to be especially shallow and relatively similar as we also found with the coal and clay experiments.

The fact that the inflow rate of sediment for A05 was double the rate of A06 and yet the topset and foreset velocities still doubled signifies that the ratio of sediment transported across the topset to the foreset would need to remain the same for both experiments. We found this to be the case in our original and modified sediment transport ratios for experiments A05 and A06. This behavior also matched our findings from the coal and clay experiments. Our modified ratios revealed that approximately half of the sediment fed into the system deposited in the topset while the rest was transported across this region. Our unmodified transport ratios implied that less than 10% of the new sediment was transported across the topset whereas our modified results revealed this

value was almost 50%. These values are more fitting to our results with a greater amount of sediment being delivered to the foreset which allowed the foreset to aggrade at a faster rate than the topset.

We completed a grain size analysis on the core samples we extracted from both deposits and found several sorting and deposition trends. We first uncovered variability in our grain size distributions that we attempted to correct by averaging all of our distributions. When comparing our grain size distributions from both upstream and downstream locations we recognized a downstream fining trend in the bottomset. This behavior was caused by larger particles settling closer to the inlet while smaller particles remained in suspension for longer and deposited farther downstream. We found on average the middle and bottom sections of the deposit exhibited similar grain size distributions when silica sand was included in the mix. This implies that the sediment that deposited in the bottomset and the sediment that was sieved along the foreset had relatively similar grain size distributions.

Even though we used a vastly different mixture for our experiments, we still found our deposits to develop similarly to Gilbert deltas studied in Kleinhans (2005). This included the general formation of the deposit especially along the foreset through grainfall and the settling of particles in grain falls. Through examination of core samples, Kleinhans observed a unique upward fining trend with the largest grains in the middle of the deposit for his experiments with some finer grains. We also uncovered this vertical trend with experiment A06. Similar to Kleinhans, we found our bottom layer contained a wide distribution after comparing our relative standard deviation plots. Whereas Kleinhans contributes this to the mixing of previously settled fine grains with coarse grains from the bottom of the foreset, we attribute this trend to the mixture of grains that settled along the bottom of the flume before being covered by the advancing foreset. We also found our middle layer of the deposit contained a wide distribution which we owe to the alternating layers of silica sand and coal produced by the kinetic sieving along the foreset. Even though we did include much smaller grains in our experiments, we still

found numerous commonalities between the Gilbert deltas studied in Kleinhans (2005) and our own.

In conclusion, we were able to uncover convincing evidence that altering the inflow rate notably influenced the transport, deposition, and segregation of the coal, clay, and silica sand surrogate mixture. We discovered results that had many similarities to the Gilbert deltas studied in Kleinhans (2005). The sediment mixtures we included in our experiments contained grains much finer than the mix used by Kleinhans. After analyzing our core samples from A05 and A06, we reported grain size variability, downstream fining, upward fining, and the capture of some finer particles on the topset. These trends were similar to what we observed with our experiments with coal and clay.

Similar to our results from A02 and A03, we found our low flow experiments had a more intense small-grain peak. This provides further evidence that the decrease in the inflow of materials and the shear stress across the topset resulted in the enhanced capture of fine grains in this area. In the end, we were not able to confirm that the addition of dense silica sand in the experimental mixture increased the capture of finer particles along the topset.

Chapter 5 - Summary, Complications, and Future Work

5.1 Summary

In this work, we studied the interdependence of the transport, depositional, and segregation behaviors of tailings materials in tailings ponds. We accomplished this by performing laboratory flume experiments with a surrogate mixture that allowed for the observation and analysis of said behaviors so as to further understand how these mechanisms impact the reclamation of oil sands tailing ponds.

A series of experiments was conducted in a narrow flume which represented a local 2D depositional feature of a tailings delta. We performed these experiments with safer and easy-to-use surrogate mixtures that exhibited similar settling behaviors to actual TSRU tailings. For our initial experiments, we used a mix of anthracite coal with a small portion of kaolinite clay. Our second sediment mixture replaced a portion of the coal with silica sand, which had a smaller median grain size and a larger density than coal. For each surrogate mixture, we performed experiments with two different discharge rates that we established through analyzing an actual tailings ponds system. Our inflow rates varied by a factor of two, allowing for us to examine how altering the flow or the shear stress across the bed affected our results.

When the materials first entered the flume, they appeared as a plume that travelled the length of the flume. Following this, a thin layer of deposited sediment appeared along the bottom of the flume. In time, sediment began to collect near the upstream weir in the shape of a wedge. This wedge gradually heightened until it reached the level of the upstream weir at which point the top of the wedge began to flatten out. This action formed the topset surface and a Gilbert-style delta began to take shape. As more materials continued to enter the flume they flowed over the top surface of the topset. At the edge of the topset, some of the largest grains settled at the upper portion of the foreset. Once this collection of large grains exceeds a certain size, the sediment is released down the surface of the foreset and performs kinetic sieving, causing fine grains into small openings and

allowing coarse grains to continue to the bottom of the foreset. Any sediment that did not fall to the foreset became suspended in the region of the pond above the foreset and bottomset. These grains were eventually allowed to settle either along the lower region of the foreset or on the bottomset. These processes were found during the formation of all of our deposits and resulted in the creation of the three distinct regions known as the topset, foreset, and bottomset.

There were several behaviors we observed with our deposits that remained consistent regardless of altering both the inflow rate and the composition of the surrogate mixture. Firstly, when examining the final slopes values, we found the final bottomset slopes for all of our deposits were very shallow and similar in magnitude. This was mainly due to the bottomset layers being formed purely through settling of fine grain materials. For all of our deposits, we observed the trend of downstream fining in the bottomset through comparing grain size distributions at upstream and downstream locations. At the downstream locations, the large-grain peak decreased whereas the small-grain peak increased. When we compared our grain size distributions for the three deposit layers, we found that the top layer consistently had the highest small-grain peak meaning it contained the most fine grained sediment. Additionally, we found all of our deposits had foreset velocities that were much greater than topset velocities due to the topset being limited by the level of the pond. Finally, the modified sediment transport ratios for all of our experiments were very similar regardless of the inflow rate and the mixture composition.

Alternatively, we uncovered a few trends that changed in response to altering the composition of the surrogate mixture. The first noticeable difference we observed was the formation of highly concentrated alternating layers of coal and silica sand in the foreset as the result of kinetic sieving. By replacing half of the coal with silica sand, we found the average grain size distributions for the entire middle and bottom deposit layers to be very similar. This finding contrasted what we found with the coal and clay experiments where the middle layer had significantly more coarse grains than the bottom layer. Additionally, when we incorporated silica sand in our mixture we found the topmost

layer was far more sorted than the other deposit layers. For our experiments with only coal and clay, we found all three layers had roughly the same amount of sorting.

There were some trends that were only affected by the altering of the inflow rate of materials into the flume. We realized that when the discharge into the system doubled, the topset and foreset velocities both increased twofold. This was the case for both sediment mixtures. For both the topset and foreset, the final slopes were steeper, sometimes twice as steep, for lower inflow rates. This was due to the topset and foreset having to move sediment through these regions with a lower flow which required the slope to steepen. Through comparing our grain size distributions for the experiments with the same mixture composition but varying inflow rates, we found the experiments with the lower inflow rates retained more finer sediment along the topset due to the decrease in the shear stress across this region.

We found that all four of our experimental deposits developed and progressed similarly to a prograding Gilbert-style delta and exhibited many of the transport, sorting, and depositional mechanisms possessed by natural river deltas. There are many analogies that can be made between the observations we made during our experiments and the behaviors possessed by Gilbert deltas. Since Gilbert-style deltas have been studied extensively there are many other potential correlations that could be made with these deltas to tailings deltas that have yet to be uncovered.

As we stated previously the major motivation for this work was to provide information to the oil sands industry that could assist them in their tailings ponds reclamation process. We know that the reclamation of these ponds is delayed by the fines located in the ponds along the Beach Below Water (BBW) that take a long time to settle. One way to fix this issue would be to capture more fines in the deposit or along the Beach Above Water (BAW). Our surrogate experiments provided results that suggest a decrease in the inflow of materials or the shear stress along the topset could enhance the retention of finer grains on the topset. Additionally, with our experiments we established that the foreset advanced at a much faster rate than the topset. Since we were able to find more fine grains along the topset with a low flow, it is possible that further advancing the

topset could increase the retention of fine particles. From this, we would recommend for the oil sands industry to modify certain dynamics so as to increase the development of the topset and therefore enhance the concentration of fines captured.

In the end, we were unable to provide significant evidence that the addition of dense silica sand at the inflow of our experiments further enhanced the capture of fines along the topset. Although we did not test this method, it is possible that placing silica sand across the deposit at a later time, perhaps after the discharge of materials ceased, could enhance the codeposition of materials that remained in suspension.

5.2 Complications Throughout Study

While the results for our work are well-founded, there are a number of difficulties worth mentioning that provide some caveats.

5.2.1 Inlet Sampling Complications

After calculating the solids content of the inlet samples, the sampling method used to obtain these samples was deemed unfit. In order to extract an inlet sample, we dipped a scoop in the constant head tank while the experiment was running. The materials from the scoop were then transferred into a sample bottle for later testing. The solids content for the inlet samples gave values lower than expected. The materials inside of the constant head tank that the scoop was able to sample were likely already settled so the scoop was only able to capture water and fine particles. This would explain why the solids content for these samples were smaller than expected.

5.2.2 Mixing Complications

Throughout our experiments, we used the same mixing tank setup as shown in **Figure 5.2.1** as a top view sketch. From this image, we can see that the mixer blades

rotate in a circle and were unable to fully reach the corners of the tank which collected some sediment. This could have affected the quality of the mixing in the tank. Therefore, a square-shape of the mixing tank was not ideal for this situation.

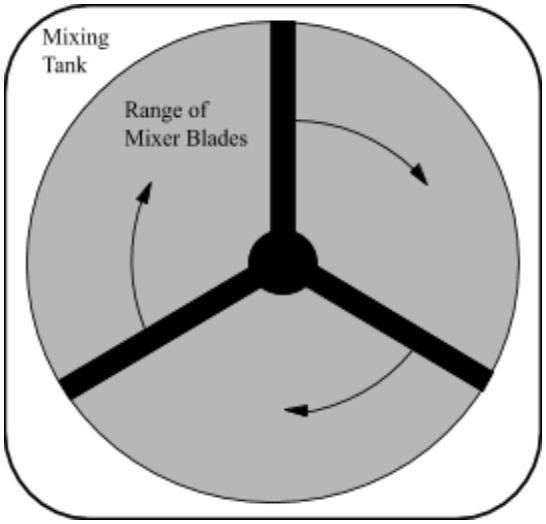

Figure 5.2.1: Sketch of top view of mixing tank. The gray circle indicates the range of the mixer blades. The solids could get trapped in the corners of the mixing tank.

5.2.3 Grain Size Analysis Sampling Complications

For all of our experiments, we found complications with our grain size analysis. We would frequently get different grain size distributions for samples that came from the same exact sample bottle, so they were retrieved from the same location within the deposit. We worked to mitigate this by performing extensive mixing on the samples before placing them in the Horiba. While mixing dry samples, we noticed some segregation occurring inside the sample bottles. If the samples were wet i.e. they contained some water that separated from the solids, the fine particles would become suspended in the fluid while the large grains settled quickly to the bottom of the sample bottle. This separation made extracting scoops with the exact same composition extremely complicated. To fix this issue, we dried the samples and then added drops of water to the samples until, while being mixed, the particles began to stick together and

not settle after mixing had stopped. We also made sure not to add too much water to the samples so that a separate liquid layer was visible. The slightly dampened grains made taking a representative scoop a lot easier. While the samples were damp, we could still perform mixing but we had to be sure that any clumps of particles were broken up.

After the samples were prepared and mixed, we extracted scoops to be inserted into the laser diffraction analyzer. We could not make any changes to the sample after it was placed in the machine and we could not see what was happening inside of the machine. If there was some sort of settling or other event occurring inside of the Horiba, we were unaware of it.

It is possible that the anthracite coal has a specific characteristic that results in strange grain size distributions. As we noticed in **3.1.3 Laser Diffraction Results**, the anthracite coal grain size distributions varied considerably between samples. The distributions for the kaolinite clay and silica sand from section **4.1.3** did not exhibit such variability between samples. The specific characteristic of the coal that could be causing this variability could be its dark color or its extreme angularity, visible in **Figure 3.1.8 (a)**.

5.3 Future Work

We found that with surrogate mixtures, we were able to systematically vary specific parameters that provided insight on better established physical mechanisms and also potentially helpful mitigation ideas. In the future, it would be interesting to test other parameters with the surrogate mixtures and see how the materials react. One potential study could be conducted by altering the depth of the pond that receives the surrogate mixture. Studying the deposit formation along with the segregation, depositional, and transport behaviors displayed by the mixture would be interesting to observe as we have seen the vertical aggradation of the deposit is limited by the water level inside of the flume. Another possibility would be further varying the composition of the surrogate mixture. We could alter the concentrations by weight for our fine and coarse surrogate

mixture components or even replace coal with all silica sand. An additional possibility would be to slightly adjust the water content of the surrogate mixture since not all tailings delivered to tailings ponds contain a similar solids content. We are aware that the addition of extra water in tailings ponds is not a desirable outcome for the oil sands industry since their reclamation processes are based around removing as much fluid from the ponds as possible. It would be interesting to view how all of these variations would affect the settling, transport, and sorting processes present in the formation of a deposit.

At this point, we have performed a study similar to the methods described in **Chapter 2** on TSRU tailings received from an oil sands tailing mining facility in an almost identical experimental system. With this system, we have tested the tailings materials under varying inflow conditions so as to observe their segregation, transportation and depositional behaviors. We have carried out a similar data collection process and analysis of the tailings materials as we did for the surrogate materials. For these experiments, we implemented a new, more representative inlet sampling technique as well as a surface sampling technique that extracts samples near the edge of the topset. These samples were taken at relatively the same time so we could see how changing the flow rate affected the grain size distributions and solids content of these samples after traveling over the topset. Through conducting experiments with actual TSRU tailings, we have come up with similar recommendations for the industry including lower the inflow rate of new materials and adding coarse sediment to encourage codeposition in the pond.

In the end, there are a number of potential variations that could have been considered with our surrogate experiments that could have yielded interesting results for the oil sands industry (e.g. altering the pond level, varying the surrogate composition, slightly changing the water content of the surrogate mixture). The variations that we tested with our experiments were those that would be most feasible for the oil sands industry to incorporate. The oil sands producers can more easily alter the discharge rates into the ponds as compared to changing the concentration of the tailings. We hope that in the future, oil sands tailings producers are able to implement variations in their

reclamation processes based on our findings and observe less segregated tailings ponds, allowing for faster reclamation.

Bibliography

7 facts on the oil sands and the environment. (2019, March 15). Retrieved from http://www.nrcan.gc.ca/energy/oil-sands/18091

2018 CAPP Crude Oil Forecast, Markets & Transportation. (2018). Retrieved from https://www.capp.ca/publications-and-statistics/publications/320294

A Guidebook to Particle Size Analysis. (2012). Retrieved from https://www.horiba.com/fileadmin/uploads/Scientific/Documents/PSA/PSA_Guidebook.pdf

Abeyta, A. (2016). The morphodynamic influence of cohesive sediment on coastal systems across scales.

Anthracite Coal; MSDS No. 8029-10-5; Asbury Carbons Inc.: Asbury, NJ, May 20, 2015.

Barrell, J. (1912). Criteria for the recognition of ancient delta deposits. *Geological Society of America Bulletin, 23*(1), 377-446. doi:10.1130/gsab-23-377

Beier, N., et al. (2013). Impact of flocculation-based dewatering on the shear strength of oil sands fine tailings. *Canadian Geotechnical Journal*, *50*(9), 1001-1007.

BGC Engineering, I. July 2010. Oil Sands Tailings Technology Review. Oil Sands Research and Information Network, University of Alberta, School of Energy and the Environment, Edmonton, Alberta. OSRIN Report No. TR-1. 136 pp.

Canada's Oil Sands Fact Book. (2018, July). Retrieved from https://www.capp.ca/publications-and-statistics/publications/316441

Chavarrías, V., et al. (2018). A sand-gravel Gilbert delta subject to base level change. Journal of Geophysical Research: Earth Surface, 123, 1160–1179. https://doi.org/10.1029/2017JF004428

Colella, A., De Boer, P.L. & Nio, S.D. (1987). Sedimentology of a marine intermontane Pleistocene Gilbert-type fan-delta complex in the Crati Basin, Calabria, southern Italy. Sedimentology, 34, 721–736.

Czuba, J.A., et al. (2011). Sediment load from major rivers into Puget Sound and its adjacent waters: U.S. Geological Survey Fact Sheet 2011–3083, 4 p.

Gilbert, G. K. (1890). *Lake Bonneville* (Vol. 1). US government printing office.

Gobo, K. (2014). Development of Gilbert-type deltas: sedimentological case studies from the Plio-Pleistocene of Corinth Rift. *Greece: Doctoral thesis thesis, University of Bergen*.

Gobo, K., Ghinassi, M., & Nemec, W. (2014). Reciprocal changes in foreset to bottomset facies in a Gilbert-type delta: response to short-term changes in base level. *Journal of Sedimentary Research*, *84*(11), 1079-1095.

Hande, A. B. (2014). Accelerated dewatering and drying treatment of oil sands tailings by electrical resonant auto-transformer. *Master of Science Thesis, University of Alberta, Canada*.

Hillen, M. M. (2009). Wave reworking of a delta: Process-based modelling of sediment reworking under wave conditions in the deltaic environment.

Introduction to Oil Sands. (2018). Retrieved from https://www.capp.ca/publications-and-statistics/publications/322601

Kaolin Slurry; SDS No. 093-GHS; Unimin Corporation: New Canaan, CT, April, 2014.

Kim, W., et al. (2006). Shoreline response to autogenic processes of sediment storage and release in the fluvial system. *Journal of Geophysical Research, 111*(F4). doi: 10.1029/2006jf000470.

Kim, W., et al. (2009). Delta progradation driven by an advancing sediment source: Coupled theory and experiment describing the evolution of elongated deltas. *Water Resources Research*, *45*(6).

Kleinhans, M. G. (2005). Grain‐size sorting in grainflows at the lee side of deltas. *Sedimentology*, *52*(2), 291-311.

Lai, S.Y.J. & Capart, H. (2007). Two-diffusion description of hyperpycnal deltas. J. Geophys. Res., 112, F03005, doi: 10.1029/2006JF000617.

Lai, S. Y. J., Chiu, Y.‐J., & Wu, F.‐C. (2019). Self‐similar morphodynamics of Gilbert and hyperpycnal deltas over segmented two‐slope bedrock channels. Water Resources Research, 55, 3689–3707. https://doi.org/10.1029/ 2018WR023824.

McCrone, A. W. (1962). Clarification of the "winnowing" concept in geology. Geological Society of America Bulletin, 73(4), 517-518.

Meyer-Peter, E. and Müller, R. (1948). *Formulas for bed-load transport*. Proceedings of the 2nd Meeting of the International Association for Hydraulic Structures Research. pp. 39–64.

Mining for Bitumen. (2017, November 7). *Oil Sands Magazine*. Retrieved from https://www.oilsandsmagazine.com/technical/mining

Mining Operations. (2019, May 27). *Oil Sands Magazine*. Retrieved from https://www.oilsandsmagazine.com/projects/oilsands-mining

Morris, P. H., & Williams, D. J. (1997). Hydraulic conditions leading to exponential mine tailings delta profiles. *Transactions of the Institution of Mining and Metallurgy-Section A-Mining Industry*, *106*, A34.

Mugade, Usha & Sapkale, Jagdish. (2015). Influence of Aggradation and Degradation on River Channels : A Review. International Journal of Engineering and Technical Research (IJETR). 3. 209-212.

Muto, T., & R. J. Steel (2004). Autogenic response of fluvial deltas to steady sea-level fall: Implications from flume-tank experiments, *Geology, 32*(5), 401 – 404.

Muto, T., & J. B. Swenson (2005). Large-scale fluvial grade as a non-equilibrium state in linked depositional systems: Theory and experiment, *J. Geophys. Res.*, 110, F03002, doi:10.1029/2005JF000284.

Naito, K., et al. (2019). Extended Engelund–Hansen type sediment transport relation for mixtures based on the sand-silt-bed Lower Yellow River, China, Journal of Hydraulic Research, DOI: 10.1080/00221686.2018.1555554

Nemec, W. (1995). The dynamics of deltaic suspension plumes. In: Geology of Deltas (Eds M.N. Oti and G. Postma), Balkema, Rotterdam, pp. 31–93.

Oil Sands Extraction and Processing. (2016, February 19). Retrieved from http://www.nrcan.gc.ca/energy/oil-sands/18094

Paola, C., et al. (2011). Natural processes in delta restoration: Application to the Mississippi Delta. *Annual Review of Marine Science*, 3(1), 67– 91.

Parker, G. (1990). Surface-based bedload transport relation for gravel rivers. *Journal of hydraulic research*, *28*(4), 417-436.

Pirmez, C., Pratson, L., & Steckler, M. (1998). Clinoform development by advection-diffusion of suspended sediment: Modeling and comparison to natural systems. Journal of Geophysical Research. 1032. 24141-24158. 10.1029/98JB01516.

Roshani, A. (2017). *Drying Behavior of Oil Sand Mature Fine Tailings Pre-dewatered with Superabsorbent Polymer* (Doctoral dissertation, Université d'Ottawa/University of Ottawa).

Seybold, H., Andrade, J. S., & Herrmann, H. J. (2007). Modeling river delta formation. *Proceedings of the National Academy of Sciences*, *104*(43), 16804-16809.

Swenson, J. B., et al. (2000). Fluvio-deltaic sedimentation: A generalized Stefan problem. *European Journal of Applied Mathematics*, *11*(5), 433–452. doi: 10.1017/s0956792500004198

Wang, X., et al. (2010). Polymer aids for settling and filtration of oil sands tailings. *The Canadian Journal of Chemical Engineering*, *88*(3), 403-410.

Wildermuth, E., Reece, A., & Morgan, J. (2015, March 11). Marine Sediments: Deltas. Retrieved from http://www.sepmstrata.org/page.aspx?&pageid=72&4

Xu, Y., Dabros, T., & Kan, J. (2013). Investigation on alternative disposal methods for froth treatment tailings—part 1, disposal without asphaltene recovery. *The Canadian Journal of Chemical Engineering*, *91*(8), 1349-1357.